UNIVERSIDADE ESTADUAL PAULISTA
"JÚLIO DE MESQUITA FILHO"
CAMPUS DE GUARATINGUETÁ

TATIANE DE PAULA MORAES

Analysis of the emission of gravitational waves by compact binaries during coalescence.

Guaratinguetá
2022

Tatiane de Paula Moraes

Analysis of the emission of gravitational waves by compact binaries during coalescence.

Dissertação apresentada ao Conselho de Curso de Pós Graduação em Física da Faculdade de Engenharia do Campus de Guaratinguetá, Universidade Estatual Paulista, como parte dos requisitos para obtenção do título de Mestra em Física na área de Relatividade e Gravitação.

Supervisor: Profº Dr. Rogerio Teixeira Cavalcanti
Co-supervisor: Profº Dr. Elias Leite Mendonça

Guaratinguetá
2022

Moraes, Tatiane de Paula
M828a Analysis of the emission of gravitational waves by compact binaries during coalescence / Tatiane de Paula Moraes – Guaratinguetá, 2022.
99 f : il.
Bibliografia: f. 82-85

Dissertação (Mestrado) – Universidade Estadual Paulista, Faculdade de Engenharia de Guaratinguetá, 2022.
Orientador: Prof. Dr. Rogério Teixeira Cavalcanti
Coorientador: Prof. Dr. Elias Leite Mendonça

1. Ondas gravitacionais. 2. Relatividade geral (Física) 3. Gravidade (Física) I. Título.

CDU 534(043)

Luciana Máximo
Bibliotecária CRB-8/3595

unesp

UNIVERSIDADE ESTADUAL PAULISTA
CAMPUS DE GUARATINGUETÁ

TATIANE DE PAULA MORAES

ESTA DISSERTAÇÃO FOI JULGADA ADEQUADA PARA A OBTENÇÃO DO TÍTULO DE
"MESTRE EM FÍSICA"

PROGRAMA: FÍSICA
CURSO: MESTRADO

APROVADA EM SUA FORMA FINAL PELO PROGRAMA DE PÓS-GRADUAÇÃO

Prof. Dr. Ernesto Vieira Neto
Coordenador

B A N C A E X A M I N A D O R A:

Prof. Dr. ROGÉRIO TEIXEIRA CAVALCANTI
Orientador - UNESP
participou por videconferência

Prof. Dr. MÁRCIO EDUARDO DA SILVA ALVES
UNESP
participou por videconferência

Prof. Dr. ÉLVIS CAMILO FERREIRA
CP3, IRMP / Université Catholique de Louvain
participou por videconferência

Junho *de 2022*

I dedicate this work to all my friends, family and teachers who contributed to my academic formation.

ACKNOWLEDGEMENTS

I would like to thank everyone who contributed during this journey, especially:

To my parents who supported me in all my choices and throughout my master's degree.

To Prof Dr. Julio Marny Hoff da Silva, who started me in General Relativity, gave me support and conditions to continue my master's degree, especially during the pandemic period.

Prof. Elias Leite Mendonça who inspired and motivated me since graduation.

To my supervisor Prof Dr. Rogerio Teixeira Cavalcanti who played a fundamental role in my scientific training and in the preparation of this work. I am grateful not only for the academic support but for all the understanding and help in these 5 years of guidance, especially during the beginning of the pandemic.

To my friends, I thank in a special way: Henrique, João, Gabriel, Andre and Heron for their companionship and availability to help me at various times.

I also thank my partner in life, Felipe Augusto da Silva Barbosa, for helping me throughout the master's degree, supporting me in the most challenging moments and also greatly contributing to my academic learning. His support, in all aspects but mainly emotionally, helped me to overcome many difficulties.

This work had the financial support of the Virtual University of the State of São Paulo (UNIVESP).

ABSTRACT

The main goal of this research is to give a broad view of aspects related to the study of gravitational waves from a theoretical approach to the analysis of simulated signals. The research is mainly based on the analysis of coalescence process of compact binaries, which is described in detail in chapter 2. Then, chapters 3 and 4 describe a theoretical review of the definition of gravitational waves and their main characteristics in general relativity and massive gravity, respectively. In this context, the van Dan-Veltman-Zakharov (vDVZ) discontinuity is also discussed. Finally, chapter 5 brings a study on the detection of gravitational waves and an analysis of three simulated signals of compact binaries. It is concluded that gravitational wave research is a broad field of study and there are great expectations to test theories such as massive gravity through analysis of data collected by future observatories such as LISA. This work also discuss some challenges involved in signal analysis and presentes a possible approach to practice the techniques needed in a real analysis.

KEYWORDS: Gravitational waves. Coalescence of compact binaries. Signal analysis. Gravitation.

RESUMO

O objetivo principal desta pesquisa é dar uma visão ampla dos aspectos relacionados ao estudo das ondas gravitacionais desde uma abordagem teórica até a análise de sinais simulados. A pesquisa baseia-se principalmente no estudo do processo de coalescência de binários compactos, que é descrito em detalhes no capítulo 2. Em seguida, os capítulos 3 e 4 descrevem uma revisão teórica da definição de ondas gravitacionais e suas principais características em relatividade geral e gravitação massiva, respectivamente. Neste contexto, a descontinuidade de van Dan-Veltman-Zakharov (vDVZ) também é discutida. Por fim, o capítulo 5 traz um estudo sobre a detecção de ondas gravitacionais e uma análise de três sinais simulados de binários compactos. Conclui-se que a pesquisa de ondas gravitacionais é um campo amplo de estudo e há grandes expectativas de testar teorias como a gravidade massiva por meio da análise de dados coletados por futuros observatórios como o LISA. Este trabalho também discute alguns desafios envolvidos na análise de sinais e apresenta uma possível abordagem para praticar as técnicas necessárias em uma análise real.

PALAVRAS-CHAVE: Ondas gravitacionais. Coalescência de binários compactos. Análise de sinal. Gravitação.

LIST OF FIGURES

Figure 1 Different regimes according to the intensity of the gravitational fields: Each gravitational field regime requires different mathematical approaches, with the weak field limit being the simplest case. When the gravitational field is very intense, the equations become even more challenging to solve. 19

Figure 2 Illustration of the Schwarzschild precession. This figure represents an amplified view of the precession present in orbits predicted by general relativity. With each passage of the smaller object through the periastron, its orbit undergoes a slight deviation, forming a rosette instead of following a closed elliptical orbit. 21

Figure 3 Observational results of the Schwarzschild precession in the star S0-2: In this figure we can see the path taken by the star S0-2 in its orbit around the supermassive black hole present at the center of the Milky Way. After reaching its closest approach to Sagittarius A*, the orbit undergoes a deviation and does not close. Observational measures are also compatible with the values predicted in GR . . 22

Figure 4 Stages of binary black hole coalescences: This figure represents the result obtained from a relativistic numerical simulation (PRETORIUS, 2007). The purpose was to study the energy loss of the binary due to the emission of gravitational waves. It highlights the main characteristics of each phase of coalescence. We can see how the Inspiral stage is much longer than the merger and the purple and orange colors indicate the increase in the emission of gravitational radiation. . 25

Figure 5 Signal of the first detection of gravitational waves after noise extraction: The spectrogram is used to show which parts of the signal have the greatest power (indicated by the yellow color). We can see how the gravitational signal stands out from the noise. On the right, we have the waveform of the gravitational wave detected and the peak of gravitational radiation emission during the merger is very evident 26

Figure 6 Behavior of the GW150914 in each stage of coalescence (ABBOTT et al., 2016): Comparison of the waveform with the binary coalescence stages. Here it becomes clear how the closer proximity between black holes increases the orbital speed and, consequently, increases the emission of gravitational waves, in which the peak occurs during the merger. 27

Figure 7 Gravitational wave merger detections: In this figure we have the representation of all the binaries detected to date (upper panel). We can see the values of the masses of the objects individually and the value of the mass of the remaining black hole. We can also see which of the objects are black holes, neutron stars and which are unknown (see "Key") in addition to being ordered according to the observing run in which they were detected. In the lower left panel we only have the zoom of some events to exemplify the use of the key. 29

Figure 8 Polarization "+": The image illustrates the effect of a gravitational wave passing through a ring of particles at rest. 37
Figure 9 Polarization "×": Cross polarization has a difference of 45° from plus polarization. 37
Figure 10 Representation of the fundamental polarization modes: In massive gravity, gravitational waves are expected to have five polarization modes, two tensor (also predicted in GR) (a) and (b), two vectors ((c) and (f)) and one scalar (which is a combination of (d) and (e) modes). Unfortunately, it is also expected that in a real emission these modes will combine, i.e., the detected signal must contain a waveform whose behavior is compatible with a mixture of two or more polarization modes, which makes the search for these signals a great challenge. To be able to find these signals, a network of detectors is needed (where five is the minimum number). We currently have only three observatories in observation mode. 41
Figure 11 Representation of Michelson interferometer. 53
Figure 12 Representation of the structure of interefometric observatories: Fabry-Pérot cavities. 54
Figure 13 Representation of the structure of interferometric observatories: Power recycling mirrors. 55
Figure 14 Representation of a sinusoidal signal in the time domain: continuous signal (a) and discrete signal (b). 57
Figure 15 Representation of a continuous sinusoidal signal in the time domain after interpolation. 58
Figure 16 Convolution between two functions f e g: Widely used in signal filtering, convolution helps to highlight parts of a signal, which can be very useful when the signal involves noise. 59
Figure 17 Window functions: rectangular and Parzen. 59
Figure 18 Window functions: Tukey and Blackman. 60
Figure 19 Data: Simulated signal - data with noise. Template- Hulse-Taylor: Template of the signal for the Hulse-Taylor binary system. The upper panel illustrates the complete signal (65536 points) while the lower panel illustrates only the first 5000 points of the signal. 64
Figure 20 Representation of data (upper image) and template (lower image) in the frequency domain. The observed behavior of the frequency domain signal is due to variations in frequency and amplitude over time. Although the gravitational signal is well behaved, the noise can vary in many different ways. 65
Figure 21 PSD of the noisy data (upper image) and the template (lower image). 66
Figure 22 ASD of the noisy signal (upper) and the template (lower). 67
Figure 23 Spectrograms: Template (lower) and noisy data (upper). The color bar indicates (on logarithmic scale) the signal power. Lighter colors indicates greater power and, in this case, also indicates the presence of a gravitational wave. 68

Figure 24 Matched Filter of a burst signal: when the signal duration is shorter than the observing duration. 69
Figure 25 Results of analysis: Signal after filtering, comparison between the signal and the template and zoom of the initial and final points of the data. The signal after filtering (in blue and black) still doesn't match perfectly the model (red and orange). 70
Figure 26 Different results for the analysis: by computing another frequency range it is possible to notice how the filtered signal looks completely changed. Here the signal fits the template a little more. 71
Figure 27 Spectrograms of both filtering. In the left we have the result for the first choice of frequencies. We can see that there is still a lot of noise. In the right plot we have the result for the second choise. In that case the frequency range is so narrow that even the gravitation wave is being filtered with the noise. 72
Figure 28 Data with noise: Simulated signal of the inspiral stage of a NSBH binary. The simulated waveform was covered with random noise and it is not possible to visualize it without performing some noise filtering. Template: Simulated waveform for the event GW170817 based on the parameters provided by the LVK collaboration. 73
Figure 29 FFT of the data with noise and the template: transforming the signal from the time domain to the frequency domain. 74
Figure 30 PSD of the data with noise nas the template: These figures highlights the points where the signal has the greatest power. This procedure helps to show where the gravitational wave is and, in a real context, it also helps to identify patterns in the noise. In this work we will use the template to help visualize the information that appears in the noisy data. Then we can compare this PSD with the previous one to confirm our choices for the frequency used in the filter. 75
Figure 31 ASD of the signal with noise and the template: On the left we have the ASD of the noisy signal and on the right the ASD of the template.The plot, as the name suggests, helps us find at which points the signal has the greatest amplitude. . . 75
Figure 32 Spectrograms: On a logarithmic scale, spectrograms relate time, frequency and signal strength. With it we can see patterns in the signal that can indicate the presence of a signal of astrophysical origin or even noises of instrumental origin, which are repeated in all detections. 76
Figure 33 Signal after noise filtering: These are the results of the filtering and the comparison between the final signal and the expected signal (template). 76
Figure 34 Residual signal and the signal after filtering. 77
Figure 35 Data with noise and template fo the event GW190426_152155. 77
Figure 36 FFT of the data and the template. 78
Figure 37 PSD of the data and the template. 78
Figure 38 ASD of the data and the template. 79
Figure 39 Spectrograms: Data with noise (left) and template (right). 79

Figure 40 Signal after filtering. 80
Figure 41 Residual signal and spectrogram of the filtered signal. 81

EVENTS AND ARTICLES

PARTICIPATION IN EVENTS

- IV Physics and Physics Engineering Week - DFI/UFLA. **Tests of General Relativity**. 2020
- XVI Physics Week at UESC **Polarization Modes of Gravitational Waves in the Context of Massive Gravity**. 2020
- XXXVII Physics week at IF - UFG. **Limits for the Mass of the Graviton**. 2020

ARTICLES

The article “Polarization Modes of Gravitational Waves in the Context of Massive Gravity" was published in the “Physics Week Magazine" at UESC in 2021 (MORAES, 2021).

CONTENTS

1 INTRODUCTION 16

2 MODERN TESTS OF GENERAL RELATIVITY 18
2.1 Test in the Weak Field Limit : Schwarzschild Precession 19
2.2 Tests in the Strong Field Limit 22
2.2.1 Coalescence of Binary Black Holes 23
2.2.2 First gravitational wave detection: GW150914 25
2.2.3 Tests of General Relativity with GWTC-3 27

3 REVISITING GENERAL RELATIVITY RESULTS 31
3.1 Sources of gravitational waves 31
3.2 Equations of Motion and Gauge Invariants 32
3.3 Polarizations 36

4 MASSIVE GRAVITY 38
4.1 Motivation 38
4.2 The Fierz-Pauli theory 39
4.3 The Stuckelberg Trick 43
4.4 Counting degrees of freedom 44
4.5 Another approach for the vDVZ discontinuity 49

5 SIGNAL ANALYSIS. 53
5.1 Interferometric Observatories 53
5.2 Introduction to signal processing 56
5.2.1 Fourier transform 56
5.2.1.1 Sampling Theorem 58
5.2.2 Windowing 58
5.2.3 Filters 59
5.3 Post-Newtonian Approximation 61
5.4 Simulated signal analysis 62
5.4.1 Signal 1: Hulse-Taylor Binary 62
5.4.2 Signal 2: GW170817 73
5.4.3 Signal 3: GW190426_152155 77

6 CONCLUSIONS 82

BIBLIOGRAPHY 83

APPENDIX A – GENERAL RELATIVITY: GAUGE INVARIANTS 87

APPENDIX B – MASSIVE GRAVITY: FINDING THE EQUATIONS OF MOTION 88

B.1 Part I 88

B.2 Part II 90

B.3 Part III 92

APPENDIX C – MASSIVE GRAVITY: FIELD DECOMPOSITIONS AND GAUGE INVARIANTS 94

C.1 Field Decompositions 94

C.2 Gauge Invariants 94

C.3 Coordinate Change 96

APPENDIX D – MASSIVE GRAVITY: ANOTHER APPROACH FOR THE VDVZ DISCONTINUITY 99

1 INTRODUCTION

Since their first detection in 2015, gravitational waves (GW) have become a strong topic of study in gravitation, astrophysics and cosmology. It took about one hundred years since the publication of the theory of general relativity for humankind to be able to prove the existence of these waves through a direct detection. Since then, many more detections have been done, summing up to ninety detections of compact binary mergers to date. The large increase in the number of detections in the last year is due not only to increased sensitivity of detectors but also to the development of new observatories (which also helps to increase the accuracy of locating the source in the sky). Today, the LVK collaboration (LIGO-Virgo-KAGRA) has scientists all around the world. Moreover, a new generation of observatories is being developed to act both in the ground, such as the Einstein Telescope (ADMINISTRATOR, 2022b) and the Cosmic Explorer (ADMINISTRATOR, 2022a), and in space, such as the Laser Interferometer Space Antenna (LISA) (NASA, 2022).

During the first years after the publication of general relativity theory, it was commonly argued (even by Albert Einstein) that the existence of gravitational waves was just a consequence of the linearization of the theory equations and, outside this regime, they would not exist. In this way, gravitational radiation could not be interpreted as a real physical prediction of the theory. The first attempts to obtain a plane wave solution in the full theory were made by Einstein and Nathan Rosen in 1937 (EINSTEIN, 1937). After that, Herman Bondi, Ivor Robinson and Felix Pirani also published a study where they defined a plane wave that carries energy (PIRANI, 1957). Later, in 1958, Andrzej Trautman publishes a paper in which he stablishes new boundary conditions to the problem, which were not considered in previous works. Therefore, in 1960, Trautman and I. Robinson published, for the first time, a plane wave solution derived from the full theory of general relativity.

It is worth mentioning that many other scientists were involved in the search for this solution (SORMANI et al., 2017) and much effort was put into the years following the publication of the theory until Bondi-Pirani-Robinson (BONDI; PIRANI; ROBINSON, 1959) and Trautman-Robinson (ROBINSON; TRAUTMAN, 1962) papers together provided the necessary evidences that the gravitational waves are, in fact, a prediction of the full theory.

Since then, the importance of this phenomenon has been reflected in the effort to detect these waves, in addition to the development of theoretical models and computational tools. The study of gravitational waves can contribute, for example, to a better understanding of black holes and to test theories of gravitation in extreme gravitational field regimes.

The main purpose of this work is to give a broad view of aspects related to the study of gravitational waves, from more theoretical and phenomenological concepts to the application in data analysis. Each of these different approaches helps us to explore aspects of the generation, propagation, detection and analysis of gravitational wave signals.

For that, we start with a phenomenological study of modern tests of general relativity. In chapter 2 we describe how general relativity not only completes the Newtonian theory of gravitation in certain aspects, but it also expands and transforms our understanding of gravity, leading to new possibilities

and the prediction of very interesting phenomena such as gravitational waves. In section 2.1 there is a discussion about an important test of general relativity in the weak field limit and then, in 2.2 we will have an extensive study on the coalescence of compact binaries and we shall see how the detection of gravitational waves generated by these events is crucial to test theories of gravitation in the strong field limit. This will provide us with the necessary knowledge for the discussions that follow.

Then, in chapter 3 , we revisit results from general relativity in order to demonstrate the formal description for gravitational waves and their polarization modes. There is also a study of some of the main types of sources of gravitational radiation (in addition to the compact binary merger studied in the previous chapter). This will help us to understand how these waves affect matter and what information we are aiming when we test general relativity.

However, as occurred with Newtonian gravitation, general relativity (GR) also needed some modifications. This will lead us to the study of the massive gravity theory, which is just one of many current proposals to extend general relativity. We will spend the entire chapter 4 retaking the mathematical procedures performed in the chapter 3 in order to highlight the vDVZ discontinuity present in the Fierz-Pauli theory and to understand how the inclusion of a massive graviton leads to important changes in the description of gravitational waves.

Finally, in chapter 5 we apply all this knowledge in the analysis of three simulated signals of gravitational waves. We are going to see how the detections are done and what are the main challenges involved in the construction of observatories such as LIGO.

2 MODERN TESTS OF GENERAL RELATIVITY

General Relativity (GR) introduced major changes in the way we describe the universe. Unlike in the Newtonian theory of gravitation, in GR time and space are interpreted as a single structure called spacetime. This structure is deformed in the presence of matter and energy and the description of this relation is given by the famous Einstein equation

$$R_{\mu\nu} - \frac{1}{2}Rg_{\mu\nu} = 8\pi G T_{\mu\nu}, \tag{2.1}$$

where $R_{\mu\nu}$ is the Riemann tensor, R is the Ricci scalar, $g_{\mu\nu}$ is the metric, and $T_{\mu\nu}$ is the stress-energy-momentum tensor. The left-hand side of this equation tells us how spacetime will be curved by the presence of matter and energy, whose information are expressed by the energy-momentum tensor that appears on the right-hand side. This equation also leads to a new interpretation of gravity. It shows that the gravitational manifestation between massive objects does not happen through an invisible force among two bodies, as described by Newton. Instead, massive objects bend the spacetime, pulling smaller-mass objects to fall towards them. Therefore, gravity is directly related to the fabric of spacetime itself.

With this new perspective, GR predicts that the movement of massive objects will cause small deformations in spacetime, called gravitational waves, which propagate at the speed of light. However, proving the existence of these waves through direct detection is a great challenge. Several theoretical studies were developed in order to search for evidences of the existence of gravitational waves and also to test the compatibility of the theory with observational data and with measurements already well established in Newtonian gravitation. In this work we consider two limits: the strong field limit and the weak field limit. The weak-field regime is considered when the gravitational fields involved are not very intense (as the case of the solar system) and therefore, we can use Newtonian gravitation or small corrections in this theory. When the gravitational field is moderate, for example when the components of a binary system are slowly approaching each other, we use the post-Newtonian approximation. On the other hand, the strong-field regime will be those that involve extreme gravitational fields, as in the vicinity of very compact objects such as black holes. Figure 1 illustrates how we can separate these regimes. Furthermore, in the strong-field regime the ratio between the individual masses of the binary also indicates which strategy is the most appropriate. When the ratio is close to zero, we can simply analyze the geodesics; when m/M is much smaller than 1, we must use perturbative models and when m/M is very close to 1, it is necessary to use numerical relativity.

Since its publication, GR has been frequently tested in the weak field limit. Starting from the problem of Mercury's perihelion and going throughout tests within and out of the solar system, GR has become the theory that is currently the most consistent with observational data. However, tests in the strong limit only became possible with advances in technology and the development (and improvement) of observatories such as LIGO (Laser Interferometer Gravitational-Wave Observatory), Virgo, GEO600, KAGRA, ESO (European Southern Observatory) and VLT (Very Large Telescope).

In this chapter we will see how improvements in current observations and the development of

Figure 1 – Different regimes according to the intensity of the gravitational fields: Each gravitational field regime requires different mathematical approaches, with the weak field limit being the simplest case. When the gravitational field is very intense, the equations become even more challenging to solve.

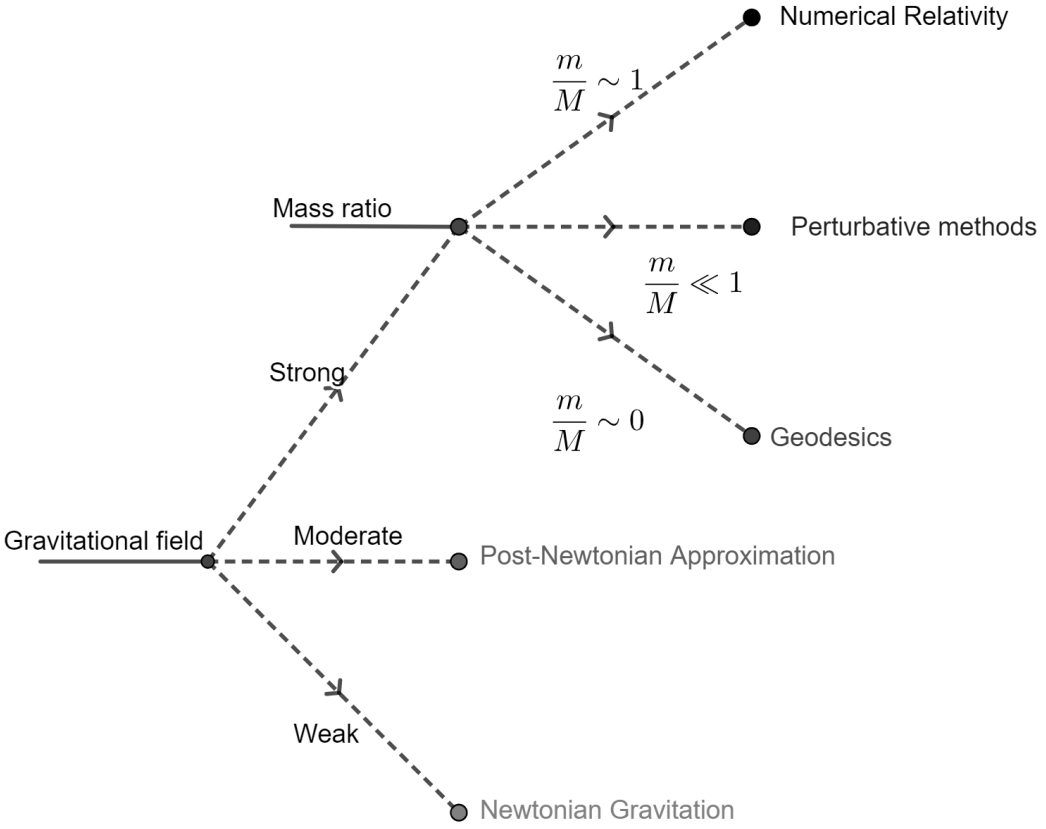

Image source: The author.

gravitational wave detectors are fundamental to test GR. For this purpose, in the section 2.1 we will briefly discuss the Schwarzschild precession and the recent discovery of this phenomenon in the star S0-2. Subsequently, in the section 2.2 , we will study in more detail the binary black hole (BBH) coalescence and the recent detections of this phenomenon by the LIGO-Virgo collaboration.

2.1 TEST IN THE WEAK FIELD LIMIT : SCHWARZSCHILD PRECESSION

We know that black holes are the most compact objects predicted by GR. As consequence of the intense deformation of spacetime, it occurs the creation of a non-return region called the event horizon. Moreover, the gravitational field generated by these black holes forces any object in their vicinity to eventually move towards them. The same happens with photons, which when attracted to the black hole's gravity, inevitably follow towards the singularity after crossing the event horizon (CARROLL, 2004). Therefore, it is not possible to directly determine the existence of these objects from equipment designed to capture light, as in the case of optical telescopes. Despite this, there is extensive evidence that these objects exist throughout the universe. Some of this evidences comes from the fact that

objects in the vicinity of these black holes are visible to us, and with GR we can predict what their behavior would be like when influenced by such intense gravitational fields.

As previously mentioned, GR describes spacetime as an elastic fabric that is deformed in the presence of matter and energy. We also know, from the equation (2.1), that very massive objects will strongly influence the behavior of lighter objects (as was also expected in Newtonian gravitation). Moreover, from observations made by the Hubble telescope (NASA, 2017), it is known that galaxies close to the Milky Way (and including the Milky Way itself) have at their core a large concentration of stars, gas and dust orbiting extremely compact objects that are consistent with the estimated order of magnitude for supermassive black holes (VILLARD, 2019).

The formal description of the formation of a region of no return, called trapped surface, was made by Roger Penrose, whose contributions earned him part of the 2020 Nobel Prize in Physics (PENROSE, 1965). Moreover, proving that the compact object at the center of the Milky Way is a supermassive black hole required nearly three decades of observations of the galactic center with 8-10 meter telescopes such as the Very Large Telescope (VLT) in Chile. Only recently, with studies of the orbits of stars like S0-2 and S0-38, it has been possible to conclude with greater precision that the only known explanation for the movement of stars in the galactic center is the presence of a supermassive black hole (CASTELVECCHI, 2022). Among these studies, stands out the contributions of Andrea Ghez (SAKAI et al., 2019) and Reinhard Genzel (GENZEL; EISENHAUER; GILLESSEN, 2010) who received the other half of the Nobel Prize in 2020 for their contributions leading a research group dedicated to improve the astrometry of the movement of these stars in the galactic center.

One of the biggest challenges in observing the behavior of stars in the center of the Milky Way is due to the scattering/absorption of light by the gases and dust that accumulate in these centers, making it very difficult to distinguish one star from another. Approximately 3.000 stars have been detected within $10''$ of the galactic center during the last three decades of observation (SAKAI et al., 2019). Among them, the star which behavior has been most investigated so far is S0-2. One of the most remarkable results involving this star was the detection of Schwarzschild precession in its orbit (ABUTER et al., 2020).

To understand about this precession, we can remember the problem with Mercury's perihelion deviation. The Newtonian theory of gravitation predicts that the planets in our solar system, for example, must describe closed elliptical orbits around the Sun. However, observations indicate that the orbits of the planets undergo a slight deviation as they pass through perihelion. This phenomenon is more accentuated in Mercury's orbit because of its closest approach to the Sun, however, all the other planets also suffer some deviation in their orbits. The advance that occurs in each orbital period for orbits described in Schwarzschild spacetime is given by (CARROLL, 2004)

$$\Delta\phi \approx 3\pi \left(\frac{2GM}{(1-e^2)a} \right) = \frac{3\pi r_s}{(1-e^2)a}, \tag{2.2}$$

where G is the universal gravitational constant, M is the mass of the planet, a is the semi-major axis of the ellipse, e is the eccentricity and r_s is called the Schwarzschild radius. For Mercury, whose

parameters are $r_s = 2.96 \ \times 10^3$ m, $a = 5.79 \ \times 10^{10}$ m and $e = 0.2056$ we are left with

$$\Delta\phi \approx 0,103 \quad \text{arcsec/orbit.} \tag{2.3}$$

In general we consider the precession by century and then we have

$$\Delta\phi \approx 43 \quad \text{arcsec/century.} \tag{2.4}$$

Figure 2 illustrates this phenomenon and indicates the perihelion deviation $\Delta\phi$ and the distances of the periastron and apoapsis, r_{min} and r_{max}, respectively.

Figure 2 – Illustration of the Schwarzschild precession. This figure represents an amplified view of the precession present in orbits predicted by general relativity. With each passage of the smaller object through the periastron, its orbit undergoes a slight deviation, forming a rosette instead of following a closed elliptical orbit.

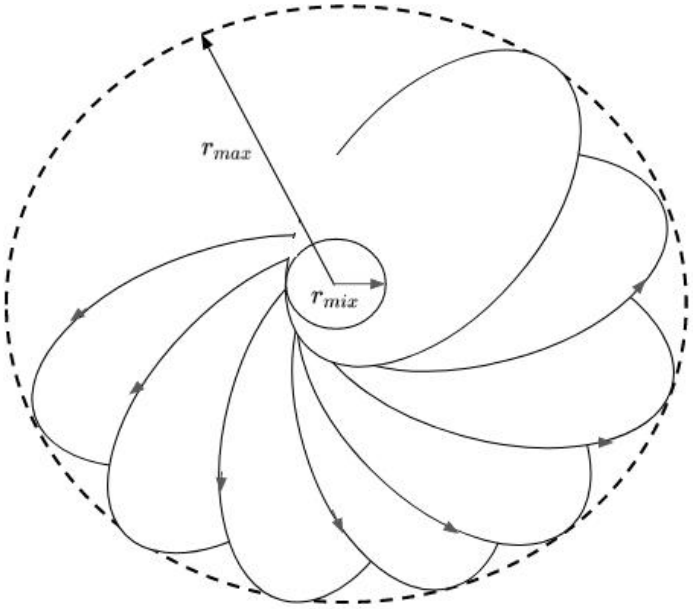

Image source: (CATTANI, 2010).

Along the twenty seven years of observations made by the European Southern Observatory (ESO) team (ABUTER et al., 2020), it was possible to observe the passage of the star S0-2 on its closest approach to the supermassive black hole called Sagittarius A*. The team, led by Frank Eisenhauer from MPE (Max Planck Institute for Extraterrestrial Physics), had the participation of Stefan Gillessen (MPE) leading the analysis of numerous information collected about the orbit of S0-2. The result obtained was that the orbit of this star is not closed, as expected in Newtonian gravitation, but precesses following an orbit in the form of a rosette. This phenomenon has never been observed in a star orbiting a black hole and the precession detected was $12'$ per orbital period.

Figure 3 shows the results obtained in the first analysis of the data. The gray trajectory describes the best fit for GR and the $\times$ marks the system's center of mass. In this figure is possible to see at the top that the orbit does not close due to precession.

Figure 3 – Observational results of the Schwarzschild precession in the star S0-2: In this figure we can see the path taken by the star S0-2 in its orbit around the supermassive black hole present at the center of the Milky Way. After reaching its closest approach to Sagittarius A*, the orbit undergoes a deviation and does not close. Observational measures are also compatible with the values predicted in GR

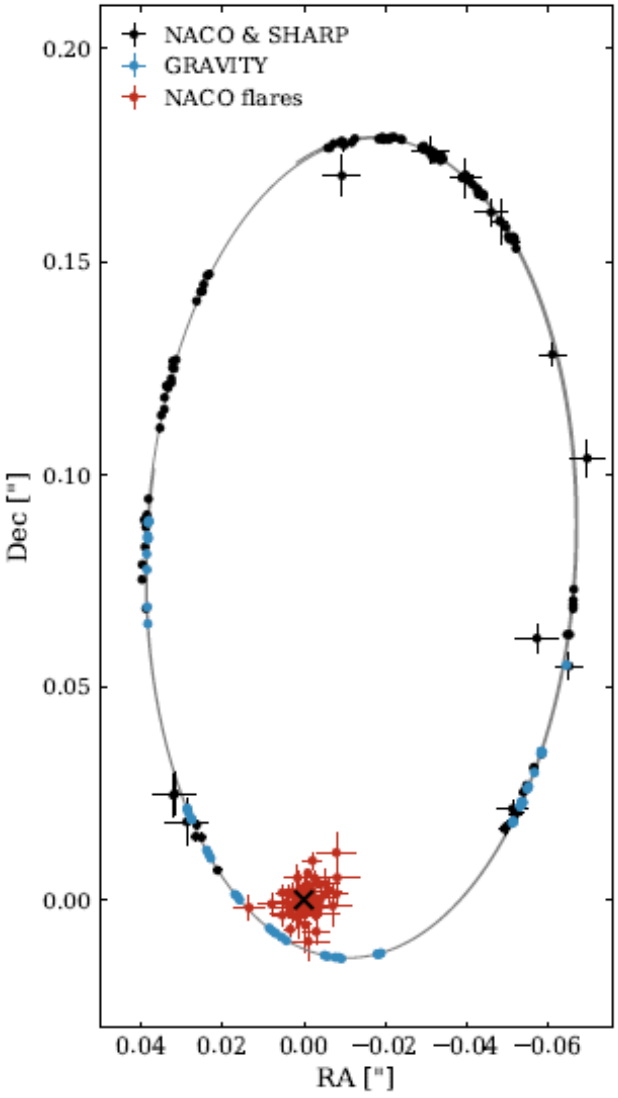

Image source: (ABUTER et al., 2020).

This discovery highlights the validity of GR that predicts precessing orbits and, in addition, the theory has also been shown to be compatible with the measurements of the precession. A good understanding of the behavior of S0-2 (and other stars in the galactic center) can help us to accurately estimate the mass of Sagittarius A* and consequently the total mass existing in the center of the galaxy. This information is important in the search for other smaller black holes and other compact objects.

2.2 TESTS IN THE STRONG FIELD LIMIT

There are still other interesting tests in the weak field limit, however we will focus on tests in the strong-field regime, where we will discuss the nature of gravitational waves and important discoveries

that have contributed to improving our understanding of black holes.

We will start this section by discussing the coalescence of binary black holes (BBH), its main characteristics and how gravitational waves carry important information about each individual black hole. Subsequently, we will analyze in more detail some of the most important events in the Gravitational-Wave Transients Catalog (GWTC-3) with which we will be able to conclude once again about the validity of the GR.

2.2.1 Coalescence of Binary Black Holes

As previously seen, there is strong evidence that black holes are indeed spread across the universe. We mentioned the dynamic movement of stars in galactic centers but we can also find black holes by searching for the gravitational waves emitted by them during the process of coalescence.

We will start by introducing some simplifications to the problem of coalescence. First of all, sometimes a black hole is considered to have an accretion disk, and it can be used to illustrate the binary system loss of energy by mechanisms other than the emission of gravitational waves. Furthermore, we can consider that long before the coalescence the two black holes were far enough apart and, so, they can be described by the Kerr metric and that the gravitational waves emitted are small perturbations in spacetime. The Kerr metric is used to describe the spacetime around black holes with some angular momentum. It will be mentioned several times in this work since it is assumed that real black holes must have spin. This is due to the fact that in the process of formation of a primary black hole, the generating star has spin. Therefore, it is much more likely to find black holes with some angular momentum than stationary black holes - such as those described by the Schwarzschild metric. Finally, we consider that the black hole formed after the merger eventually stabilize into a Kerr black hole again. With that in mind, we are able to classify some stages and analyze the characteristics of the merger. We can subdivide the problem into four stages: Newtonian, Inspiral, Merger and Ringdown.

Newtonian Stage: At this stage the black holes are so far apart that the gravitational waves emitted are not enough to start the coalescence process. Thus, for the merger to actually happen, some other phenomenon outside the binary needs to occur, such as the interaction with some gas and dust.

Inspiral Stage: When the binary reaches this stage, gravitational wave emission become the dominant process that drives the black holes closer and closer together. The closer they get, the faster they move and more energy is lost in the form of gravitational waves. This phase is very well modeled by Post-Newtonian (PN) methods.

Post-Newtonian formalism is a calculation tool that expresses Einstein's (non-linear) equations in terms of the lowest-order deviations from Newton's law of universal gravitation. This allows approximations to Einstein's equations to be made in the case of weak fields. Some of these post-Newtonian approximations are expansions by a small parameter, which is the ratio of the velocity of the matter forming the gravitational field to the speed of light. In the limit, when this parameter is null, the post-Newtonian expansion reduces to Newtonian gravitation (WILL, 1993).

Merger: At this stage, the emission of gravitational waves becomes strong enough to force the black holes to come together to form a single final black hole. This process is very fast and to fully understand this stage it is necessary to use numerical simulations (NS).

Ringdown: After the merger, the remaining black hole is in the Ringdown stage, where spacetime can be described by the Kerr metric with some perturbation. Given the appropriate initial conditions, this stage can be calculated using perturbative techniques.

In addition to the characteristics of each stage of coalescence, black holes can also perform more or less eccentric orbits and this is an important parameter to correctly perform simulations of this problem, in addition to the mass and spin values of each black hole. The paper (PRETORIUS, 2007) discusses the results obtained from numerical simulations of four categories of BBH. These categories are: (1) binaries with equal mass, small eccentricity and spin; (2)different mass, small eccentricity and spin; (3) equal mass, non-negligible spin and small eccentricity and (4) equal mass, large eccentricity and minimum spin. We will then see some important results that can help us to understand more about this phenomenon.

For type (1) binaries, the parameters that will characterize the merger are only the mass and final spin of the remaining black hole. The energy emitted during the Merger and Ringdown stages is theoretically expected to add up to 3.5% of the total energy of the system. Moreover, an additional 1.5% of the available energy would be radiated before these stages, so 5% of the total energy is converted in gravitational waves during the entire merger event (PRETORIUS, 2007). However, observational data suggest slightly lower values for this loss. Figure 4 illustrates the behavior of binaries of this type.

We can see in the first row of Figure 4 that there is some emission of gravitational waves that can take the binary to the next stage. Then the black holes continue orbiting each other until they enter the Inspiral stage (fourth row) and then quickly move from Merger (center of the fifth row) to Ringdown (last frame of the fifth row and first two frames of the last row). Finally, the spacetime around the remaining black hole can be described by the Kerr metric. Purple colors indicate the peak of gravitational wave emission. The shape of the emitted wave, its characteristics and effects when interacting with matter will be discussed in the chapter 3 .

In case (2), some characteristics of the merger and the waveform change from the previous case, for example, equal masses maximize the total energy emitted and also maximize the final spin of the remaining black hole.

If the merger happens between rotating black holes, as indicated in case (3), the amount of radiated energy can greatly change from case (2) and, consequently, there will be changes in the mass and spin of the remaining black hole. The black holes of the binary can also present spin either in the same or opposite directions. So, due to the Frame Dragging effect, one black hole can affect the movement of the other, depending on the spin directions of each one. Frame Dragging is a phenomenon that appears around rotating black holes because the movement of these objects forces spacetime to be dragged around them, creating a region where any object (and even light) is forced to move in the same direction of the black hole's rotation. At last, when an orbit results in asymmetrical patterns of gravitational wave emission, it can happen that the remaining black hole is pulled away from the region where the merger occurred and continue moving to distant regions.

The first complete binary black hole (BBH) merger to be simulated (PRETORIUS, 2005) had the characteristics of case (4). For this, highly compact concentrations of energy were chosen as the initial condition. Some other simulation studies can be found at: (HANNAM et al., 2008),(CAMPANELLI et

Figure 4 – Stages of binary black hole coalescences: This figure represents the result obtained from a relativistic numerical simulation (PRETORIUS, 2007). The purpose was to study the energy loss of the binary due to the emission of gravitational waves. It highlights the main characteristics of each phase of coalescence. We can see how the Inspiral stage is much longer than the merger and the purple and orange colors indicate the increase in the emission of gravitational radiation.

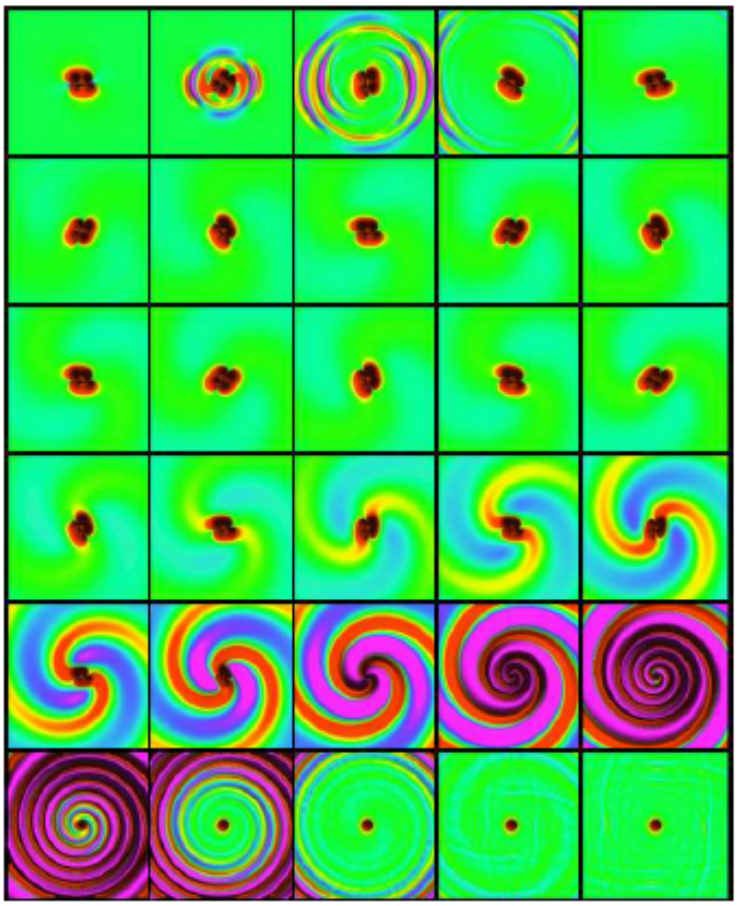

Image source: (PRETORIUS, 2007).

al., 2006),(BAKER et al., 2006),(BAKER et al., 2007).

Now that we have an overview of how the coalescence process of BBH works, we can study some of the main gravitational wave detections made by the LIGO-Virgo-KAGRA collaboration during the first three observing runs (called O1, O2 and O3a+O3b) and see how this data is used to test GR at strong field limits.

2.2.2 First gravitational wave detection: GW150914

On November 14, 2015 the LIGO observatories (one site in Hanford and the other in Livingston, USA) recorded for the first time a gravitational wave signal (ABBOTT et al., 2016). Named GW150914, the signal contains the first direct evidence of the existence of black holes.

To reach this conclusion, an extensive and thorough analysis of the signal was required. We will have a more detailed discussion of detectors and the signal analysis process later in this work. In this section we will only make a general interpretation of the first detection in order to introduce some

ideas that will be fundamental in the subsequent discussions.

Figure 5 shows, respectively, the spectrogram and the waveform of the gravitational wave after the signal be processed. In the left panel we can see the presence of a transient signal. The colors closest to yellow indicates that the signal has greater power than the noise present in the sample. It is worth noting that this signal is extremely short, lasting less than one second, and that its frequency varies significantly over time. In the right panel we have the representation of the gravitational waveform (in blue the data from the Livingston detector and in red the data from the Hanford detector). Here we can see how the amplitude also increases near the end of the signal. In chapter 5 we will see more details of plots like these.

Figure 5 – Signal of the first detection of gravitational waves after noise extraction: The spectrogram is used to show which parts of the signal have the greatest power (indicated by the yellow color). We can see how the gravitational signal stands out from the noise. On the right, we have the waveform of the gravitational wave detected and the peak of gravitational radiation emission during the merger is very evident

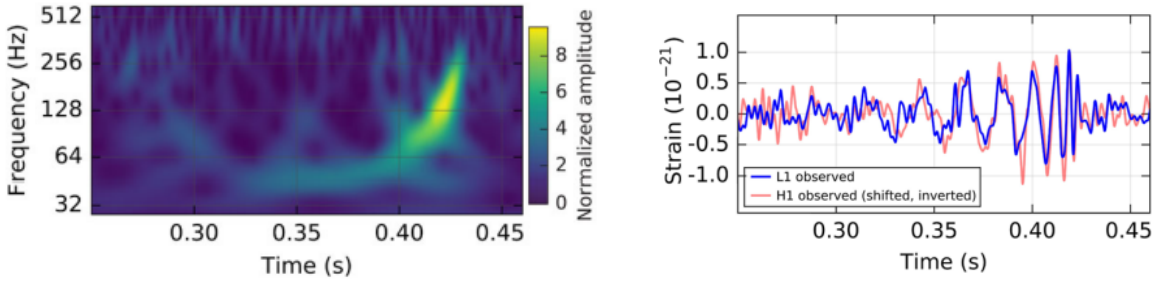

Image source: (ABBOTT et al., 2016).

These characteristics are very relevant to identify the origin of this gravitational wave. This is due to the fact that each type of source will generate a signal with very different characteristics in the detector. This transient, short-lived signal of rapidly increasing frequency and amplitude is not a characteristic signal of a single rotating object or even of two objects orbiting each other with a fixed orbital separation (as described earlier by the Newtonian stage). The only way to explain this result is to consider that there are two objects orbiting each other and approaching each other with time (ABBOTT et al., 2016). The closer they get, the faster they move and, consequently, the gravitational disturbance produced will be more intense. With that we can have the first important conclusion: it is a binary system.

To extract more information from this system, we can initially assume that $m_1 \geq m_2$ and then we can look for the mass of the objects that constitute the binary. To describe the emission of gravitational wave by a binary system, we use the chirp mass ($\mathcal{M}$) given by (ABBOTT et al., 2016)

$$\mathcal{M} = \frac{(m_1 m_2)^{3/5}}{(m_1 + m_2)^{1/5}}. \tag{2.5}$$

The measured mass is slightly different from the actual mass value of the object acting as a source. This measured value with deviation is called a "chirp". The same goes for frequency. If we then use Newton's laws of motion, for universal gravitation, and take Einstein's quadrupole formula, we will be

able to estimate that the chirp mass will be $\mathcal{M} = 30M_{\odot}$ (ABBOTT et al., 2016). We can also calculate the orbital separation between these two objects and we will see that it is only twice the sum of the Schwarzschild radius of each object, i.e., they are very close to each other, a distance that would be impossible for a binary of stars to be reached without it merging.

Figure 6 – Behavior of the GW150914 in each stage of coalescence (ABBOTT et al., 2016): Comparison of the waveform with the binary coalescence stages. Here it becomes clear how the closer proximity between black holes increases the orbital speed and, consequently, increases the emission of gravitational waves, in which the peak occurs during the merger.

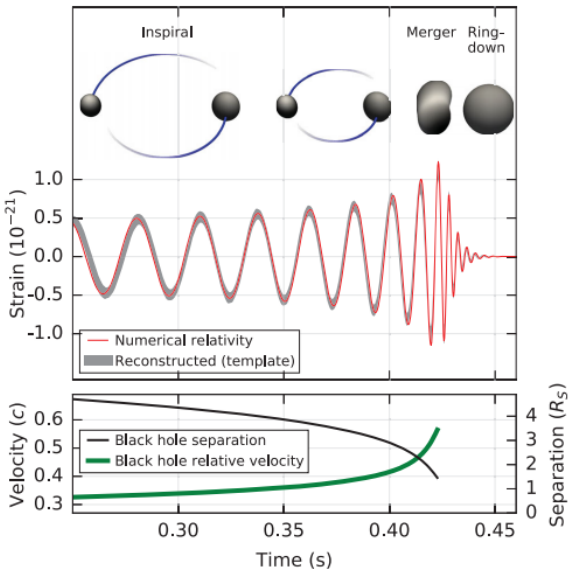

Image source: (ABBOTT et al., 2016).

These are two strong evidences that the source is a binary system of very compact objects and the values obtained reinforce that these must be black holes (since such values have never been measured for neutron stars, for example). With the complete analysis of the data, it was concluded that the masses are $36M_{\odot}$ and $29M_{\odot}$ (ABBOTT et al., 2016), very close to what we expected through simple arguments.

Figure 6 illustrates very well the previous discussion about the BBH coalescence and how the gravitational wave signal is very characteristic in each stage. We can see in the upper panel that during the inspiral stage, the gravitational wave practically does not have variations in amplitude and the frequency only starts to increase very quickly near the merger, where it reaches its maximum value. After that begins the Ringdown where the remaining black hole begins to stabilize. In the bottom panel we see how velocity and orbital separation vary with time.

Now we will study some of the main GR tests performed from the detections confirmed so far.

2.2.3 Tests of General Relativity with GWTC-3

During the first observing run, called O1 (from 12 september 2015 to 19 january 2016) only LIGO observatories were active. At the end of O2 (from 30 november 2016 to 25 august 2017) the Virgo observatory in Italy joined the LIGO observatories, significantly improving the reliability of the data collected. More recently, from 01 april 2019 to 30 september 2019, occurred the first part of the third

observing run (O3a), with an advanced version of the three observatories. Finally, the second part of O3, called O3b, occurred from 01 november 2019 to 27 march 2020, and for the analysis of the detections the KAGRA observatory in Japan joined the collaboration.

The data collected during O1 form the GWTC-1 catalog (ABBOTT et al., 2019), which contains information about 11 events, which are BBH and neutron star- black hole (NSBH) coalescences, where GW170817 (ABBOTT et al., 2017) is one of the most important events. The great importance of the merger of these two neutron stars comes from the fact that it was the only event to date that was also observed in the entire electromagnetic spectrum and, therefore, it was the event with the greatest amount of data collected. With the new detections carried out during O2, the GWTC-1 catalog was updated and named as GWTC-2 (ABBOTT et al., 2021a). Shortly after, new detections from O3a and O3b were released, creating the GWTC-2.1 and GWTC-3 catalogs (COLLABORATION et al., 2021a), the latter being the most comprehensive set of gravitational wave observations presented to date. This catalog contains all 90 detections confirmed so far, as shown in Figure 7. Some of the events stand out, such as: GW190814 (ABBOTT et al., 2020), GW190521 (ABBOTT et al., 2020) and GW200129_065458 (COLLABORATION et al., 2021a). The first one was the merger of a 23 $M_\odot$ black hole with a 2.6 $M_\odot$ object. According to the LIGO-Virgo collaboration (ABBOTT et al., 2020), this second object is more likely to be the lightest black hole ever detected rather than the heaviest neutron star. However, this event (and some others very similar) is still of unknown origin.

The second one, GW190521, was the merger of two black holes (85 $M_\odot$ e 66 $M_\odot$), but what stands out in this merger is the mass of one of the components of the binary. There is a mass range for stars in which we know that when they collapse, the result is guaranteed to be a black hole. Thus, there is an upper and lower limit to the masses of black holes that can be formed by these collapses. These objects are called primary black holes. Above a certain value, a black hole will only exist if it is formed by some other mechanism or if it is a second/third generation black hole, i.e., a black hole generated by the merger of two other primary black holes. This problem is known as Pair-instability supernova (LEUNG; NOMOTO; BLINNIKOV, 2019). Then, apparently, the merger took place between a primary and a secondary black hole and that raises some questions about the formation of binary systems like this. The resulting black hole from the GW190521 event was the second most massive detected to date. Finally, the event GW200129_065458 shows a bimodality in mass ratio, which is not expected. Multimodality can arise, e.g., due to the presence of glitches or multiple overlapping signals in the data although the latter option is most unlikely given O3 sensitivity.

These events help us to understand more about black holes physics and we can also use them to test theories of gravitation, especially General Relativity. Among the tests performed by the LIGO-Virgo-KAGRA (LVK) (COLLABORATION et al., 2021b) collaboration, we will mention four of them: two consistency tests, namely residual test and the IMR test; the PPN test and the polarization test.

The idea of the first consistency test, called the residual test, is quite simple: subtract the best-fit model from the data and ensure that the residual signal have the expected statistical properties of instrumental noise. For this test to be clearer, we need to take into account an important part of the analysis. GR allows us to predict how would be the waveform of gravitational waves emitted by different types of sources. With this information we can build a database or bank with the expected

Figure 7 – Gravitational wave merger detections: In this figure we have the representation of all the binaries detected to date (upper panel). We can see the values of the masses of the objects individually and the value of the mass of the remaining black hole. We can also see which of the objects are black holes, neutron stars and which are unknown (see "Key") in addition to being ordered according to the observing run in which they were detected. In the lower left panel we only have the zoom of some events to exemplify the use of the key.

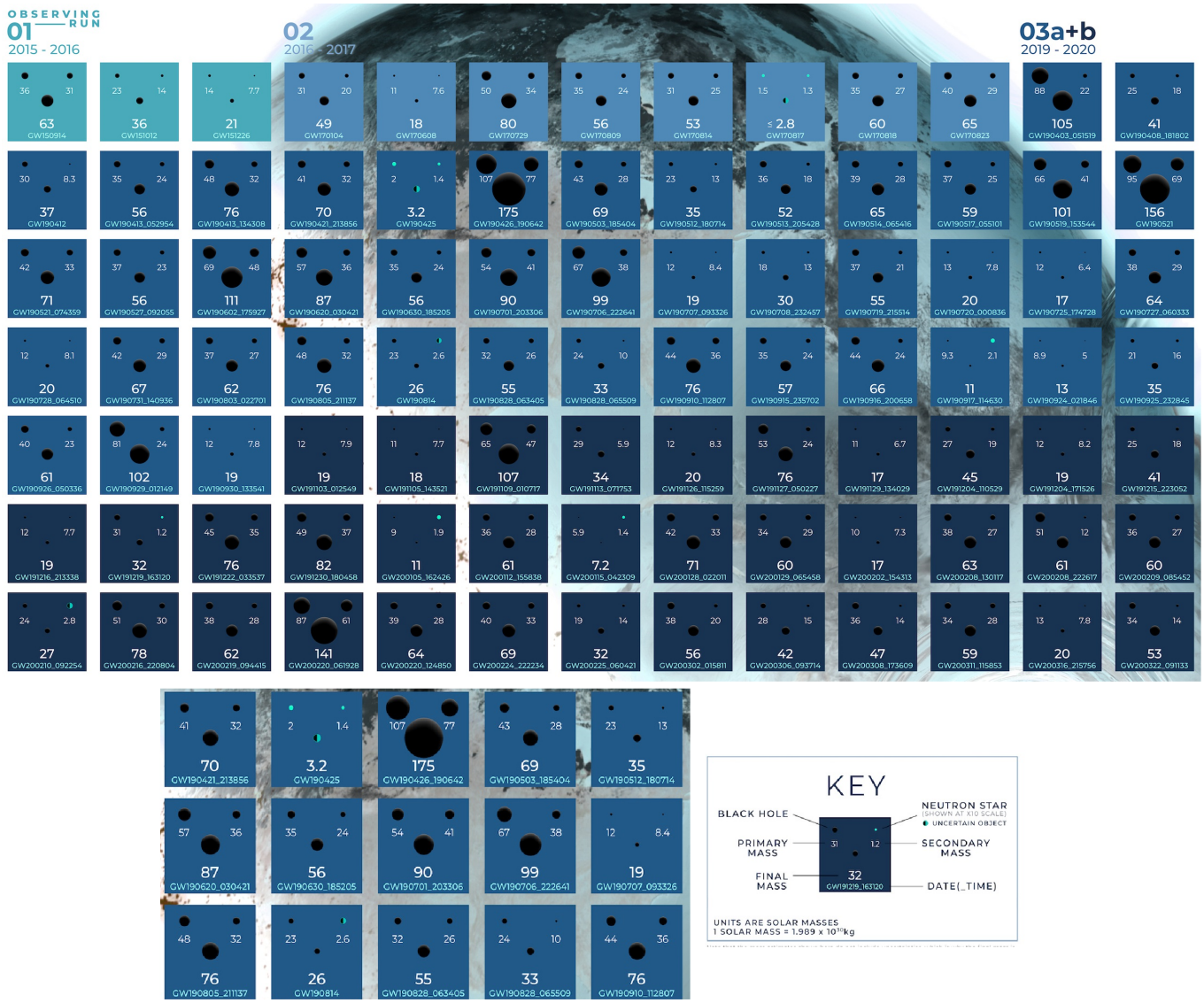

Image source: (LIGO-CALTECH, 2021)

characteristics of the signal. These reference files are called templates. Then, when a signal is detected, we can compare our models with the observational data. In addition, it is also possible to determine which are the main sources of noise in the detector and in which frequency ranges these noises predominate (we will see some details about noise in later section). So, the residual test uses these templates, the noise information and the data collected to verify how accurate the theoretical prediction was.

The second test is the Inspiral-Merger-Ringdown (IMR) consistency test. In GR, it is expected that the estimated values for the mass and spin of the remaining black hole are compatible if we use separately the inspiral stage data and the post-inspiral stage data. So this test consists of estimating the

mass and spin values of the remaining black hole from these two independent portions of the signal (at low and high frequencies) and then comparing the values obtained.

Another important test is the parametric test of the generation and propagation of gravitational waves. We have seen that the inspiral stage can be described by a post-Newtonian approximation. To measure GR deviations in this domain, two waveform models called $IMRP_{HENOM}P_V2$ and $SEOBNR_V4$ are used. In this work we will not go into details about these models. More complete information can be found in (ABBOTT et al., 2021b).

Finally, polarization tests helps us to identify whether the signal contains information from polarization modes different from those predicted in GR. In GR, two tensor modes are predicted, called "$+$" polarization and "$\times$" polarization, but other theories of gravitation can predict up to six distinct modes. In chapters 3 and 4 we will see about these polarizations in more details.

No research to date has found any violations of GR. Other theories are also being tested, for example, the massive gravity, and much physical information has been extracted from analyzes such as those mentioned in this work. A new observation run is scheduled to start in mid-December 2022 with LVK. It is also expected that in the future, with the development of space observatories such as LISA (Laser Interferometer Space Antenna), we will be able to study further in the universe, an increasing number of events with a precision also much higher than the previous ground-based observatories have.

3 REVISITING GENERAL RELATIVITY RESULTS

Still in the context of General Relativity (GR), we are going to review some important definitions about gravitational waves so we can finally work with modifications of this theory. For this, we will start in the section 3.1 with a brief discussion of the main sources of gravitational radiation . Next (3.2), we will start with the linearization of Einstein's field equations and see in the section 3.3 how the gravitational waves polarization modes are in GR.

3.1 SOURCES OF GRAVITATIONAL WAVES

So far we have seen that the process of binary black holes (BBH) coalescence emits gravitational waves that we can detect on Earth through observatories such as LIGO. However, there are several sources of gravitational waves in the universe. In this section we will study the main sources.

Still in the context of coalescence, not only BBH mergers will be responsible for the generation of gravitational waves. The merger of neutron star binaries (NSB) or neutron star-black hole binaries (NSBH) will also produce gravitational waves strong enough for us to detect on Earth. However, lighter objects will cause a distortion in spacetime that can be considered negligible. In this way, we could also produce gravitational waves in laboratory, but again, they would be negligible. To make this clearer, we can exemplify with the dimension of the amplitude of the gravitational wave generated by the merger of black holes. We know that the waves detected so far have a peak around 10^{-21}. The displacement at the detector's arms is about 40000 times smaller than a proton diameter. For this reason, this thesis will only deal with those sources which gravitational waves are significant and detectable here on Earth (or the ones that we hope to be able to detect in the future with space observatories such as LISA). We can divide these sources into three categories: periodic sources, burst sources and stochastic sources.

Periodic sources are those that produce approximately continuous gravitational waves. As an example we can cite binaries of compact objects in the Newtonian stage, that is, objects that are orbiting each other without entering the inspiral phase. Since the energy loss is very small compared to the gravitational waves detected will have an approximately constant pattern and will appear on the detector throughout the observation period. Due to their constancy and low intensity, these waves are very difficult to detect and require a network of detectors to confirm that the signal is indeed astrophysical and not instrumental noise, given that, if the signal is indeed from astrophysical origin, it must appear on all detectors with enough sensitivity that are simultaneously in observation mode. Furthermore, noise from instrumental origin is not expected to have exactly the same characteristics in different detectors. Another example of such sources are pulsars (rapidly rotating neutron stars) with some asymmetry in their shape or with an axis of symmetry different from the axis of rotation.

On the other hand, Burst-type sources are those associated with very energetic and short-duration events, so the gravitational wave will appear in the detector as a transient signal with frequencies that grow very quickly. As an example we can mention the mergers of compact objects and the core collapse of very massive stars. The first example has already been extensively explored in this work because only the gravitational waves produced by these processes have been detected so far. It is expected that

ground-based observatories will also be able to detect gravitational waves from supernovae, however, there is still no evidence of these events in the analyzed data from the first three observing run. An important detail about these signals is that, although we expect that the more general characteristics of the waves produced by these events will be the same, wave form will be different for each case, i.e., it is expected that the signal coming from the merger of supermassive black holes is shorter and with a more intense frequency variation than generated by the merger of neutron star binaries. So far, the LVK collaboration has a large number of well-established waveforms templates for compact binary merger event but there is still a lot of research to be done to develop templates that model the signals coming from different sources.

Finally, stochastic sources are those that involve multiple sources. There are situations, as in the case of galactic centers, in which there is a large concentration of different objects and phenomena generating gravitational waves that overlap both in time and in frequency. Then, in this case, there will be some kind of "gravitational wave background ", just like it happens with cosmic microwave background. Because they have even smaller amplitudes than those produced by Burst-type sources, these waves cannot be detected by current observatories. We would need the detectors to be much larger so that they could achieve the required sensitivity. Therefore, we expect that gravitational waves of this type will be detected in the future by the LISA observatory.

3.2 EQUATIONS OF MOTION AND GAUGE INVARIANTS

In order to find a definition for the polarizations of the gravitational waves, we must start with a definition for the gravitational wave itself. Previously we saw that these waves are small perturbations in spacetime generated by the motion of massive objects. This perturbation will be described by the tensor $h_{\mu\nu}$ and will be given by

$$h_{\mu\nu} \equiv g_{\mu\nu} - \eta_{\mu\nu}, \tag{3.1}$$

where $g_{\mu\nu}$ is the spacetime metric and $\eta_{\mu\nu}$ is the Minkowski plane metric. Some important definitions for this work are: $\eta_{\mu\nu} = diag(-1, 1, 1, 1)$, $(x^0, x^1, x^2, x^3) = (t, x, y, z)$, $\partial_\mu = \frac{\partial}{\partial x^\mu}$, $\Box \equiv \partial^\mu \partial_\mu$ is the D'Alambertian operator and $\nabla^2 \equiv \delta^{ij}\partial_i\partial_j$ is the Laplacian. Furthermore, the symmetrizations are given by $T_{(\mu\nu)} \equiv \frac{1}{2}\left(T_{\mu\nu} + T_{\nu\mu}\right)$; $T_{[\mu\nu]} \equiv \frac{1}{2}\left(T_{\mu\nu} - T_{\nu\mu}\right)$ and we rise and lower the indices with the background metric $\eta_{\mu\nu}$.

We will see that gravitational wave observatories are based on the idea that, when interacting with matter, this perturbation $h_{\mu\nu}$ will produce detectable effects. If we want, for example, to detect the effect that the passage of a gravitational wave will have when it hits two neighboring particles at rest, we just need to measure the spatial separation between these particles. We know that their motion will be described by the geodesic deviation equation given by

$$\ddot{\zeta}^i = -R^{i\ (1)}_{0j0}\zeta^i, \tag{3.2}$$

where $R^{i\ (1)}_{0j0}$ is the first order Riemann tensor and the points indicates derivatives with respect to $x^0 = t$. Then it will be possible to show that the relative separation between the particles will change due to

the passage of the gravitational wave (TACHINAMI; TONOSAKI; SENDOUDA, 2021).

We will then evaluate the behavior of gravitational radiation by finding the physical degrees of freedom existing in the theory and we will do this using the gauge invariant formalism. We will start from the fact that $h_{\mu\nu}$ is a symmetric tensor and, therefore, we can decompose it into three parts: a scalar h_{00}, a vector h_{0i} and a tensor h_{ij}. Next, we will use the Helmholtz decomposition, which guarantees that a vector field $\vec{F}$ can be decomposed into two parts: one where the curl is null ($\vec{\nabla} \cdot \vec{W} = 0$) and another one where the divergence is null:

$$\vec{F} = \vec{W} + \vec{\nabla}\phi. \tag{3.3}$$

Following this decomposition, we can write the field $h_{\mu\nu}$ as follows ((CARROLL, 2004)):

$$h_{00} = 2\phi, \tag{3.4}$$

$$h_{0i} = B_i + \partial_i S, \tag{3.5}$$

$$h_{ij} = 2\delta_{ij}\Psi + 2\partial_i\partial_j E + \partial_i F_j + \partial_j F_i + h_{ij}^{TT}, \tag{3.6}$$

where $\partial^i B_i = 0$, $\partial^i F_i = 0$, $\partial^i h_{ij}^{TT} = 0$, $\eta^{ij} h_{ij}^{TT} = 0$ e Ψ and E are scalars. With that, we have

$$h = -2\phi + 6\Psi + 2\nabla^2 E. \tag{3.7}$$

We also know that, according to an infinitesimal coordinate transformation, this field transforms as follows:

$$h_{\mu\nu} \to h_{\mu\nu} + \partial_\mu \xi_\nu + \partial_\nu \xi_\mu. \tag{3.8}$$

Applying the decomposition to the gauge field ξ_μ we have

$$\xi_0 = \xi_0, \tag{3.9}$$

$$\xi_i = \xi_i^D + \partial_i \xi^R, \tag{3.10}$$

where $\partial^i \xi_i^D = 0$. Combining (3.9) and (3.10) to the transformations of the field $h_{\mu\nu}$, we have (see appendix A)

$$\widetilde{h}_{00} \equiv 2\widetilde{\phi}, \tag{3.11}$$

$$\widetilde{h}_{0i} \equiv \widetilde{B}_i + \partial_i \widetilde{S}, \tag{3.12}$$

$$\widetilde{h}_{ij} \equiv 2\delta_{ij}\widetilde{\Psi} + 2\partial_i\partial_j \widetilde{E} + \partial_i \widetilde{F_j} + \partial_j \widetilde{F}_i + \widetilde{h}_{ij}^{TT}, \tag{3.13}$$

where ˜ indicates the transformed fields. So we are left with the following gauge invariants:

$$\tilde{\phi} = \phi + \partial_0 \xi_0, \tag{3.14}$$

$$\tilde{\Psi} = \Psi, \tag{3.15}$$

$$\tilde{S} = S + \partial_0\, \xi^R + \xi_0, \tag{3.16}$$

$$\tilde{E} = E + \xi^R, \tag{3.17}$$

$$\tilde{h}_{ij}^{TT} = h_{ij}^{TT}, \tag{3.18}$$

$$\tilde{F}_i = F_i + \xi_i^D, \tag{3.19}$$

$$\tilde{B}_i = B_i + \partial_0\, \xi_i^D. \tag{3.20}$$

Thus we can combine these gauges to find new invariants and then we have:

- Combining ϕ, S and E, we get (see appendix A)

$$D = \phi - \partial_0 S + \partial_0^2 E. \tag{3.21}$$

- Combining B_i and F_i, we have directly that

$$H_i = B_i - \partial_0 F_i. \tag{3.22}$$

Now that we have the gauge invariants, we can write the field equations in terms of them. To do so, we must first write the Ricci tensor. Then its components will be given by ((CARROLL, 2004))

$$R_{00} = n^{ij}\partial_0\partial_j h_{0i} - \frac{1}{2}\left(\partial_0\partial_0 h + \partial_0\partial_0 h_{00} + \nabla^2 h_{00}\right), \tag{3.23}$$

$$R_{0i} = \frac{1}{2}\left(-\partial_0\partial_i h_{00} + \eta^{jk}\partial_j\partial_i h_{0k} + \eta^{jk}\partial_j\partial_0 h_{ki} - \partial_0\partial_i h - \nabla^2 h_{0i}\right), \tag{3.24}$$

$$R_{ij} = -\frac{1}{2}\left(\partial_0\partial_i h_{0j} + \partial_0\partial_j h_{0i} - \eta^{kl}\partial_k\partial_j h_{li} - \eta^{kl}\partial_k\partial_i h_{lj} - \partial_i\partial_j h + \Box h_{ij}\right). \tag{3.25}$$

Knowing that without source, the field equations are reduced to $R_{\mu\nu} = 0$, we can use the decomposition of $h_{\mu\nu}$ to rewrite the previous equations. So we are left with

- from R_{00}, we have:

$$n^{ij}\partial_0\partial_j h_{0i} - \frac{1}{2}\left(\partial_0\partial_0 h + \partial_0\partial_0 h_{00} + \nabla^2 h_{00}\right) = 0, \tag{3.26}$$

$$-3\partial_0\partial_0\Psi - \nabla^2 D = 0. \tag{3.27}$$

- from R_{0i}, we have:

$$\frac{1}{2}\left(-\partial_0\partial_i h_{00} + \eta^{jk}\partial_j\partial_i h_{0k} + \eta^{jk}\partial_j\partial_0 h_{ki} - \partial_0\partial_i h - \nabla^2 h_{0i}\right) = 0, \tag{3.28}$$

$$\nabla^2 H_i - 4\partial_0\partial_i\Psi = 0. \tag{3.29}$$

- from R_{ij}, we have:

$$-\frac{1}{2}\left(\partial_0\partial_i h_{0j} + \partial_0\partial_j h_{0i} - \eta^{kl}\partial_k\partial_j h_{li} - \eta^{kl}\partial_k\partial_i h_{lj} - \partial_i\partial_j h + \Box h_{ij}\right) = 0, \tag{3.30}$$

$$\partial_0\partial(_i H_j) - 2\partial_i\partial_j D + 2\left(\Box\delta_{ij} + \partial_i\partial_j\right)\Psi + \Box h_{ij}^{TT} = 0. \tag{3.31}$$

If we take the trace of (3.31), an additional constraint is found:

$$\nabla^2 D = \left(3\Box + \nabla^2\right)\Psi. \tag{3.32}$$

It can be shown that the field (and trace) equations take the following form:

$$\nabla^2\phi = -3\partial_0\partial_0\Psi, \tag{3.33}$$

$$\nabla^2 B_i = -4\partial_0\partial_i\Psi, \tag{3.34}$$

$$\Box h_{ij}^{TT} = -\partial_0\partial(_i B_j) + 2\partial_i\partial_j\phi - 2\left(\Box\delta_{ij} + \partial_i\partial_j\right)\Psi, \tag{3.35}$$

$$\nabla^2\phi = \left(3\Box + \nabla^2\right)\Psi. \tag{3.36}$$

Combining (3.33) and (3.36), we have

$$\nabla^2\Psi = 0, \tag{3.37}$$

and therefore $\Psi = 0$ (since Ψ is localized given that $h_{\mu\nu}$ is also localized). As a result, the other equations are ((CARROLL, 2004))

$$\nabla^2\phi = 0, \tag{3.38}$$

$$\nabla^2 B_i = 0, \tag{3.39}$$

$$\Box h_{ij}^{TT} = -\partial_0 \partial({}_i B_j) + 2\partial_i \partial_j \phi, \tag{3.40}$$

from which follows that $\phi = 0$ and $B_i = 0$. Therefore,

$$\Box h_{ij}^{TT} = 0. \tag{3.41}$$

The previous equation has a solution of the type $h_{\mu\nu} = C_{\mu\nu} e^{ik_\sigma x^\sigma}$ which is the equation for a transverse plane wave, where $C_{\mu\nu}$ is a symmetric, purely spatial, traceless tensor and k_σ is the wave vector (CARROLL, 2004) .

3.3 POLARIZATIONS

We can go back to the equation for the geodetic deviation and write the field $\varepsilon_{ij} = R_{0i0j}$, as a linear combination of two polarization tensors (TACHINAMI; TONOSAKI; SENDOUDA, 2021):

$$\varepsilon_{ij} = -\frac{1}{2}\ddot{h}_+ e_{ij}^+ - \frac{1}{2}\ddot{h}_\times e_{ij}^\times. \tag{3.42}$$

The form of these tensors is given by (for a wave traveling along the z -axis):

$$e^+ = \begin{pmatrix} 1 & 0 & 0 \\ 0 & -1 & 0 \\ 0 & 0 & 0 \end{pmatrix} \tag{3.43}$$

$$e^\times = \begin{pmatrix} 0 & 1 & 0 \\ 1 & 0 & 0 \\ 0 & 0 & 0 \end{pmatrix}. \tag{3.44}$$

These tensors represent the basis of the two polarization modes of the gravitational waves, called "$+$" polarization and "$\times$" polarization, with a difference of only 45° between them.

To illustrate how the gravitational wave affects matter, consider a set of particles at rest, arranged in a circle. The Figure 8 and Figure 9 illustrate how the passage of a gravitational wave forces the ring of particles to oscillate into an ellipse. In the upper image we have the representation of the effect of the passage of a wave with polarization $+$ and in the lower panel with polarization $\times$. We see, therefore, that the relative distance between these particles is altered, as previously mentioned, due to the spacetime being stretched and contracted. Further on, we will see that this is the central idea behind the development of gravitational wave detectors such as LIGO. These are the only two modes expected in GR, however, in alternative theories such as massive gravity, the gravitational waves can assume other forms of polarization.

We can then conclude the first part of this work, where we discussed important theoretical aspects about gravitational waves (especially from the perspective of General Relativity) and start a study of

Figure 8 – Polarization "+": The image illustrates the effect of a gravitational wave passing through a ring of particles at rest.

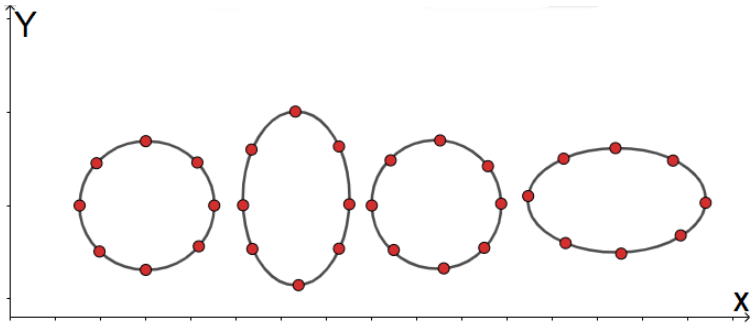

Image source: The author.

Figure 9 – Polarization "×": Cross polarization has a difference of 45° from plus polarization.

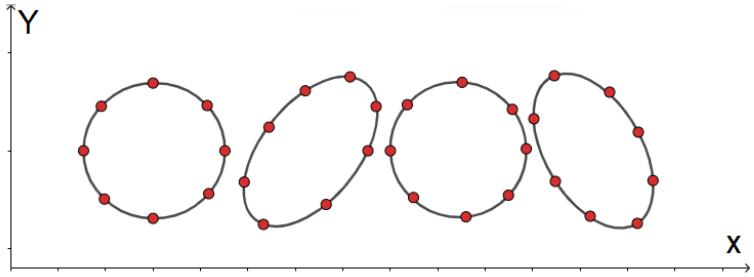

Image source: The author.

this phenomenon in the context of massive gravity to see how the results in this theory differ from General Relativity.

4 MASSIVE GRAVITY

In this chapter we will discuss the propagation of gravitational waves in the context of a massive gravity theory. We will start with a historical motivation in section 4.1 and see what are the main modifications of GR that appear in the Fierz-Pauli theory (4.2). In the next sections, we will see how to use the Stuckelberg trick (4.3) and what are the consequences of applying it to the Fierz-Pauli action. We will do this procedure twice. At first, in section 4.4, we will explicitly study the degrees of freedom existing in the massive theory. Then, in 4.5 we will change the sequence of some procedures performed in the previous section in order to show the vDVZ discontinuity from the start, in the Lagrangian.

4.1 MOTIVATION

Previously, we saw that the Newtonian theory of gravitation needed to be extended in order to explain, for example, the observed value of the perihelion deviation of Mercury. We also saw that the GR theory not only solves this problem, but it also predicts new phenomena, such as gravitational waves, that help us to study gravity in the extreme (such as in the vicinity of black holes). However, GR also needs some modifications because, in certain limits, the theory becomes incompatible with some observational data. As an example, we have the problem of dark matter, dark energy and the problem of incompatibility between gravitation and quantum mechanics. As a result, several theories have emerged in an attempt to extend GR and, among them, the theories of massive gravity. These theories consider the graviton (theoretical particle responsible for transmitting gravitational information) has mass. In theories of this type, four new degrees of freedom (DOFs) appear when compared with GR, i.e., while in GR the gravitational wave has two polarization modes, in massive theories it can have up to five.

The idea of considering a massive graviton began with Markus Fierz and Wolfgang Pauli in mid-1939 (FIERZ; PAULI, 1939). Among the consequences of the inclusion of a massive graviton in the theory, we can mention: the changes in the value of the perihelion advance of the planets, in the propagation speed of gravitational waves and in the orbital decay of binary systems. All these changes are a direct consequence of the appearance of new DOFs in the theory. These differences continue to appear even at the zero mass limit $m \to 0$. This problem, discovered by van Dam, Veltman and Zakharov (DAM; VELTMAN, 1970) (ZAKHAROV, 1970), became known as " the vDVZ discontinuity".

Shortly after that, Boulware and Deser (BOULWARE; DESER, 1972) noticed that the discontinuity was a problem of the linearization of the theory. By entering higher order terms, the discontinuity was fully solved. However, this modification led to a new problem: the appearance of non-physical DOF (negative kinetic energy dependent terms). Which means, while the linear Fierz-Pauli theory has five DOFs, the nonlinear theory has six. This problem became known as ”Boulware-Deser ghost” and it was necessary to develop new theories such as the dRGT (Claudia de Rham, Gregory Gabadadze, and Andrew Tolley) (RHAM; GABADADZE, 2010) (RHAM; GABADADZE; TOLLEY, 2011) to deal with this additional DOF.

We will see in the 4.3 section that this zero mass limit is non-smooth and we will use the Stuckelberg trick to correct this problem. Finally, after establishing the Fierz-Pauli action with the new Stuckelberg fields, we will find the equations of motion that come out of this action. With it we will be able to count the DOFs of this theory and show the vDVZ discontinuity.

4.2 THE FIERZ-PAULI THEORY

We begin our study with a review of the well-established results of the Fierz-Pauli theory. Initially, consider the action for a single massive spin 2 particle, known as the Fierz-Pauli action, given by (HINTERBICHLER, 2012)

$$S = \int d^D x \left[-\frac{1}{2}\partial_\lambda h_{\mu\nu}\partial^\lambda h^{\mu\nu} + \partial_\mu h_{\nu\lambda}\partial^\nu h^{\mu\lambda} - \partial_\mu h^{\mu\nu}\partial_\nu h + \frac{1}{2}\partial_\lambda h \partial^\lambda h - \frac{1}{2}m^2\left(h_{\mu\nu}h^{\mu\nu} - h^2\right)\right]. \quad (4.1)$$

The non-massive terms are invariant by the following gauge symmetry

$$\delta h_{\mu\nu} = \partial_\mu \xi_\nu + \partial_\nu \xi_\mu, \quad (4.2)$$

however the massive term violates this symmetry. It is worth noting that the -1 that appears in the parentheses of the massive term is called "Fierz-Pauli tuning". Any modification to it will cause this action to no longer describe a single massive spin 2 particle and will change the number of DOFs. Furthermore, it is possible to show that, when $D = 4$, this action leads to the five degrees of freedom as mentioned above (HINTERBICHLER, 2012). Explicit demonstration of these DOFs will be done later in this chapter.

From (4.1) we have the following equations of motion

$$\frac{\delta S}{\delta h^{\mu\nu}} = \Box h_{\mu\nu} - \partial_\lambda \partial_\mu h^\lambda{}_\nu - \partial_\lambda \partial_\nu h^\lambda{}_\mu + \eta_{\mu\nu}\partial_\lambda\partial_\sigma h^{\lambda\sigma} + \partial_\mu\partial_\nu h - \eta_{\mu\nu}\Box h - m^2(h_{\mu\nu} - \eta_{\mu\nu}h) = 0. \quad (4.3)$$

Due to the invariance of the non-massive terms by gauge symmetry (4.2), applying the gradient ∂^μ in the expression (4.3) will result in

$$\partial^\mu h_{\mu\nu} - \partial_\nu h = 0. \quad (4.4)$$

If we then put this result in the expression (4.3) and take the trace, we will get

$$h = 0, \quad (4.5)$$

which due to (4.4) implies that

$$\partial^\mu h_{\mu\nu} = 0. \quad (4.6)$$

Therefore, we have the following result (HINTERBICHLER, 2012)] [(CASTRO, 2018)

$$\left(\Box - m^2\right) h_{\mu\nu} = 0. \tag{4.7}$$

Here we can count the DOFs. It is known that the perturbation $h_{\mu\nu}$ can have up to ten DOFs because it is a symmetrical rank-2 tensor. We have seen that the null trace (4.5) and the transversality of the field (4.6) derive from the equations of motion. The null trace removes one degree of freedom and transversality removes another four. This leaves us with the expected five degrees of freedom.

The equation (4.7) is a Klein-Gordon equation and has a solution of the form

$$h_{\mu\nu} = \epsilon_{\mu\nu}(k) e^{ikx}, \tag{4.8}$$

where k is the wave vector and $\epsilon_{\mu\nu}$ is a symmetrical tensor called the polarization tensor. From (4.8) comes the polarization given by (CASTRO, 2018)

$$\epsilon^{(a)} = \frac{1}{\sqrt{2}} \begin{pmatrix} 0 & 0 & 0 & 0 \\ 0 & 1 & 0 & 0 \\ 0 & 0 & -1 & 0 \\ 0 & 0 & 0 & 0 \end{pmatrix} \quad , \quad \epsilon^{(b)} = \frac{1}{\sqrt{2}} \begin{pmatrix} 0 & 0 & 0 & 0 \\ 0 & 0 & 1 & 0 \\ 0 & 1 & 0 & 0 \\ 0 & 0 & 0 & 0 \end{pmatrix} \tag{4.9}$$

$$\epsilon^{(c)} = -\frac{1}{\sqrt{2}m_g} \begin{pmatrix} 0 & k_3 & 0 & 0 \\ k_3 & 0 & 0 & -\omega \\ 0 & 0 & 0 & 0 \\ 0 & -\omega & 0 & 0 \end{pmatrix} \quad , \quad \epsilon^{(d)} = -\frac{1}{\sqrt{2}m_g} \begin{pmatrix} 0 & 0 & k_3 & 0 \\ 0 & 0 & 0 & 0 \\ k_3 & 0 & 0 & -\omega \\ 0 & 0 & -\omega & 0 \end{pmatrix} \tag{4.10}$$

$$\epsilon^{(e)} = -\frac{1}{\sqrt{2}m_g^2} \begin{pmatrix} k_3^2 & 0 & 0 & -\omega k_3 \\ 0 & -m_g^2/2 & 0 & 0 \\ 0 & 0 & -m_g^2/2 & 0 \\ -\omega k_3 & 0 & 0 & \omega^2 \end{pmatrix} \tag{4.11}$$

where $\epsilon^{(a)}$ and $\epsilon^{(b)}$ represent the "$+$" and "$\times$" polarizations of gravitational waves in GR and the others are some combinations between the three additional fundamental modes that arise in massive gravity. Full demonstration of how to obtain this result can be found in (MORAES, 2019) and (TACHINAMI; TONOSAKI; SENDOUDA, 2021). Figure 10 illustrates the five fundamental modes predicted in massive theories. In (c), (d), (e) and (f) we have the three additional polarizations from massive gravity (since (d) and (e) are expected as one mode) and in (a) and (b) we have the modes predicted by GR.

To demonstrate the vDVZ discontinuity, one could consider the action 4.1 with a source term, given by

$$S = \int d^D x \left[-\frac{1}{2}\partial_\lambda h_{\mu\nu}\partial^\lambda h^{\mu\nu} + \partial_\mu h_{\nu\lambda}\partial^\nu h^{\mu\lambda} - \partial_\mu h^{\mu\nu}\partial_\nu h + \frac{1}{2}\partial_\lambda h \partial^\lambda h - \frac{1}{2}m^2\left(h_{\mu\nu}h^{\mu\nu} - h^2\right) + \kappa h_{\mu\nu}T^{\mu\nu} \right], \tag{4.12}$$

whose equations of motion now take the following form

Figure 10 – Representation of the fundamental polarization modes: In massive gravity, gravitational waves are expected to have five polarization modes, two tensor (also predicted in GR) (a) and (b), two vectors ((c) and (f)) and one scalar (which is a combination of (d) and (e) modes). Unfortunately, it is also expected that in a real emission these modes will combine, i.e., the detected signal must contain a waveform whose behavior is compatible with a mixture of two or more polarization modes, which makes the search for these signals a great challenge. To be able to find these signals, a network of detectors is needed (where five is the minimum number). We currently have only three observatories in observation mode.

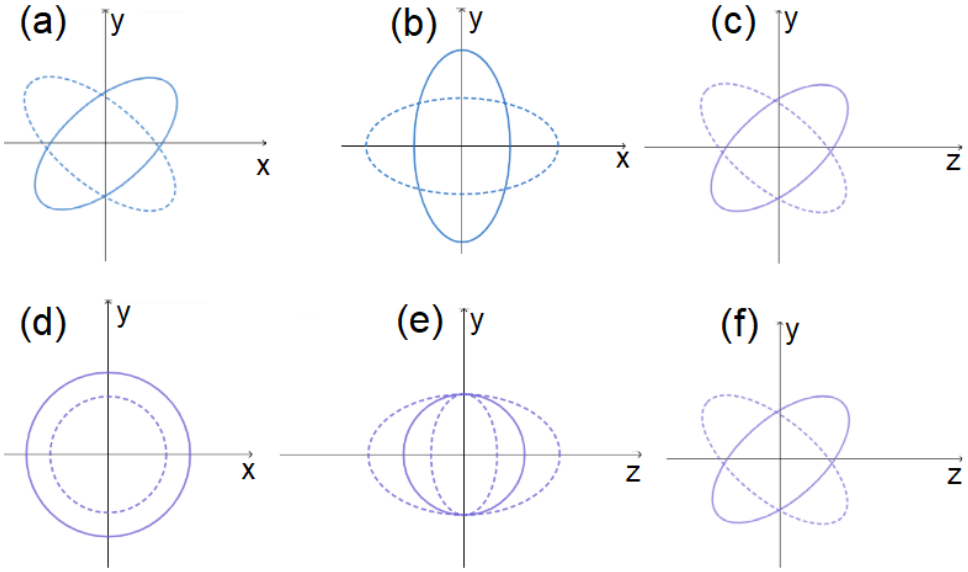

Image source: The author.

$$\Box h_{\mu\nu} - \partial_\lambda \partial_\mu h^\lambda{}_\nu - \partial_\lambda \partial_\nu h^\lambda{}_\mu + \eta_{\mu\nu}\partial_\lambda \partial_\sigma h^{\lambda\sigma} + \partial_\mu \partial_\nu h - \eta_{\mu\nu}\Box h - m^2(h_{\mu\nu} - \eta_{\mu\nu}h) = -\kappa T_{\mu\nu}. \quad (4.13)$$

The solution of the equation (4.13) is (considering $\partial_\mu T^{\mu\nu} = 0$) (HINTERBICHLER, 2012)

$$h_{00}(x) = \frac{2M}{3M_p}\frac{1}{4\pi}\frac{e^{-mr}}{r}, \quad (4.14)$$

$$h_{0i}(x) = 0, \quad (4.15)$$

$$h_{ij}(x) = \frac{M}{3M_p}\frac{1}{4\pi}\frac{e^{-mr}}{r}\left[\frac{1+mr+n^2r^2}{m^2r^2}\delta_{ij} - \frac{1}{m^2r^4}\left(3+3mr+m^2r^2\right)x_i x_j\right], \quad (4.16)$$

where $r \equiv \sqrt{x_i x_i}$, M is the mass of a point particle at rest, $M_p = 1/\kappa$ and e^{-mr} is called the Yukawa factor, very characteristic of massive theories. With that we can build

$$h_{\mu\nu}dx^\mu dx^\nu = -B(r)dt^2 + C(r)dr^2 + A(r)r^r d\Omega^2, \quad (4.17)$$

whose coefficients $A(r)$, $B(r)$ and $C(r)$ are (in the limit where $r \ll 1/m$) (HINTERBICHLER, 2012):

$$A(r) = \frac{M}{3M_p}\frac{1}{4\pi m^2 r^3}, \tag{4.18}$$

$$B(r) = -\frac{2M}{3M_p}\frac{1}{4\pi r}, \tag{4.19}$$

$$C(r) = -\frac{2M}{3M_p}\frac{1}{4\pi m^2 r^3}. \tag{4.20}$$

For comparison, note how these coefficients are in GR:

$$A(r) = \frac{M}{2M_p}\frac{1}{4\pi r}, \tag{4.21}$$

$$B(r) = -\frac{M}{2M_p}\frac{1}{4\pi r}, \tag{4.22}$$

$$C(r) = \frac{M}{2M_p}\frac{1}{4\pi r}. \tag{4.23}$$

It is possible to show that, from the results for the non-massive case, one obtains (HINTERBICHLER, 2012)

$$\phi = -\frac{GM}{r}, \tag{4.24}$$

and

$$\alpha = \frac{4GM}{b}, \tag{4.25}$$

where ϕ is the Newtonian potential and α is the light angular deviation. However, for the massive case, we are left with

$$\phi = -\frac{4GM}{3r}, \tag{4.26}$$

and

$$\alpha = \frac{4GM}{b}. \tag{4.27}$$

We can clearly see that the results for ϕ are not compatible, although the angular deviation of the light remains the same. To make the values of the potentials the same, we can take $G \to 3/4G$. However, this modification will led to $\alpha = (3GM)/b$, confirming the discontinuity problem. We will now see another way to demonstrate this problem, using the Stuckelberg trick.

4.3 THE STUCKELBERG TRICK

A big problem in the previous section is that when we take $m \to 0$ in the equation (4.1) it leads to a non-smooth limit because degrees of freedom are lost when this limit is taken. To avoid this problem (gain or loss of DOFs) we must use the Stuckelberg trick. The idea is to add new fields and gauge symmetries so that the theory is not changed but the limit $m \to 0$ becomes smooth.

Starting from a general massive Lagrangian given by

$$S = \int d^D x \left[\mathcal{L}_{m=0} - \frac{1}{2} m^2 (h_{\mu\nu} h^{\mu\nu} - h^2) + \kappa h_{\mu\nu} T^{\mu\nu} \right] \tag{4.28}$$

we want to conserve the gauge symmetry present in the non-massive part

$$\delta h_{\mu\nu} = \partial_\mu \xi_\nu + \partial_\nu \xi_\mu \tag{4.29}$$

and we will do this by introducing a Stuckelberg field A_μ (vector):

$$h_{\mu\nu} \to h_{\mu\nu} + \partial_\mu A_\nu + \partial_\nu A_\mu. \tag{4.30}$$

Then the action becomes

$$S = \int d^D x \left[\mathcal{L}_{m=0} - \frac{1}{2} m^2 (h_{\mu\nu} h^{\mu\nu} - h^2) - \frac{1}{2} m^2 F_{\mu\nu} F^{\mu\nu} - 2m^2 (h_{\mu\nu} \partial^\mu A^\nu - h \partial_\mu A^\mu) + \right. \tag{4.31}$$

$$\left. + \kappa h_{\mu\nu} T^{\mu\nu} - 2\kappa A_\mu \partial_\nu T^{\mu\nu} \right],$$

where $F_{\mu\nu} \equiv \partial_\mu A_\nu - \partial_\nu A_\mu$. We are then left with an additional gauge symmetry given by $\delta A_\mu = -\xi_\mu$, which is a direct consequence of the transformation of the field $h_{\mu\nu}$. To normalize the kinetic term, we can do $A_\mu \to \frac{1}{m} A_\mu$. Then we can take the limit $m \to 0$. For the four-dimensional case (which is the only one we are going to use in this work), this limit results in four degrees of freedom and therefore the limit is still not smooth since we should have five degrees of freedom.

In order to fix this, we can insert one more Stuckelberg field Φ (scalar) so that

$$A_\mu \to A_\mu + \partial_\mu \Phi. \tag{4.32}$$

Then the action becomes

$$S = \int d^D x \left[\mathcal{L}_{m=0} - \frac{1}{2} m^2 (h_{\mu\nu} h^{\mu\nu} - h^2) - \frac{1}{2} m^2 F_{\mu\nu} F^{\mu\nu} - 2m^2 (h_{\mu\nu} \partial^\mu A^\nu - h \partial_\mu A^\mu) - \right. \tag{4.33}$$

$$\left. - 2m^2 (h_{\mu\nu} \partial^\mu \partial^\nu \Phi - h \partial^2 \Phi) + \kappa h_{\mu\nu} T^{\mu\nu} - 2\kappa A_\mu \partial_\nu T^{\mu\nu} + 2\kappa \Phi \partial_\mu \partial_\nu T^{\mu\nu} \right].$$

The new gauge symmetries are: $\delta A_\mu = \partial_\mu \Lambda$ e $\partial^2 \Phi = \Lambda$. If we once again make $A_\mu \to \frac{1}{m} A_\mu$ and

$\Phi \to \frac{1}{m^2}\Phi$ we will get

$$S = \int d^D x \Big[\mathcal{L}_{m=0} - \frac{1}{2}m^2(h_{\mu\nu}h^{\mu\nu} - h^2) - \frac{1}{2}F_{\mu\nu}F^{\mu\nu} - 2m(h_{\mu\nu}\partial^\mu A^\nu - h\partial_\mu A^\mu) \tag{4.34}$$

$$-2(h_{\mu\nu}\partial^\mu\partial^\nu\Phi - h\Box\Phi) + kh_{\mu\nu}T^{\mu\nu} - \frac{2}{m}kA_\mu\partial_\nu T^{\mu\nu} + \frac{2}{m^2}k\Phi\partial_\mu\partial_\nu T^{\mu\nu}\Big].$$

If we now take the limit $m \to 0$, the previous action will become

$$S = \int d^D x \Big[\mathcal{L}_{m=0} - \frac{1}{2}F_{\mu\nu}F^{\mu\nu} - 2(h_{\mu\nu}\partial^\mu\partial^\nu\Phi - h\Box\Phi) + \kappa h_{\mu\nu}T^{\mu\nu}\Big] \tag{4.35}$$

and we can show that this action now carries the expected five degrees of freedom.

With the action (4.34) we can follow the same procedures as in the chapter 3 to find the equations of motion and, when solving them, we must find the same polarizations mentioned in the previous section. But our final goal here is to verify how the Stuckelberg fields helps us to highlight the vDVZ discontinuity that actually appears in the Lagrangian, not just in the equations of motion that come out of it. The purpose is to demonstrate that the discontinuity is more evident when taking the zero mass limit directly in the Lagrangian rather than in the equations of motion. To do so, we need to follow some important steps. But before that, we will explicitly count the DOFs in the massive theory, and with this we will see some of the steps that will be used in the next section.

4.4 COUNTING DEGREES OF FREEDOM

We will start our study with a massive action already with the Stuckelberg fields, given by

$$S = \int d^4 x \Big[\mathcal{L}_{m=0} - \frac{1}{2}m^2(h_{\mu\nu}h^{\mu\nu} - h^2) - \frac{1}{2}F_{\mu\nu}F^{\mu\nu} - 2m(h_{\mu\nu}\partial^\mu A^\nu - h\partial_\mu A^\mu) \tag{4.36}$$

$$-2(h_{\mu\nu}\partial^\mu\partial^\nu\Phi - h\Box\Phi) + kh_{\mu\nu}T^{\mu\nu} - \frac{2}{m}kA_\mu\partial_\nu T^{\mu\nu} + \frac{2}{m^2}k\Phi\partial\partial T\Big],$$

where $F_{\mu\nu} \equiv \partial_\mu A_\nu - \partial_\nu A_\mu$ and $\partial\partial T = \partial_\mu\partial_\nu T^{\mu\nu}$. From the expression above derive the following equations of motion (see appendix B):

$$\text{General Relativity} + m^2\left(h^{\varepsilon\rho} - \eta^{\varepsilon\rho}h\right) + 2m\left[\frac{1}{2}\left(\partial^\varepsilon A^\rho + \partial^\rho A^\varepsilon\right) - \partial_\mu A^\mu\eta^{\varepsilon\rho}\right] \tag{4.37}$$

$$+2\left(\partial^\varepsilon\partial^\rho\Phi - \eta^{\varepsilon\rho}\Box\Phi\right) - kT^{\varepsilon\rho} = 0,$$

$$\Box A^\rho - \partial_\varepsilon\partial^\rho A^\varepsilon + m\left(\partial_\varepsilon h^{\varepsilon\rho} - \partial^\rho h\right) - \frac{2}{m}k\partial_\nu T^{\rho\nu} = 0, \tag{4.38}$$

$$\Box h - \partial^\mu \partial^\nu h_{\mu\nu} - \frac{2}{m} k \partial\partial T = 0, \tag{4.39}$$

where "General Relativity" in 4.37 corresponds to the equations of motions that comes from the Einstein-Hilbert action.

In order to determine the degrees of freedom present in these equations, we can first write them in terms of gauge invariants, as we did for GR (see chapter 3). To do this, we start with the decomposition of the field A_μ :

$$A_0 = 2\omega, \tag{4.40}$$

$$A_i = J_i + \partial_i M. \tag{4.41}$$

Taking the following gauge symmetries

$$\delta A_\mu = -\xi_\mu, \tag{4.42}$$

$$\delta A_\mu = \partial_\mu \Lambda \tag{4.43}$$

we can search for the equations that come out of the field A_μ using the same procedure as for the field $h_{\mu\nu}$ (see chapter 3). Then, using (4.42) we have (see appendix C)

$$\tilde{A}_0 = 2\omega - \xi_0 = 2\tilde{w}, \tag{4.44}$$

$$\tilde{A}_i = J_i + \partial_i M - \xi_i = \tilde{J}_i + \partial_i \tilde{M}. \tag{4.45}$$

And using (4.43), we have (see appendix C)

$$\tilde{\tilde{A}}_0 = 2\omega + \partial_0 \Lambda = 2\tilde{\tilde{\omega}}, \tag{4.46}$$

$$\tilde{\tilde{A}}_i = J_i + \partial_i M + \partial_i \Lambda = \tilde{\tilde{J}} + \partial_i \tilde{\tilde{M}}. \tag{4.47}$$

where the letters with $\tilde{}$ and $\tilde{\tilde{}}$ represent the transformed fields. As a result, we have the following invariants:

$$\tilde{J}_i = J_i - \xi_i^D, \tag{4.48}$$

$$\tilde{\tilde{J}}_i = J_i, \tag{4.49}$$

$$\tilde{M} = M - \xi^R, \tag{4.50}$$

$$\tilde{\tilde{M}} = M + \Lambda, \tag{4.51}$$

$$\tilde{\omega} = \omega - \frac{1}{2}\,\xi_0, \tag{4.52}$$

$$\tilde{\tilde{\omega}} = \omega + \frac{1}{2}\partial_0\Lambda. \tag{4.53}$$

We can then combine the previous equations in order to find new gauge invariants (see appendix C), as we did in chapter 3. Then, combining $\tilde{\tilde{M}}$ and $\tilde{\tilde{\omega}}$, we get

$$\tilde{f}_1 = f_1 = \frac{1}{2}\partial_0 M - \omega.$$

If we now combine $\tilde{\phi}$, $\tilde{S}$ and $\tilde{M}$, we are left with

$$\tilde{f}_2 = f_2 = \phi - \partial_0 S - \partial_0^2 M. \tag{4.54}$$

It is also possible to combine $\tilde{\omega}$, $\tilde{S}$ and $\tilde{E}$:

$$\tilde{f}_3 = f_3 = \omega + \frac{1}{2}S - \frac{1}{2}\partial_0 E. \tag{4.55}$$

or even $\tilde{\omega}$, $\tilde{S}$ and $\tilde{M}$, so we get

$$\tilde{f}_4 = f_4 = 2\omega + \partial_0 M + S. \tag{4.56}$$

Finally, we can combine $\tilde{F}$, $\tilde{J}$ e $\tilde{B}$:

$$\tilde{f}_5 = f_5 = 2\partial_0 J_i + \partial_0 F_i + B_i \tag{4.57}$$

Now that we have all the necessary gauge invariants, we can rewrite the three equations of motion (4.37), (4.38) and (4.39) in terms of them. Starting with the third equation of motion and remembering that it is given by (without source)

$$\Box h - \partial^\epsilon \partial^\rho h_{\epsilon\rho} = 0 \tag{4.58}$$

and decomposing the field $h_{\mu\nu}$, we get (see appendix C)

$$\nabla^2 (D - 2\Psi) + 3\,\partial_0^2 \Psi = 0. \tag{4.59}$$

With the second equation of motion (4.38), after lowering the indices, we are left with

$$\Box A_\alpha - \partial^\beta \partial_\alpha A_\beta + m(\partial^\beta h_{\beta\alpha} - \partial_\alpha h) = 0. \tag{4.60}$$

Then, varying β , we have

$$\Box A_\alpha - \partial^0\partial_\alpha A_0 - \partial^i\partial_\alpha A_i + m(\partial^0 h_{0\alpha} + \partial^i h_{i\alpha} - \partial_\alpha h) = 0 \tag{4.61}$$

and when $\alpha = 0$ we are left with

$$\Box A_0 - \partial^0\partial_0 A_0 - \partial^i\partial_0 A_i + m(\partial^0 h_{00} + \partial^i h_{i0} - \partial_0 h) = 0. \tag{4.62}$$

Substituting the decomposition (4.40) and (4.41) into (4.62), we have

$$\Box 2\omega - \partial^0\partial_0 2\omega - \partial^i\partial_0(J^i + \partial_i M) + m\left[\partial^0 2\phi - \partial^i(B_i + \partial_i S) - \partial_0(-2\phi + 6\Psi + 2\nabla^2 E)\right] = 0 \tag{4.63}$$

If we now take $m = 0$ we will get

$$\nabla^2\left(f_1\right) = 0, \tag{4.64}$$

where

$$f_1 = \left(\frac{1}{2}\partial_0 M - \omega\right). \tag{4.65}$$

When $\alpha = j$ we are left with

$$\Box A_j - \partial^0\partial_j A_0 - \partial^i\partial_j A_i + m(\partial^0 h_{0j} + \partial^i h_{ij} - \partial_j h) = 0. \tag{4.66}$$

Taking the same substitution as before, we are left with

$$\partial_0\partial^0 J_j - \partial_j\partial_0^2 M - 2\partial_0\partial_j\omega + m\Bigg(\partial^0 B_j + \partial^0\partial_j S + 2\delta_{ij}\partial^i\Psi + \tag{4.67}$$

$$+\partial^i\partial_i F_j + 2\partial_j\phi - 6\partial_j\Psi\Bigg) = 0$$

and if once again we take $m = 0$, we will have

$$-2\partial_0\partial_j f_1 + \partial_0\partial^0 J_j = 0. \tag{4.68}$$

Finally, following exactly the same procedures as before for the first equation of motion (4.37), already taking the zero mass limit and lowering the indices, we are left with :

- For the component 00:

$$\nabla^2 D + 3\partial_0\partial_0\Psi + 2\left(\partial_0\partial_0\Phi - \eta_{00}\Box\Phi\right) = 0. \tag{4.69}$$

- For the component $0i$:

$$\nabla^2 H_i + 4\partial_0\partial_i\Psi + 2\left(\partial_0\partial_i\Phi - \eta_{0i}\Box\Phi\right) = 0. \tag{4.70}$$

- For the component ij:

$$\partial_0\partial_i H_j - 2\partial_i\partial_j D + 2\left(\Box\delta_{ij} + \partial_i\partial_j\right)\Psi + \Box h_{ij}^{TT} + 2\left(\partial_i\partial_j\Phi - \eta_{ij}\Box\Phi\right) = 0. \tag{4.71}$$

We can combine the equations (4.59), (4.64), (4.68), (4.69), (4.70), (4.71), taking the trace or divergence of some of them, for example, and with the final result we can count the degrees of freedom of the theory. However, we want this information to be as explicit as possible in our equations of motion and this is not as evident in our equations as it was in the case of GR. So, instead, it is more convenient to go back to the equations (4.37), (4.38) and (4.39) and introduce a change of variable of the form

$$h_{\mu\nu} = h'_{\mu\nu} + \pi\eta_{\mu\nu}. \tag{4.72}$$

Then the equation (4.37) will be given by

$$\Box h^{\mu\nu} - \partial_\alpha\partial^\mu h^{\nu\alpha} - \partial_\alpha\partial^\nu h^{\mu\alpha} + \partial^\mu\partial^\nu h - \eta^{\mu\nu}\left(\Box h - \partial\alpha\partial_\beta h^{\alpha\beta}\right) + 2\left(\partial^\mu\partial^\nu\Phi - \eta^{\mu\nu}\Box\Phi\right) = 0, \tag{4.73}$$

where

$$\Box h^{\mu\nu} - \partial_\alpha\partial^\mu h^{\nu\alpha} - \partial_\alpha\partial^\nu h^{\mu\alpha} + \partial^\mu\partial^\nu h - \eta^{\mu\nu}\left(\Box h - \partial\alpha\partial_\beta h^{\alpha\beta}\right) = \text{General Relativity} \tag{4.74}$$

and it becomes (see appendix C)

$$\Box h'^{\mu\nu} - \partial_\alpha\partial^\mu h'^{\nu\alpha} - \partial_\alpha\partial^\nu h'^{\mu\alpha} + \partial^\mu\partial^\nu h' - \eta^{\mu\nu}\Box h' + \eta^{\mu\nu}\partial_\alpha\partial_\beta h'^{\alpha\beta} = 0, \tag{4.75}$$

which is exactly the result we would have with GR but in the new coordinate system. Then we already know the equations that comes from (4.75), which are (3.27), (3.29) and (3.31) (see chapter (3)). If we then take $\xi^R = -E$, $\xi^0 = -S + \partial_0 E$ and $\xi_i^D = -F_i$, we will find in the first important result:

$$\Box h_{ij}'^{TT} = 0. \tag{4.76}$$

Then, applying the same transformation (4.72) in the equation (4.39) we get

$$\Box\left(h' + 4\pi\right) - \partial^\mu\partial^\nu\left(h'_{\mu\nu} + \pi\eta_{\mu\nu}\right) = 0, \tag{4.77}$$

which leads to (see appendix C)

$$\Box\Phi = 0. \tag{4.78}$$

Finally, from the equation (4.38), which no longer depends on the field $h_{\mu\nu}$ after taking the zero mass limit, we will have

$$\nabla^2 f_1 = 0 \tag{4.79}$$

with which we have that $f_1 = 0$. Subsequently, we have

$$\Box J_j = 0. \tag{4.80}$$

With this we can explicitly see that from (4.76) we have two DOFS, from (4.78) we have one more and, finally, from (4.80) we have two more DOFs, totalizing the five degrees of freedom expected for massive gravity theory.

4.5 ANOTHER APPROACH FOR THE VDVZ DISCONTINUITY

In the section (4.2) we started our study of massive gravity by verifying how the equations of motion, the gravitational potential and the deflection of light, are in the Fierz-Pauli theory. As this is a well-known result; there was no need to develop the equations involved. After that, we explicitly count how many DOFs exists in that theory. To do it, we used the Stuckelberg trick, found the equations of motion (without source) and wrote them by two different methods: from the decomposition of the fields and from a change of variables. We saw that with the second method the DOFs were more explicit, as we wanted. However, there is a question we can ask about the procedures used so far. In the section 4.2 , we saw that the vDVZ discontinuity leads to a change in the value of the gravitational potential. This conclusion is reached simply by taking the zero-mass limit in the equations of motion coming out of (4.1). However, despite being a correct procedure, it does not help us to see the origin of this discontinuity, only its consequence. For that, we need to go back to the action (B.1), apply the change of variable (4.72), but now, we will keep the source term until the end. If we then take the zero-mass limit, we have

$$S = \int d^4x \Big\{ -\frac{1}{2}\partial_\lambda h'_{\mu\nu}\partial^\lambda h'^{\mu\nu} + \partial_\mu h'_{\nu\lambda}\partial^\nu h'^{\mu\lambda} - \partial_\mu h'^{\mu\nu}\partial_\nu h' + \frac{1}{2}\partial_\lambda h'\partial^\lambda h' - \tag{4.81}$$

$$-\frac{1}{2}F_{\mu\nu}F^{\mu\nu} - 3\partial_\mu\Phi\partial^\mu\Phi + \kappa h'_{\mu\nu}T^{\mu\nu} + \kappa\Phi T\Big\}.$$

Here it is clear how the Stuckelberg field (scalar) does not decouple from the energy-momentum tensor at the limit where $m \to 0$. This is the origin of the vDVZ discontinuity, which we can now fully demonstrate.

Starting from (4.81), we will repeat the procedures done in the appendix A to obtain, once again, the equations of motion. So, we will be left with the following expressions (see appendix A and D)

- For A_μ:

$$\Box A^\rho - \partial_\epsilon\partial^\rho A^\epsilon = 0 \tag{4.82}$$

which as a function of the gauge invariants is

$$\Box J_j = 0. \tag{4.83}$$

- For $h_{\mu\nu}$:

In (4.81) the terms that depend on $h_{\mu\nu}$ are exactly those existing in the Einstein-Hilbert action with source, so, when varying this action with respect to $h_{\mu\nu}$ we will simply obtain the result already known in GR (see chapter 3), which is

$$\Box h_{ij}^{TT} = 0. \tag{4.84}$$

- For Φ:

Finally, when varying (4.81) with respect to the field Φ, we have:

$$-6\Box\Phi - \kappa T = 0, \tag{4.85}$$

where Φ is already a gauge invariant. Now, we just have to solve (4.85) to show the consequence that the vDVZ discontinuity has on the gravitational potential. For this, we need to use the Fourier transform and also define an energy-momentum tensor. Let us therefore consider a point source so that

$$T_{\mu\nu} = M\delta^{\{3\}}(\vec{x})\delta^0_\mu\delta^0_\nu. \tag{4.86}$$

Since

$$\Phi(\vec{x},t) = \frac{1}{(2\pi)^{3/2}}\int d^3\vec{k}\Big\{\ \tilde{\Phi}(\vec{k},t)\ \ e^{-i\vec{k}\cdot\vec{x}}\Big\} \tag{4.87}$$

and

$$\delta^{\{3\}}(\vec{x}) = \frac{1}{(2\pi)^{3/2}}\int d^3k\ \ \left\{\frac{e^{-i\vec{k}\cdot\vec{x}}}{(2\pi)^{3/2}}\right\} \tag{4.88}$$

then,

$$\Box\Phi = \frac{1}{(2\pi)^{3/2}}\int d^3k\ \ \left\{\Box\left(\tilde{\Phi}(\vec{k},t)\ \ e^{-i\vec{k}\cdot\vec{x}}\right)\right\} = \tag{4.89}$$

$$= \frac{1}{(2\pi)^{3/2}}\int d^3k\ \ \left\{-e^{-i\vec{k}\cdot\vec{x}}\ddot{\tilde{\Phi}}(\vec{k},t) - \vec{k}^2\tilde{\Phi}(\vec{k},t)e^{-i\vec{k}\cdot\vec{x}}\right\}, \tag{4.90}$$

and then (4.85) is:

$$\frac{1}{(2\pi)^{3/2}}\int d^3k\ \ \left\{e^{-i\vec{k}\cdot\vec{x}}\ 6\left(\ddot{\tilde{\Phi}}(\vec{k},t) + \vec{k}^2\tilde{\Phi}(\vec{k},t)\right)\right\} = \frac{M\kappa}{(2\pi)^{3/2}}\int d^3k\left\{\frac{e^{-i\vec{k}\cdot\vec{x}}}{(2\pi)^{3/2}}\right\} \tag{4.91}$$

$$\frac{1}{(2\pi)^{3/2}}\int d^3k\left\{e^{-i\vec{k}\cdot\vec{x}}\left[6(\ddot{\tilde{\Phi}} + \vec{k}^2\tilde{\Phi}) - \frac{M\kappa}{(2\pi)^{3/2}}\right]\right\} = 0. \tag{4.92}$$

Inside the integral (4.92) we have the differential equation

$$\ddot{\tilde{\Phi}} + \vec{k}^2\tilde{\Phi} = \frac{M\kappa}{6(2\pi)^{3/2}} \tag{4.93}$$

which solution is of the form

$$\tilde{\Phi}(\vec{k},t) = \text{Homogeneous solution} + \text{Particular solution.} \tag{4.94}$$

The homogeneous solution has the form

$$\text{Homogeneous solution} = C_1 e^{ikt} + C_2 e^{-ikt}, \tag{4.95}$$

where $k = \sqrt{\vec{k}^2}$. On the other hand, the particular solution is

$$\text{Particular solution} = \frac{M\kappa}{6(2\pi)^{3/2}\vec{k}^2}. \tag{4.96}$$

Therefore, substituting (4.95) and (4.96) in (4.92), we get

$$\Phi(\vec{x},t) = \frac{1}{(2\pi)^{3/2}}\int d^3k\left\{e^{-i\vec{k}\cdot\vec{x}}\left[C_1 e^{ikt} + C_2 e^{-ikt} + \frac{M\kappa}{6(2\pi)^{3/2}\vec{k}^2}\right]\right\} \tag{4.97}$$

$$= \frac{1}{(2\pi)^{3/2}}\int d^3k\left\{e^{-i\vec{k}\cdot\vec{x}}\left(C_1 e^{ikt} + C_2 e^{-ikt}\right)\right\} + \frac{M\kappa}{6(2\pi)^{3/2}}\int d^3k\ \left\{\frac{e^{-i\vec{k}\cdot\vec{x}}}{\vec{k}^2}\right\}. \tag{4.98}$$

Since the first integral is not coupled to the source, we only need to solve for the second integral. Taking $\vec{x}$ in the direction of k_z we have (in spherical coordinates)

$$\Phi_{\text{particular}} = \frac{M\kappa}{6(2\pi)^{3/2}}\int d^3k\ \left\{\frac{e^{-ikr\cos\theta}}{k^2}\right\} \tag{4.99}$$

$$= \frac{4\pi}{r}\int_0^\infty dk\frac{sen(kr)}{k} = \frac{4\kappa^2}{2r}. \tag{4.100}$$

Therefore (4.96) is:

$$\Phi_{\text{particular}} = \frac{M\kappa}{6(2\pi)^{3/2}}\frac{4h^2}{2r}. \tag{4.101}$$

Taking $\kappa = 32\pi G$ we finally have

$$\Phi_{\text{particular}} = \frac{4GM}{3r}. \tag{4.102}$$

This is exactly the result demonstrated at the beginning of this chapter but, with this method, it was possible not olny to demonstrate the gravitational potential in the Fierz-Pauli theory, but also highlight the origin of the vDVZ discontinuity.

In the next chapter we will see some details about the detection and analysis of gravitational wave signals. For that we only use GR. As we have seen, a network of detectors (with at least five) is

necessary to start our search for astrophysical signals with the characteristics predicted by massive gravity and, so far, we have only three ground-based observatories in operation. Therefore, this work aimed to investigate the behavior of these waves in a theory beyond general relativity with a purely theoretical approach.

5 SIGNAL ANALYSIS.

Now that we know how gravitational waves are described in GR, in massive gravity and we understand the importance of testing these (and others) theories and how it is done, we can study in more detail about the signal analysis process and we will do that with simulations. Therefore, in this chapter we will begin the analysis of simple simulated signals of gravitational waves. We will start in the section 5.1 with a review about gravitational wave detectors. In section (5.2.1) we will study some fundamental concepts such as Fourier transforms, sampling and aliasing. Then, in 5.2.2, we will see the main window functions and the importance of using them in signal analysis. Finally, in 5.2.3, we will briefly discuss some filtering methods and in 5.3 we will discuss the post-Newtonian approximation method in a little more detail. With these concepts we will be able to understand the procedures, challenges and results of the analysis of the inspiral stage (long before merger) of three simulated signals: Hulse-Taylor binary: PSR 1913+16 (5.4.1), GW190426-152155 (5.4.2) and GW170817 (5.4.3).

5.1 INTERFEROMETRIC OBSERVATORIES

We will start by studying how the interferometric observatories operates. These observatories were developed based on the Michelson interferometer. Figure 11 illustrates the most fundamental aspects of this experiment.

Figure 11 – Representation of Michelson interferometer.

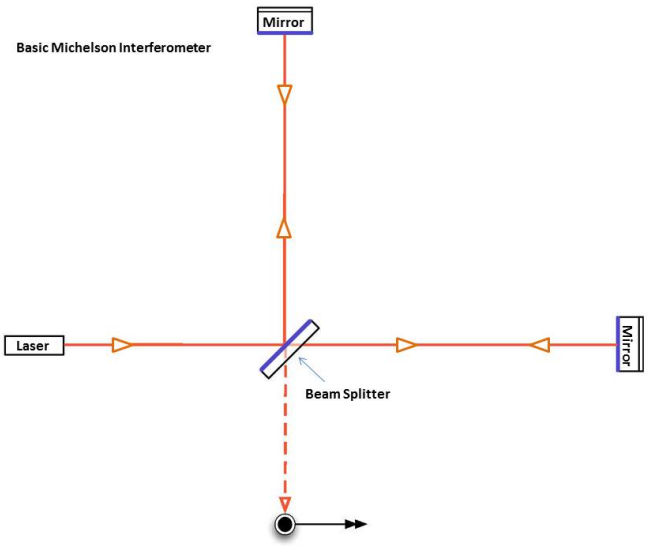

Image source: (LIGO-CALTECH, 2015).

The interferometer is made up of two long perpendicular arms, through which a light beam that is generated by a laser and divided by a beam-splitter. In addition, there are two highly reflective mirrors, which are located at the end of each arm, forcing the light beams to travel all the way back and recombine at the photon detector. In an ideal situation, i.e., if the experiment is not affected by

any external forces, when the two beams recombine they will suffer destructive interference and no signal will appear in the photon detector. However, when a gravitational wave passes through the interferometer, it will force the arms to be stretched and contracted and, consequently, this will change the arrival time of the light beams. That way, when they recombine, the interference will no longer be completely destructive and an interference pattern will appear in the detector.

Evidently, LIGO observatories (among others) are much more complex than we see in this illustration and the main reason is the need for the experiment to have the necessary sensitivity to detect the effect of the passage of a gravitational wave which amplitude, as we have already seen, is very tiny. Thus, to get a more accurate illustration of the structure of these observatories we need to take into account the modifications and improvements that must be made to the Michelson experiment.

The first thing to consider is the size of the experiment arms. The longer they are, the longer the path the light beams will have to travel and, consequently, any action of external forces will affect the experiment more significantly, i.e., the experiment will become more sensitive to small variations in the path of the light beams. The LIGO observatories has 4km-long arms while Virgo has arms 3km-long. Unfortunately, these lengths are still not enough to detect gravitational waves and there is a geographic limitation that prevents the construction of much larger observatories. To solve this problem, a new set of mirrors is added between the beam-splitter and the reflecting mirrors of each arms, creating two new regions called Fabry-Pérot cavities.

Figure 12 – Representation of the structure of interefometric observatories: Fabry-Pérot cavities.

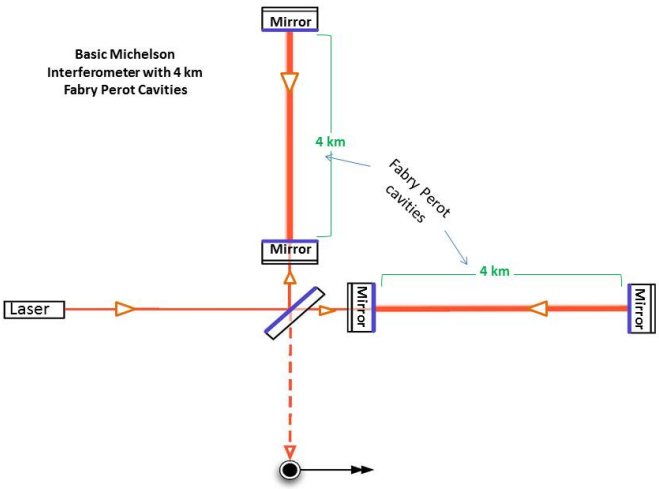

Image source: (LIGO-CALTECH, 2015)

These new mirrors are partially reflective, so part of the light is forced back towards the mirrors located at the end of the detector's arms, where it will be reflected back once again. This phenomenon keeps happening, forcing the light to travel a much longer path than the actual size of the arms. These cavities, illustrated in Figure 12, are responsible for a large increase in the sensitivity of observatories. Any change in these regions will result in very significant changes in the pattern generated in the detector.

Figure 13 – Representation of the structure of interferometric observatories: Power recycling mirrors.

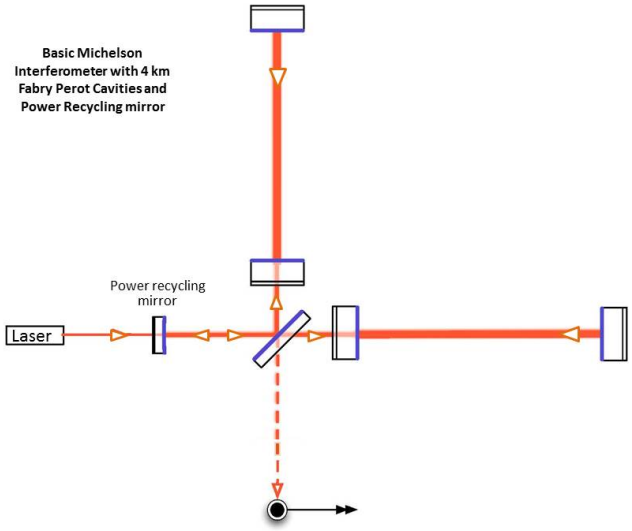

Image source: (LIGO-CALTECH, 2015).

Another important thing is the power of the laser. For the experiment to have the necessary sensitivity, the laser needs to have a power of at least 700 kW, however, the LIGO's laser only reaches 200 kW (LIGO-Caltech). In order to fix this problem, we need to insert one more set of mirrors, called power recycling mirrors. This time, this modification is inserted between the laser and the beam-splitter. The Figure 13 illustrates how the light coming from the laser is accumulated and gains more power before passing through the beam-splitter.

Lastly, we can also force back the light that arrives at the detector into the experiment arms. This procedure is called signal recycling and it also helps to increase the detector's sensitivity to certain frequency ranges, helping to deal especially with instrumental noise.

It is worth mentioning that there are still many other modifications and the real observatories are much more complex. However, for the purposes of this work, these informations are sufficient to continue.

Then we can study another important experimental aspect, which is noise. Just like any other experiment, interferometric observatories suffer from a number of external factors that make it difficult or even prevent the detection of a gravitational wave. Some of the noise comes from the experimental equipment itself, while others come from the environment. As the main sources of noise, we can cite: shot noise, radiation pressure, seismic noise, thermal and gravity gradient noise. (CREIGHTON; ANDERSON, 2011).

The shot noise is a random noise of instrumental origin that predominates at high frequencies. To reduce its effects, it is needed to increase the power of the laser. However, by doing this we increase the radiation pressure noise. This other noise predominates at low frequencies and originates in the small movement of the mirrors caused by "pushes of radiation". In order to reduce this movement, heavier mirrors are used. Unfortunately, it is not possible to eliminate either of the two noises and if we try to decrease the effect of one of them, we will automatically have to deal with the increase of the other.

Another problem of instrumental origin is thermal noise. It will predominate at frequencies above 40 Hz and its cause is the random movement of molecules on the surface of the mirrors and in the wires that suspend the equipment. One way to deal with these effects is by performing a very rigorous cleaning and maintenance of the mirrors.

Finally, the noises of environmental origin are the seismic noise and the gravity gradient noise. There are several phenomena that can influence the interferometer measurements. The most evident of these is the occurrence of earthquakes. However, people passing on the street, cars, wind and even ocean waves can generate relatively loud noises in the detector. To deal with these issues, interferometers are designed so that the mirrors are suspended. Furthermore, fluctuations in the density of the soil or atmosphere affect mirrors simply by their Newtonian forces. This gravity gradient noise acts at low frequencies along with radiation pressure noise, although it is almost imperceptible in the current detectors. It is likely that for the next generation of detectors, with increasing sensitivity, this noise will become a bigger problem. With this in mind (among other challenges), one possibility to deal with these issues would be the construction of underground interferometers (as already is the case of KAGRA observatory).

5.2 INTRODUCTION TO SIGNAL PROCESSING

All the analysis that will be demonstrated in this section was done with Python language from the Jupyter platform. Numpy, Scipy and Matplotlib libraries were used, which complete documentation can be found in (BURNS; AL, 2020). But before we go directly to the analysis, it is important to understand all the operations that will be performed in the process.

5.2.1 Fourier transform

The first (and probably the most important) concept we need an overview is the Fourier Transform (FT). We use the FT to take a signal from the time domain to the frequency domain (and vice versa). This procedure is very useful because the signal is often obscured by noise that is more easily identifiable in the frequency domain, where we can analyze what is noise and what is a signal with the power spectral density.

A continuous signal $f(t)$ will have an FT $F(\nu)$ given by

$$F(\nu) = \int_{\infty}^{\infty} f(t) e^{-2\pi i \nu t} dt \tag{5.1}$$

which inverse transform is

$$f(t) = \int_{-\infty}^{\infty} F(\nu) e^{2\pi i \nu t} d\nu. \tag{5.2}$$

In general we are interested in signals that are finite in time and therefore it is more interesting to transport the signal from its continuous form to a discrete form. To do this, we just build the signal $f(t)$ from N points evenly spaced in an interval $t \in [0, T]$, where T is the total time of the signal(JOHANSSO, 2019). The result is a set of samples $(x_0, x_1, ..., x_N)$, as illustrated in Figure 14.

The upper figure represents the continuous signal in the time domain (x-axis refers to time and y-axis refers to amplitude) and the figure represents the discrete signal (dots) with only a background shadow indicating the original behavior of the signal.

Figure 14 – Representation of a sinusoidal signal in the time domain: continuous signal (a) and discrete signal (b).

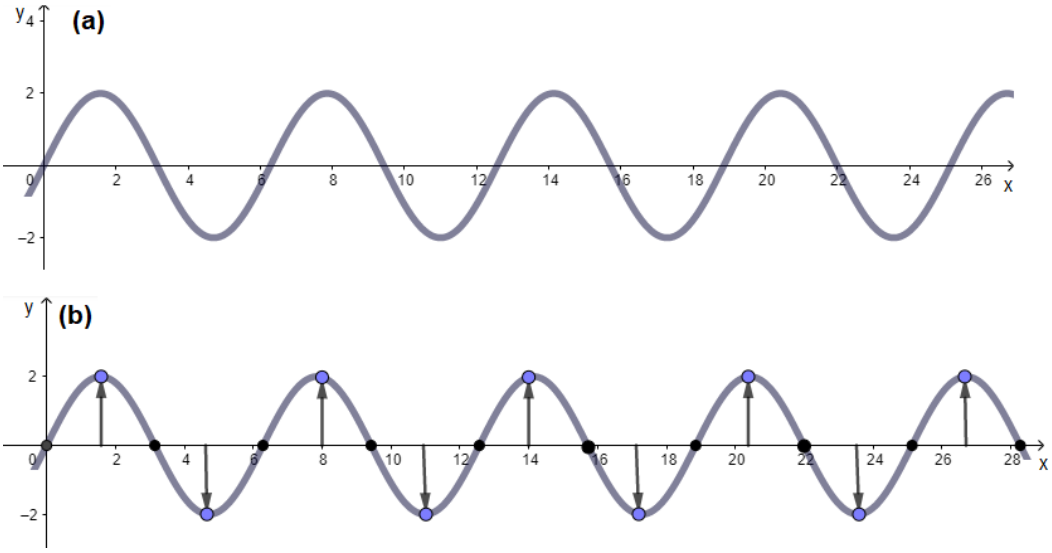

Image source: The author.

Then, the discrete Fourier transform (DFT) will be given by

$$X_k = \sum_{n=0}^{N-1} x_n e^{-2\pi i n k/N} \tag{5.3}$$

and its inverse will be

$$x_n = \frac{1}{N} \sum_{k=0^{N-1}} X_k e^{2\pi i n k/n}, \tag{5.4}$$

where X_k is the FT of each sample x_n and k represents the transformed points that can be associated with real frequencies.

In Python we are going to use the rfft, irfft and rfftfreq functions of the SciPy module fftpack. This module offers the implementation of the FFT (Fast Fourier Transform) algorithm, which allows us to calculate the DFT and its inverse efficiently and quickly. As in our case we will be dealing with data that depend only on values in the real domain ($\Re$), i.e., there are no complex values, we can use the rfft functions for the Fourier transform (instead of the fft which includes complex values) and irrft for the inverse (instead of ifft). To calculate the frequencies associated with the values of the points returned by the FFT, we just have to use the rfftfreq function.

This process of rewriting a continuous signal into a discrete form is called sampling and there are some important considerations to make about this procedure.

5.2.1.1 Sampling Theorem

Initially consider another continuous sinusoidal signal such as Figure 14 (a). To transform it into a discrete signal, we just choose some points within a certain range t. To do the inverse, we just need to interpolate and then the signal will return to a continuous form. However, if the number of points chosen initially is very small, after interpolation the signal may assume a very different shape from the original.

Figure 15 – Representation of a continuous sinusoidal signal in the time domain after interpolation.

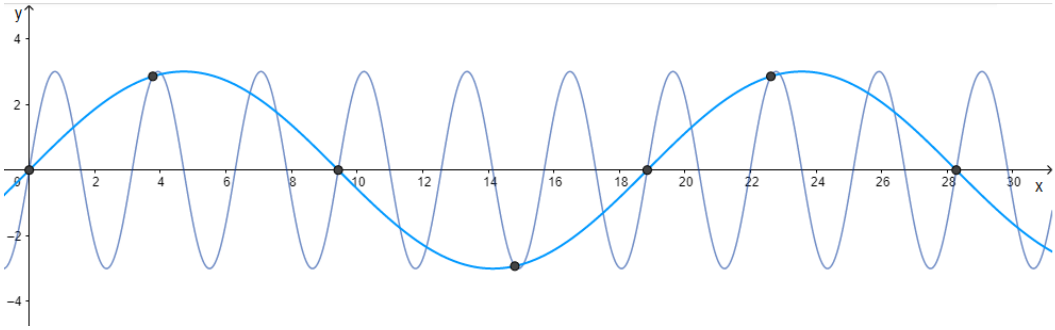

Image source: The author.

Figure 15 shows a random choice of some points and the blue light curve shows how the signal after the interpolation has a much lower frequency than the initial signal. This means that, if we initially have a signal with several frequencies (such as an audio signal), the lack of points in the interpolation can generate a loss of information and will lead to distortion of some higher frequencies. This phenomenon is called aliasing. To avoid it, we must choose at least two points per cycle of the signal. The Nyquist sampling theorem says that the sampling frequency must be greater than or equal to twice the value of the maximum frequency (Nyquist frequency) that one wants to represent without distortion by aliasing, that is,

$$f_s \geq 2f_{NQ}. \tag{5.5}$$

This procedure, as we mentioned, also works for the number of points that must be chosen as at least twice the number of points in the sample. This is interesting because we do not always know what are the highest frequency existing in the original signal, especially if it is covered by noise. We will see in these analysis of simulated signals that this second procedure will be the most appropriate in order to guarantee that the entire gravitational signal will not be distorted.

5.2.2 Windowing

One of the most common processes in data analysis is called Windowing. This process consists of a simple convolution between a window function and the signal to be analyzed.

Convolution is a mathematical operation between two functions, f and g, that results in a third function which behavior tells us how the shape of f is modified by g. This operation is of the form $f * g$ and is illustrated in Figure 16. This process is mainly used when we want to highlight or ignore some part of a given signal.

Figure 16 – Convolution between two functions f e g: Widely used in signal filtering, convolution helps to highlight parts of a signal, which can be very useful when the signal involves noise.

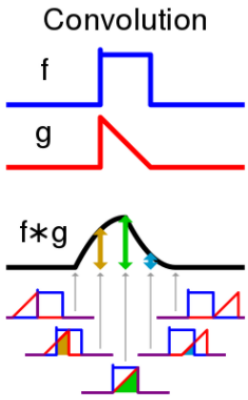

Image source: (WIKIPEDIA, 2021a).

A window function is the one which values are always null if they are outside a certain chosen range(JOHANSSO, 2019). This function causes the central values of this range to be maintained (or accentuated) while the initial and final values are attenuated, tending to zero. Some of the most famous window functions are: Blackman, Kaiser, Hamming and Tukey. Figure 17 and Figure 18 illustrate some of them. In the vast majority of cases, these windows mentioned above are interchangeable, i.e., any one of them can be used without any loss of information, since their behavior is very similar. In this work we will use the Blackman window (although the analysis also works very well with the Tukey window).

Figure 17 – Window functions: rectangular and Parzen.

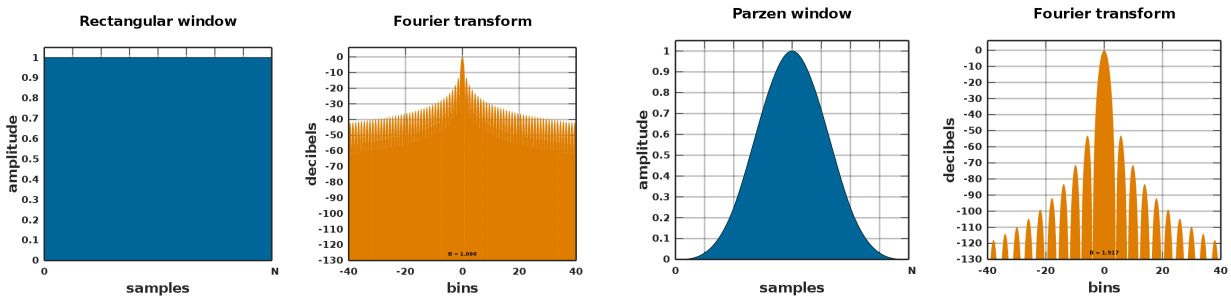

Image source: (WIKIPEDIA, 2021b).

The great importance of using these window functions is to reduce the spectral leakage, which we previously knew as aliasing. Then, before we perform the DFT, we must pass a window function on the signal to ensure that these distortions will be very small.

5.2.3 Filters

The simplest way to build a filter is by using convolutions. We can, for example, create a low-pass filter, choosing up to what frequency of the signal we want to keep. We can also choose one or more ranges of frequencies (bandpass filter) or a minimum frequency from which we want to keep

Figure 18 – Window functions: Tukey and Blackman.

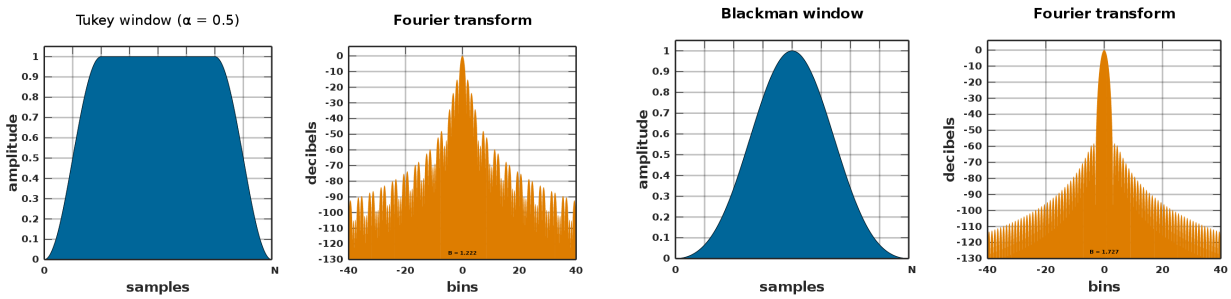

Image source: (WIKIPEDIA, 2021b).

(high-pass). For this, it is enough to perform a convolution between the signal to be analyzed and the desired constraint. To illustrate the case of a low-pass filter, consider that a given signal is represented by an S function and that we must select only the frequencies f below $10Hz$ in that signal. Then we have

```
S_filtered = S * (f < 10)
```

The low-pass filter indicated in this example must be applied in the frequency domain and then just perform the inverse Fourier transform to see how the signal was after filtering.

Another important method is the matched filter. This filtering method is widely used when the signal is completely obscured by noise and filters such as bandpass are not enough to fully evidence the desired signal, or when we do not even know if there is a signal of interest in the middle of the noise. In the case of gravitational wave search, this filter is only possible when we have templates to perform the correlation between the detected signal and the expected signal. It is also worth noting that the use of a particular filter does not exclude the possibility of using others on the same signal. We can initially filter the noise with a bandpass filter, for example, and then use the matched filter. This initial process is called whitening and is mainly used to suppress very high frequencies (much higher than the desired signal). In addition, some types of frequency filters, such as bandpass, can be applied directly in the time domain through convolutions (JOHANSSO, 2019).

Finally, an important family of convolution filters are the so-called FIR and IIR filters. FIR (finity impulse response) filters are of the form

$$y_n = \sum_{k=0}^{M} b_k x_{n-k}, \tag{5.6}$$

where x_{n-k} are the input values from previous times, y_n are the output values and b_k is a coefficient to be determined. The IIR (infinity impulse response) filters are of the form [(JOHANSSO, 2019)]

$$a_0 y_n = \sum_{k=0}^{M} b_k x_{n-k} - \sum_{k=0}^{N} a_k y_{n-k}. \tag{5.7}$$

The equation (5.7) is not exactly a convolution as it also includes previous values from the y output, but

its general appearance is very similar. Computing the values of b_k and a_k given a set of filter properties is known as filter design. To apply these filters, we can use the lfilter function of Scipy's signal module, as

```
S_filtered = signal.lfilter(b, 1, S)
```

where b represents the coefficient b_k and S is the signal to be filtered. We can also take

In: b, a = signal.butter(2, freq, btype='high')

where a and b are the coefficients a_k and b_k, freq is the critical frequency of the filter and btype='high' is used to indicate whether the filter is of low-pass or high-pass type.

We will see in later section which of these filters are more appropriate for the analysis of the simulated signals used in this work.

5.3 POST-NEWTONIAN APPROXIMATION

We saw in chapter 2 that, when the gravitational field is considered moderate, the Newtonian theory of gravitation becomes insufficient and it is necessary to insert relativistic corrections in the theory. We have also seen that this modification is called the post-Newtonian approximation and is the tool we need to describe the inspiral phase of compact binaries. We know that in the post-Newtonian theory, expansions of the GR equations of motion are made using as a parameter the ratio between the speed of the objects that form the binary system and the speed of light. However, this expansion is only useful during the inspiral phase because, as the compact objects approach each other, the gravitational field becomes very intense, i.e., the problem becomes highly relativistic and, then, GR as we have seen becomes the most appropriate tool.

Given that the merger stage is well known and is precisely the stage detected by current observatories, in this chapter we will simulate the expected signal for the gravitational wave long before the merger, where the post-Newtonian approximation is still valid. We will see that the shape of these gravitational waves will be very similar to what we would expect to observe from periodic sources as the variation in frequency and amplitude will be very small compared to the changes that occur during the merger.

To create the simulated signals, we first need to find the waveform that will be obscured by noise, i.e., we need to build our templates. With the new equations of motion that appear in the post-Newtonian theory it is possible to rewrite the tensor $h_{\mu\nu}$ and, consequently, it is possible to formulate the energy and flux of emission of gravitational radiation. This path leads to the formulation for the polarizations of gravitational waves, and then it would be enough to plot the waveforms. In this work we will only be interested in the analysis of the simulated signal and therefore we will not go into details about the calculations involved in creating the template (although part of this calculation has been demonstrated in chapter 3). For more details, all these theoretical calculations are fully developed in (LUCCHINI, 2022) and the codes used to create the templates are available in (LUCCHINI, 2021). This procedure, as well as the generation of waveforms, were done using the SageMath software and

the complete codes for the noisy data are available in (MORAES, 2022). All signals were masked with random, normally distributed noise and with amplitudes greater than the template.

5.4 SIMULATED SIGNAL ANALYSIS

Finally we have all the necessary tools to start the analysis of some simulated signals. The purpose of this section is to bring a study of the inspiral stage of compact binaries. We saw in chapter 2 that gravitational waves have very small amplitudes and are extremely difficult to detect. Currently observatories can only detect the signal at the moment when two compact objects merge because the gravitational waves emitted in the process before it are outside the detectors' sensitivity range. However, we know that the inspiral stage is well modeled by post-Newtonian theory and then we can simulate some gravitational wave signals from sources which parameters are already known.

The first simulated inspiral signal that we will analyze is the Hulse-Taylor binary PSR 1913+16 (5.4.1). Next, we will analyze the simulation of the events GW170817 (5.4.2) and GW190426_152155 (5.4.3) detected by the LIGO-Virgo collaboration. The event GW170817, mentioned earlier, was the merger of two neutron stars and was also the first event to be simultaneously observed in all electromagnetic range. The third event, GW190426_152155, was the merger of a black hole with another compact object, which is still unknown whether it was a black hole or a neutron star.

As aforementioned, the three signals were initially masked by random, stationary noise with a much larger amplitude than the signal. This scenario is very close to what happens in current detectors with the only difference that the noise will not have specific patterns as in observatories (we have seen that instrumental noise, for example, has a well-known behavior and is always repeated in all observations).

It is also important to note that all the analyzes that will be discussed in the following sections were intended to be based solely on the signal with noise, as if the template did not exist, so that there would be no bias in the search for the frequencies that would be used in the construction of the filters. However, during the research, it became clear that some basic information about the event or noise was needed to ensure more reliable results for the analysis.

In a real context, it is not possible to know if the dataset has any information of astrophysical origin, which makes the analysis very challenging. On the other hand, in a real context, researchers have a database on the behavior of noise, for example, and this has a great impact on the efficiency of the search for these gravitational signals.

With that in mid, our purpose here was just to develop an educational practice tool, with which was possible to test and improve basic knowledge with python language that is fundamental for real analysis. All notebooks (code files created on the Jupyter platform) with the following analysis are available in (MORAES, 2022).

5.4.1 Signal 1: Hulse-Taylor Binary

The Hulse-Taylor binary system, known as PSR 1913+16, was discovered in 1974 by Russell Hulse and Joseph Taylor Jr, whose work (HULSE; TAYLOR, 1975) won them the Nobel Prize in Physics in 1993.

This binary is composed of a neutron star and a pulsar and was the first binary containing a pulsar to be detected. As pulsars emit pulses of radiation at a regular rate and neutron stars are very compact objects, this binary provides a great opportunity for us to test GR in a regime of intense gravitational field. Among all the tests involved in the study of this binary, what is the most interesting for this work is the proof of the existence of gravitational waves. We saw in chapter 2 that the emission of gravitational radiation will steal energy from the binary system forcing the two objects to come closer together. Hulse and Taylor demonstrated that the binary PSR 1913+16 undergoes an orbital decrease of approximately 3.3 mm per orbit (HULSE; TAYLOR, 1975) and this was the first direct observation of the emission of gravitational waves.

Unfortunately, current detectors still do not have the sensitivity needed to directly detect the waves coming from this binary. However, as the parameters of this system (such as masses, orbital frequency, etc.) are known, we can simulate the waveform of the gravitational wave emitted by it. To replicate this analysis, simply follow these steps:

- Plot the template and the signal with noise in the time domain,
- Select a window function and, after applying it to the data and the template, perform the fourier transform (FFT),
- Calculate and plot the power spectral densities (PSD),
- Calculate and plot the amplitude spectral densities (ASD),
- Plot the spectrograms
- Collect information from the plots and start with signal filtering.

The first step is important, since we do not know what kind of information we have. With the time-domain plot it is possible to determine the duration of the signal, the maximum strain value and it will also provide us some first clue about the noise.

In Figure 19, the x-axis contains the information about time (in the order of giga years) and the y-axis contains the strain values. We can notice from the template that the strain values are very small, in the order of 10^{-18}. From the data plot we can see that the noise is greater in amplitude and it mixes completely with the gravitational wave signal.

In general, the detections made by the LIGO-Virgo observatories are also covered by different noises and it is not possible to say that there is information of astrophysical origin in the data only through the visualization in the time domain. Therefore, we need to transform our data to the frequency domain, where we can analyze the behavior of the signal and noise in different frequency bands.

To do this, we first use the Blackman window function on both the data and the template. We have seen that this will cause the edge values to be attenuated and there will be a decrease in possible distortions caused by the FFT.

Now we can perform the FFT and calculate the value of the frequencies associated with each FFT output points. In this step, the frequency of the sample f_s was defined as twice the number of points

Figure 19 – Data: Simulated signal - data with noise. Template- Hulse-Taylor: Template of the signal for the Hulse-Taylor binary system. The upper panel illustrates the complete signal (65536 points) while the lower panel illustrates only the first 5000 points of the signal.

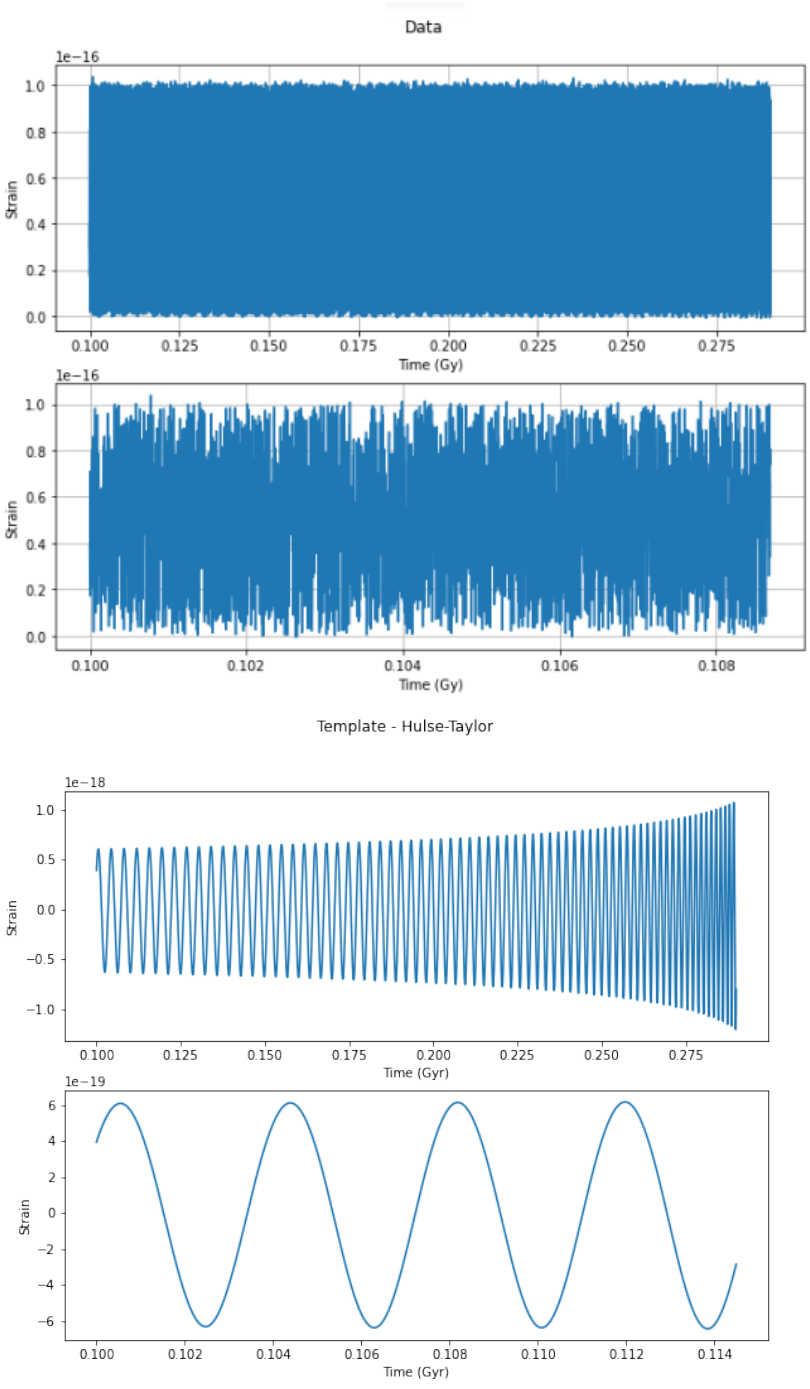

Image source: The author.

in the data. Then, in the frequency domain, the data and the template take the form illustrated in Figure 20.

Note that the plots are on a logarithmic scale. The x-axis represents frequencies and the y-axis represents strain/frequency.

Here comes the first challenge. In a real situation, it is possible to determine at which frequency

Figure 20 – Representation of data (upper image) and template (lower image) in the frequency domain. The observed behavior of the frequency domain signal is due to variations in frequency and amplitude over time. Although the gravitational signal is well behaved, the noise can vary in many different ways.

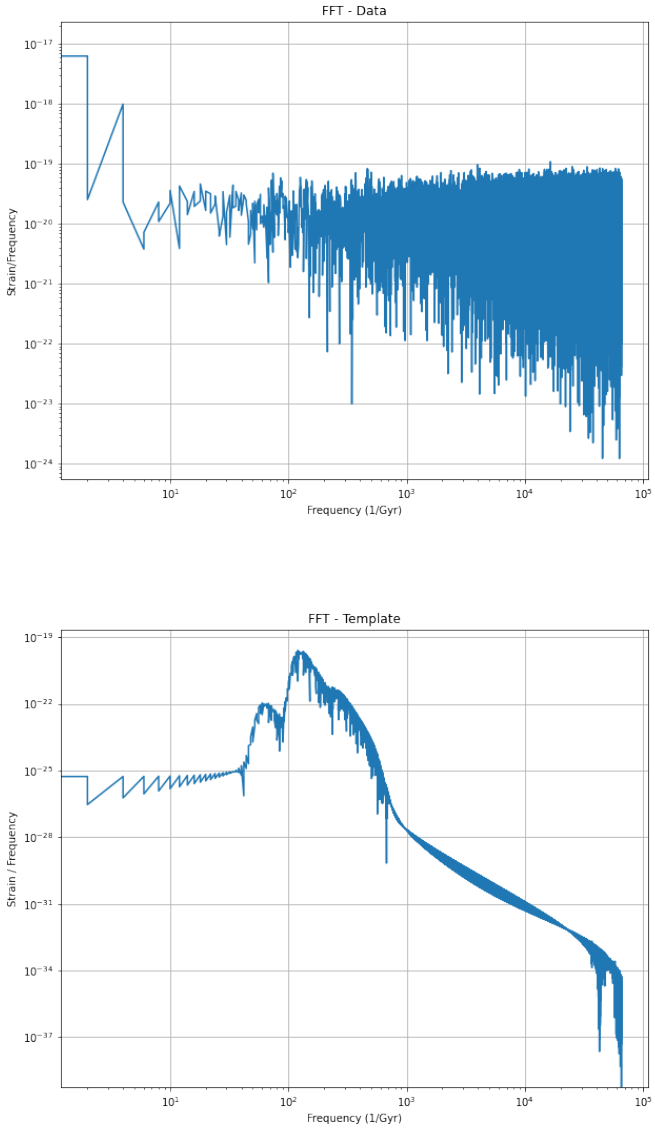

Image source: The author.

there is a predominance of noise (and which noise) since a considerable amount of them is already well known. However, this signal is immersed in completely random noise. There is no known pattern and therefore the plot of figure Figure 20 is still insufficient to draw any conclusions. The only thing that we can highlight at this point is that there are very marked peaks in the template in a specific frequency range. Ideally, as previously mentioned, we would not look at the template during the analysis. However, there is no way to make statements with just the noisy data since we are in a different context and with fewer resources than it would be in a real analysis. With this information from the template, we can turn our attention to the noisy data and look for some behavior that fits the

signal.

In order to extract more information from the data, we will calculate and plot the power spectral density (PSD) of both the noisy data and the template. During the merger, it is expected that the gravitational signal has greater power than the noise, which helps in its identification on the PSD. Even during the inspiral stage, the signal should also stand out. However, we can not guarantee that this behavior would be maintained in this analysis, since the noise can have an absolutely different behavior than expected in a real situation. We can look for these patterns but, in principle, we can not make statements without studying more deeply about the noise present in these simulations.

Figure 21 – PSD of the noisy data (upper image) and the template (lower image).

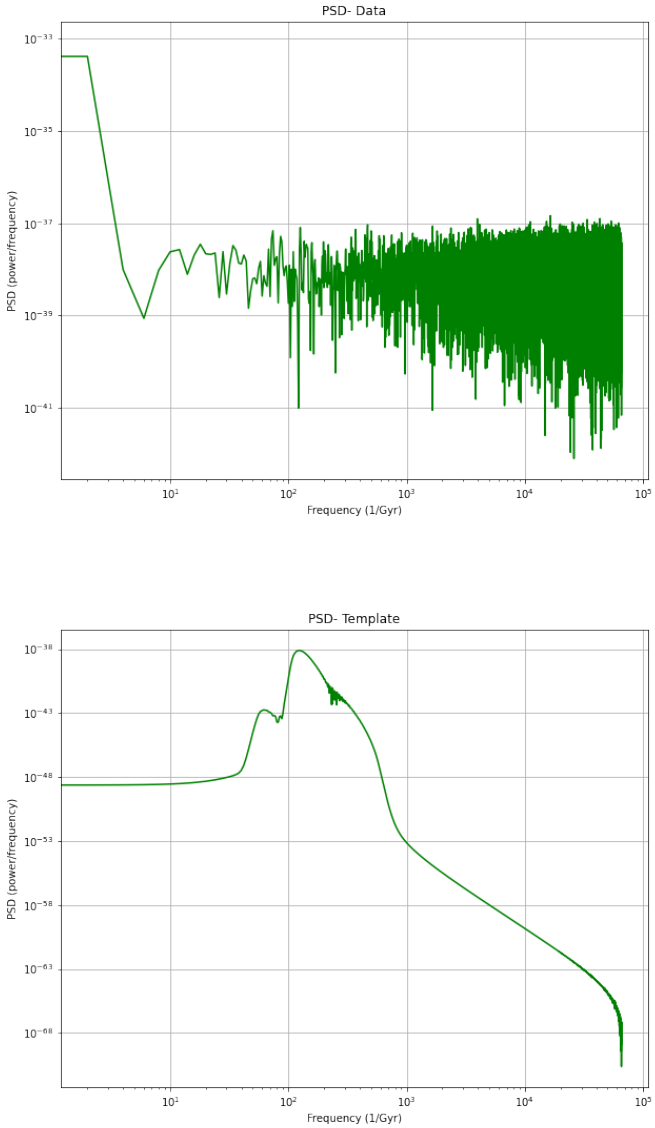

Image source: The author.

In Figure 21, once again, the plot does not show any very evident peaks in the noisy signal. This tells us that the noise and the gravitational wave signal are very close in frequency. This also tells us that it will be very difficult to separate them when filtering. This is in fact a problem that also

appears in a real scenario of analysis. What makes it so challenging to identify gravitational waves from periodic sources such as the Hulse-Taylor binary is that, in addition to being present during the entire observation period, they have a much lower frequency than during a merger. This causes them to be confused with noises of instrumental origin. Current observatories do not have the sensitivity needed to make this distinction.

We can also try to plot the amplitude spectral density (ASD) and spectrogram of the noisy data and the template. The results is shown in Figure 22.

Figure 22 – ASD of the noisy signal (upper) and the template (lower).

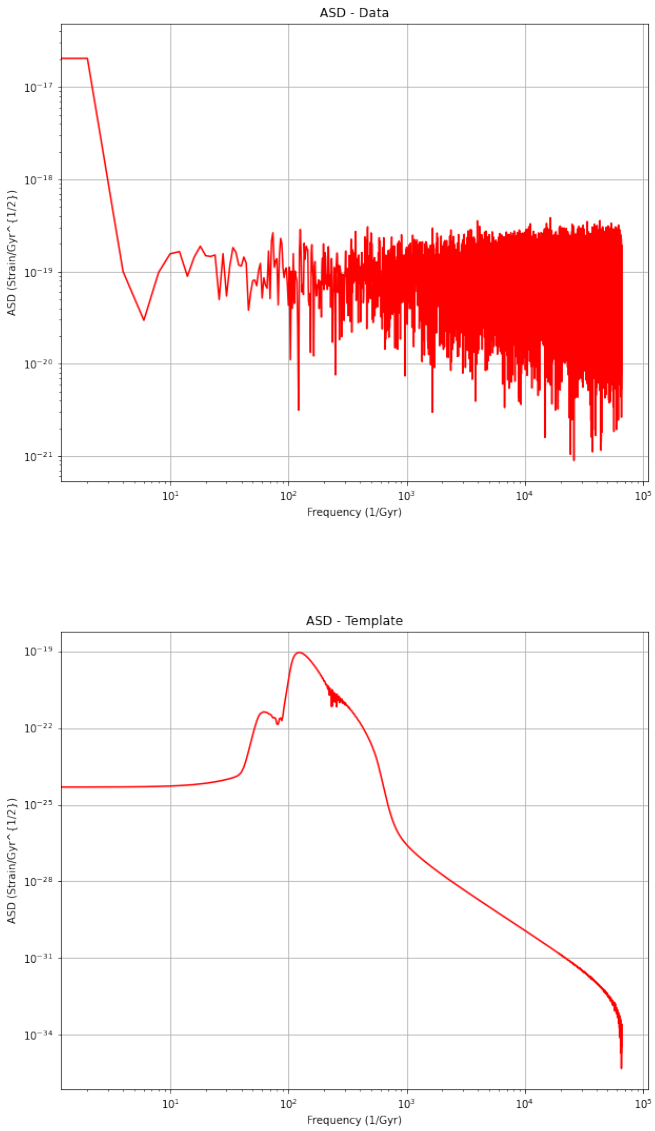

Image source: The author.

As happened with the PSD, the plot of the ASD does not show great differences and once again we are forced to look at the behavior of the template. In the spectrogram we can see some clearer lines that mark where the signal has greater power but from the noisy signal it is not possible to identify the gravitational wave. This is also very common, even for signals which origin is the merger of compact

Figure 23 – Spectrograms: Template (lower) and noisy data (upper). The color bar indicates (on logarithmic scale) the signal power. Lighter colors indicates greater power and, in this case, also indicates the presence of a gravitational wave.

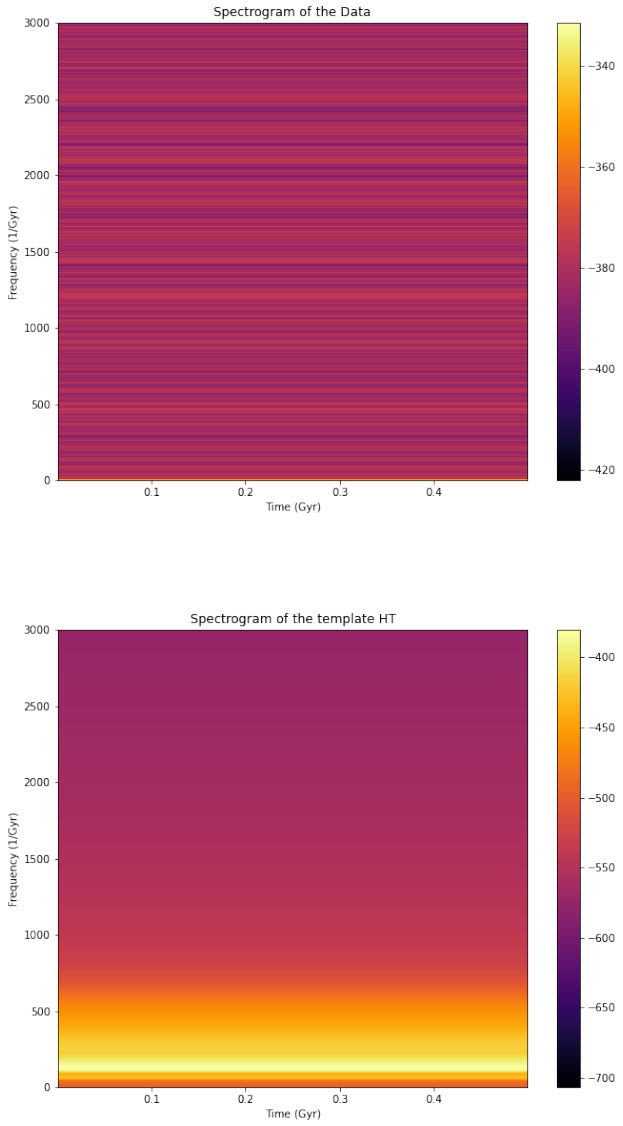

Image source: The author.

binaries. The signal is usually evident after some type of filtering. The same is happening here. If we look to the spectrogram of the template (Figure 23) it is clear that the gravitational wave varies in frequency and has more power in a range that starts very close to 0 Gyr^{-1} and ends above 500 Gyr^{-1}. This is a very large range of frequencies, which makes filtering even more difficult. To make this clearer in terms of international system units, 500 Gyr^{-1} is equivalent to approximately 1,585 $\cdot\ 10^{-24}$ Hz.

Finally, from the spectrogram and the other plots (especially of the template), we can select a frequency range where we believe that most of the gravitational information is and with that build a band pass filter that will intensify the frequencies in this chosen range and suppress the others. For this

particular case, we can select frequencies from 50 Gyr^{-1} to 200 Gyr^{-1} as an initial guess and then make adjustments to the filter.

By varying the filter parameters (initial frequency, final frequency and order) it is possible to notice large variations in the results, with the initial part of the signal being the most difficult to filter correctly. In all the analyzes in this chapter, single and multiple filters were tested for each signal, but the conclusion was that using more than one filter does not bring great benefits and can even suppress considerable parts of the astrophysical signal that we are looking for.

It was also tested another very efficient way to find a gravitational signal that is completely covered by noise: the matched filter. When we do the convolution between the noisy signal and the template, the matched filter output (if normalized) will indicate the signal-to-noise ratio (SNR). This procedure is very useful when we have data with a large time interval but with a comparatively short signal. In this way, the SNR plot will indicate a peak where there is gravitational information, as illustrated in Figure 24.

Figure 24 – Matched Filter of a burst signal: when the signal duration is shorter than the observing duration.

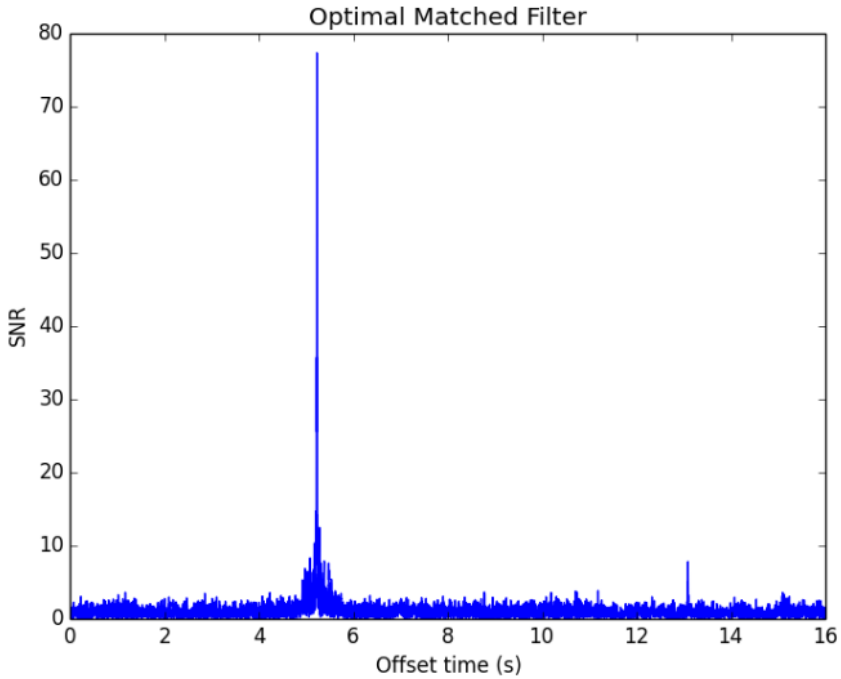

Image source: ((LIGO, 2022)).

Therefore, it makes a lot of sense to use the matched filter in the search for burst signals, for example. However, for continuous signals (as is the case in this work), the SNR plot will only indicate the values of the ratio between signal and noise, but as there is signal and noise in the entire data file, there is no way to differentiate one from the other and, therefore, there is no way to draw any conclusion from the matched filter alone. For the same reason, it is also not useful to use cross-correlation filtering, which is also a convolution between the noisy signal and the template but in the time domain.

The results obtained using a single bandpass filter (between 55 and 140 Gyr^{-1}) are illustrated in Figure 25. If we change the filter frequencies to 291 and 305 Gyr^{-1} we get Figure 26. These

plots shows the signal after filtering (upper) and the comparison of the filtered signal (in red) with the template (in black) on the second panel. On the third and fourth panel we have two different zooms of the signal. One shows the final 5536 points (near the merger) and the other shows the first 10000 points of the signal. We can see that neither of the two situations has good match with the template.

Figure 25 – Results of analysis: Signal after filtering, comparison between the signal and the template and zoom of the initial and final points of the data. The signal after filtering (in blue and black) still doesn't match perfectly the model (red and orange).

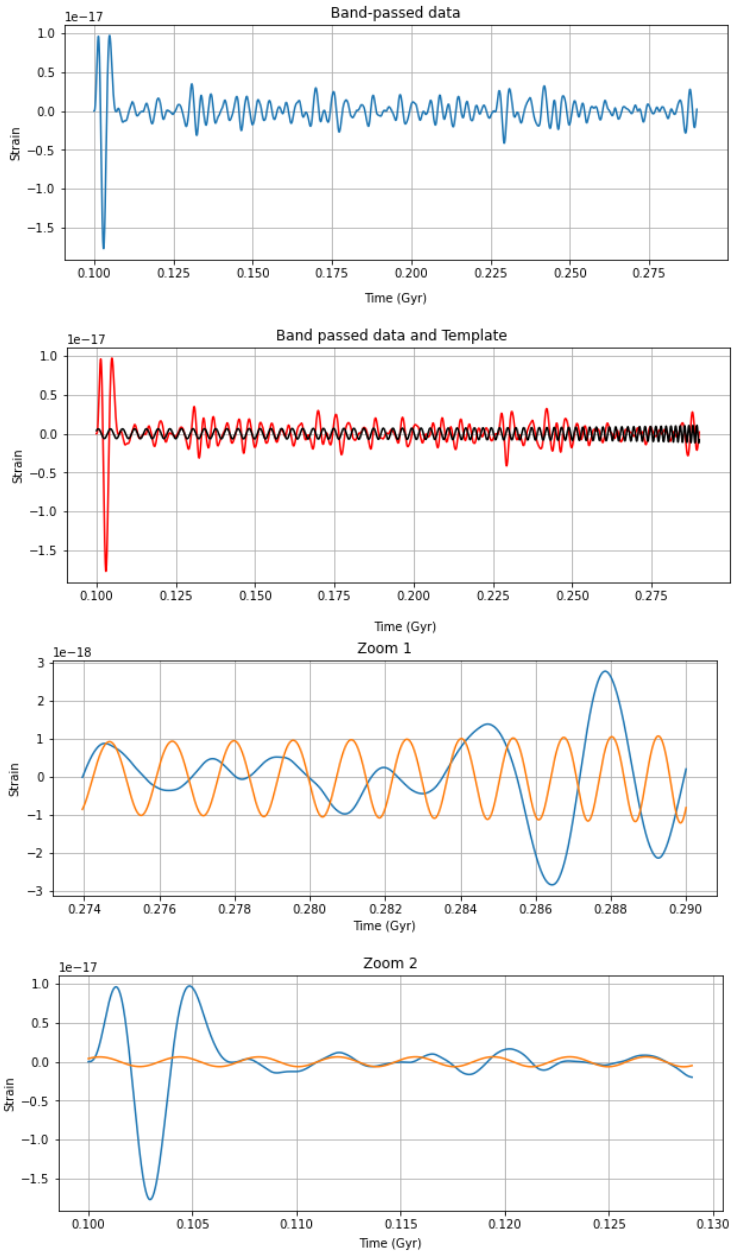

Image source: The author.

When manually testing different frequencies for the filter it became clear that from 1 to 55 and from 300 to 700 Gyr^{-1} the signal is predominantly noise. In fact, as we saw in the other plots, it is likely that the gravitational wave is between 55 and 300 Gyr^{-1}. When applying these values to the filter, it is possible to notice that there is still a lot of noise. Note that we can also plot the spectrogram of the filtered signal (for both bandpass filters suggested above) since it shows which frequency band has the

Figure 26 – Different results for the analysis: by computing another frequency range it is possible to notice how the filtered signal looks completely changed. Here the signal fits the template a little more.

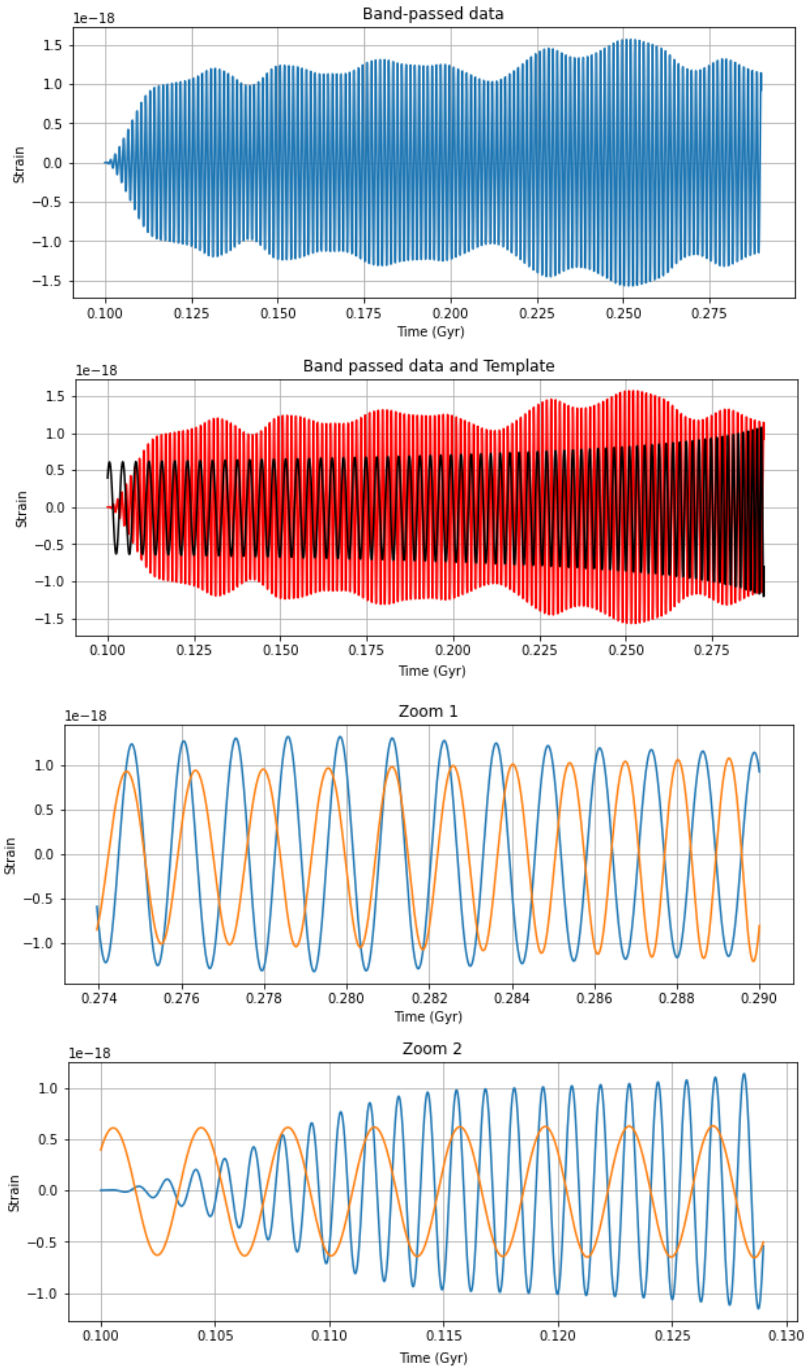

Image source: The author.

greatest power. From Figure 27 one can think that the second suggestion is a better one, considering that we have less noise after filtering (bottom plot). However, we are also filtering a lot of information of the gravitational wave which can be even a bigger problem.

In conclusion, for this analysis there was not a satisfactory result. The factors that may have led to this result are:

- Lack of information and noise pattern: It was not possible to select frequencies that contain only

Figure 27 – Spectrograms of both filtering. In the left we have the result for the first choice of frequencies. We can see that there is still a lot of noise. In the right plot we have the result for the second choise. In that case the frequency range is so narrow that even the gravitation wave is being filtered with the noise.

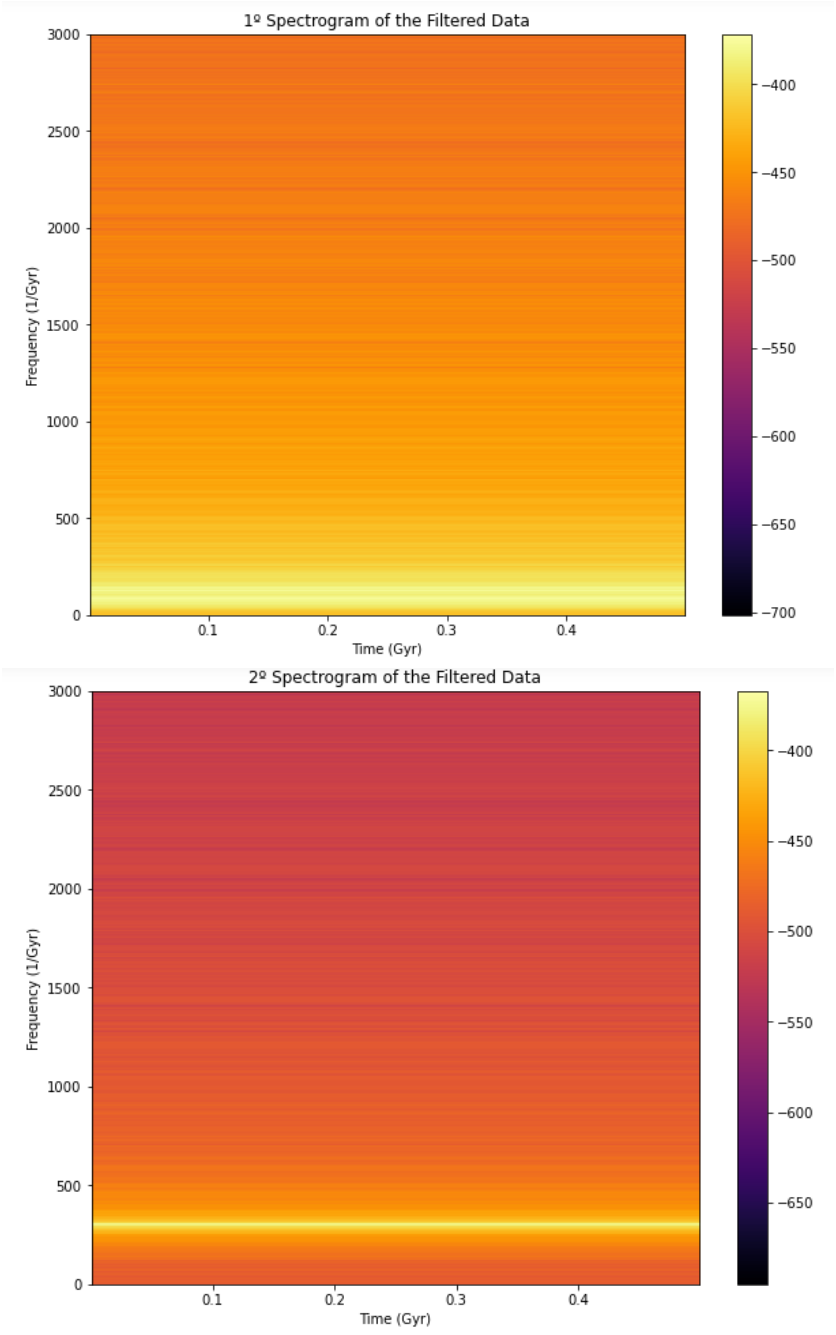

Image source: The author.

(or predominantly) noise.

- The signal comes from a periodic source: This implies a signal throughout the observing time and the further away from the merger, the smaller the wave amplitude. The signal also has a more subtle frequency variation in the inspiral stage than during the merger so it is easily confused with noise.

- The noise was intentionally chosen to have greater amplitude than the signal throughout the

sample. It was also random.

Fortunately, we will see in the next analyzes that, following exactly the same steps, we will reach more satisfactory results.

5.4.2 Signal 2: GW170817

GW170817 was the first detection of gravitational waves from a neutron star binary. This event was very important because radiation in the entire electromagnetic spectrum was also detected, guaranteeing an enormous amount of astrophysical information. However, the signal detected by the LIGO-Virgo observatories only represents the moment of the merger of these stars. So, as we did with the Hulse-Taylor binary, it is possible to simulate the inspiral stage of this binary and analyze how the waveform would appear in the detector if they had the necessary sensitivity.

Once again, we will start the analysis by plotting the noisy data and the template in the time domain. Figure 28 (left) shows what is our data. As in the previous case, it is not possible to identify the gravitational wave directly with this plot.

Figure 28 – Data with noise: Simulated signal of the inspiral stage of a NSBH binary. The simulated waveform was covered with random noise and it is not possible to visualize it without performing some noise filtering. Template: Simulated waveform for the event GW170817 based on the parameters provided by the LVK collaboration.

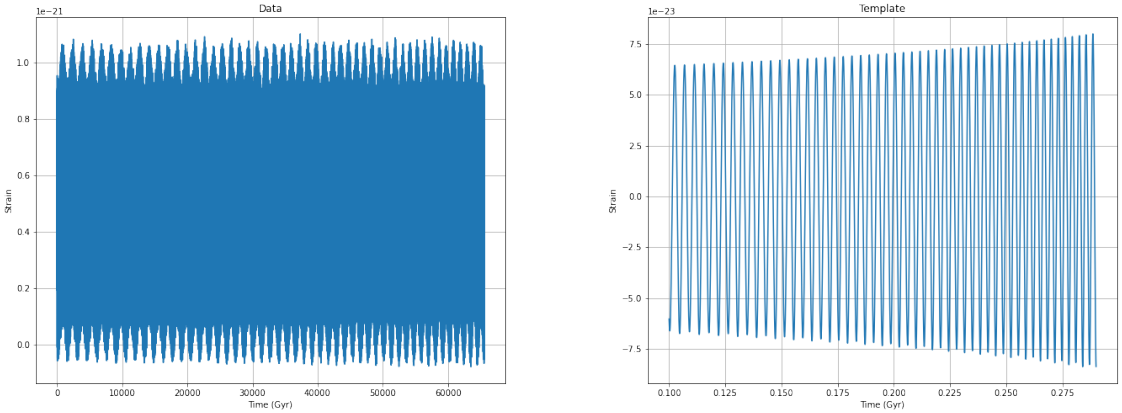

Image source: The author.

Figure 28 illustrates the template (on the right) for this signal and here it is worth making some observations. Note initially that the noisy signal is on the order of 10^{-21} while the template is on the order of 10^{-23}. These are the amplitudes we are interested for the main signal and for the residual signal after filtering. Again the time is in giga years (Gyr). Note how there is no clear evidence of the presence of the signal in Figure 28 (left). To extract the information needed to build the filters, we need to pass the signal (and the template) to the frequency domain. Figure 29 represents the noisy signal and the template after the FFT.

From the two previous plots we can extract the following information: From Figure 29 it is possible to notice the erratic behavior of noise predominance at frequencies below $\sim 10^2 Gyr^{-1}$. Around

Figure 29 – FFT of the data with noise and the template: transforming the signal from the time domain to the frequency domain.

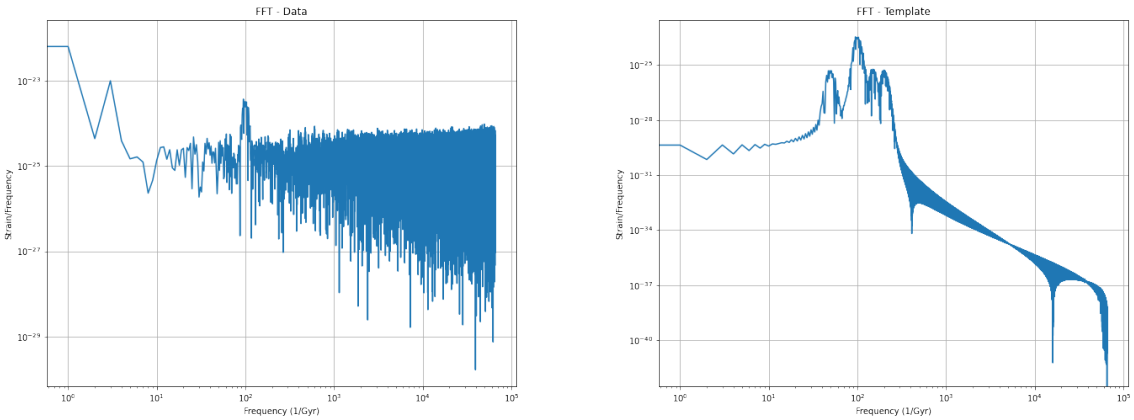

Image source: The author.

$10^2 Gyr^{-1}$ we have a very accentuated and well behaved peak, giving us a first indication of where the gravitational wave is. Above this frequency we have a mixture of gravitational signal with noise (with a greater predominance of noise). It is clear from these plots that this is a different situation from the previous case. Here appears a very marked peak in the noisy signal. This makes it much easier to identify the gravitational wave. We can even safely say that the frequencies before and after this peak are predominantly noise and can be discarded by the filter.

When analyzing the template, we see in Figure 29 how the gravitational wave have "cycles" and varies its frequency over time, which makes it difficult to identify a maximum and minimum value that we should not ignore when filtering the signal. Then, as an initial guess, we can select frequencies between 30 and 200 Gyr^{-1} as the main range, keeping in mind that our filter will inevitably filter some gravitational information along with the noise. Finally, it is also important to note that for this FFT we also used $f_s = 2 \times 65536$, i.e., instead of defining a specific value for the frequency of the gravitational wave, we can directly define the number of points to be considered in the Fourier transform. As the file contains 65536 points, f_s was defined as twice that value (as required by Nyquist's theorem), however, the analysis can also be done with any other integer multiple of 65536. Subsequently we make the PSD and ASD of the noisy signal and the template, as shown in figure Figure 30 and Figure 31.

As mentioned before, the PSD helps us to find in which sections the signal has greater power. This procedure is very useful not only to identify where the gravitational wave may be, but also to identify noises that follow some pattern, as happens with instrumental noises. In Figure 30 we can see that the peak is compatible with the frequency range we selected earlier. Then, we can plot the ASD. From Figure 31 we can see more clearly where the greatest amplitudes are, which is compatible with the discussion for the FFT.

Lastly, before starting to build our filter, it is interesting to plot the spectrograms. Figure 32 illustrates the spectrogram of the template on the right and of the signal with noise on the left. Notice in the template plot how the gravitational wave appears in all data points, has greater power (in yellow) and is contained in a very restricted range of frequencies. In the noisy signal spectrogram it is possible

Figure 30 – PSD of the data with noise nas the template: These figures highlights the points where the signal has the greatest power. This procedure helps to show where the gravitational wave is and, in a real context, it also helps to identify patterns in the noise. In this work we will use the template to help visualize the information that appears in the noisy data. Then we can compare this PSD with the previous one to confirm our choices for the frequency used in the filter.

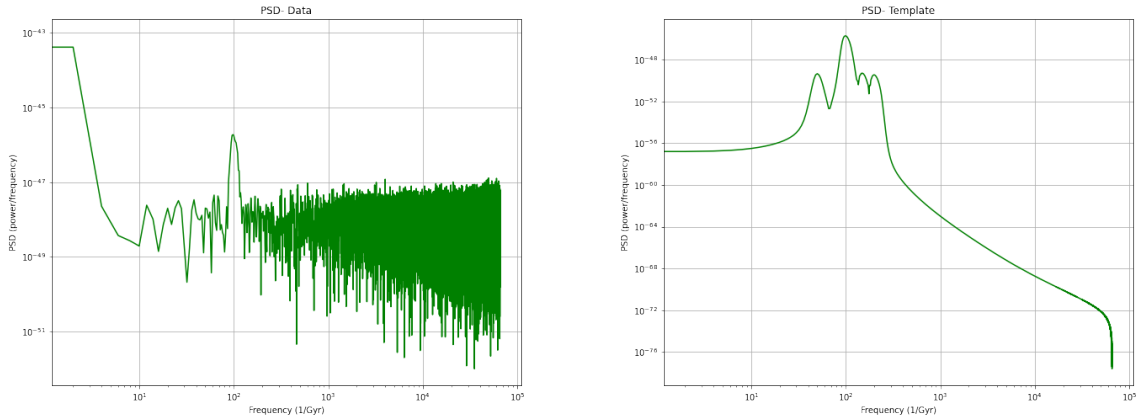

Image source: The author.

Figure 31 – ASD of the signal with noise and the template: On the left we have the ASD of the noisy signal and on the right the ASD of the template.The plot, as the name suggests, helps us find at which points the signal has the greatest amplitude.

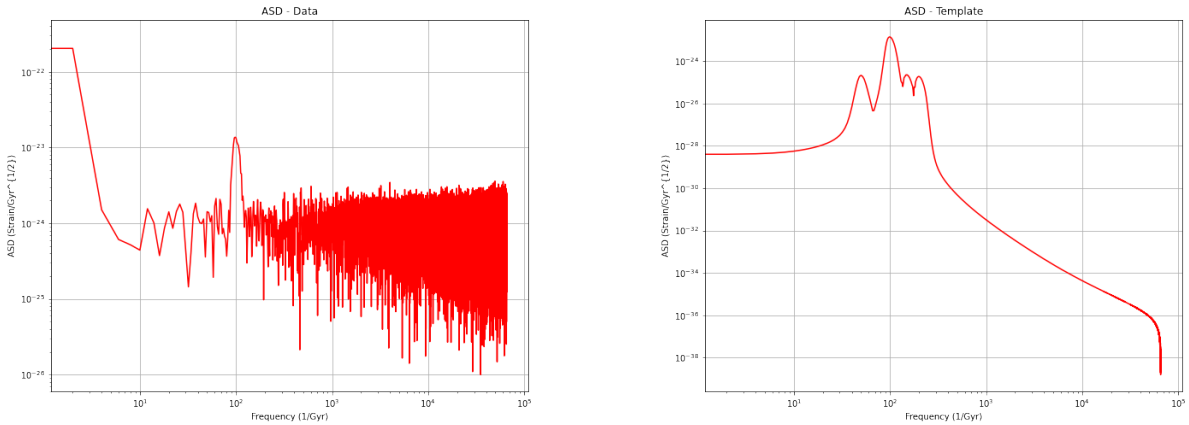

Image source: The author.

to identify that there is a gravitational wave in the data, which was impossible in the previous case. Our intention will be, after filtering, to plot a new spectrogram and see if the gravitational signal become even more evident.

Therefore, with all this information in mind, we can once again use a bandpass filter to extract as much of the noise as possible and highlight the gravitational signal. In Figure 33 (left upper panel in blue)w e can see, in the time domain, the result of filtering the signal when we select only the frequencies from 75.5 Gyr^{-1} to 195 Gyr^{-1}.

Figure 32 – Spectrograms: On a logarithmic scale, spectrograms relate time, frequency and signal strength. With it we can see patterns in the signal that can indicate the presence of a signal of astrophysical origin or even noises of instrumental origin, which are repeated in all detections.

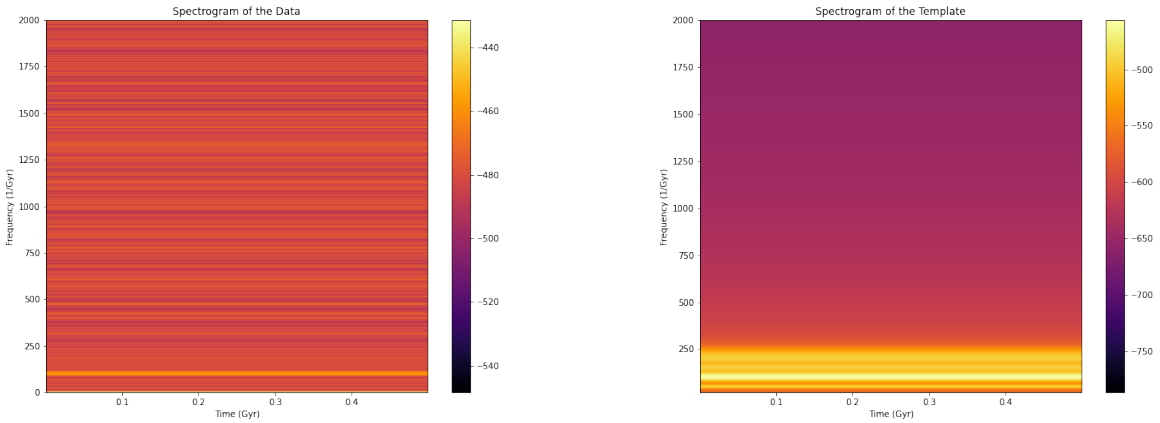

Image source: The author.

Figure 33 – Signal after noise filtering: These are the results of the filtering and the comparison between the final signal and the expected signal (template).

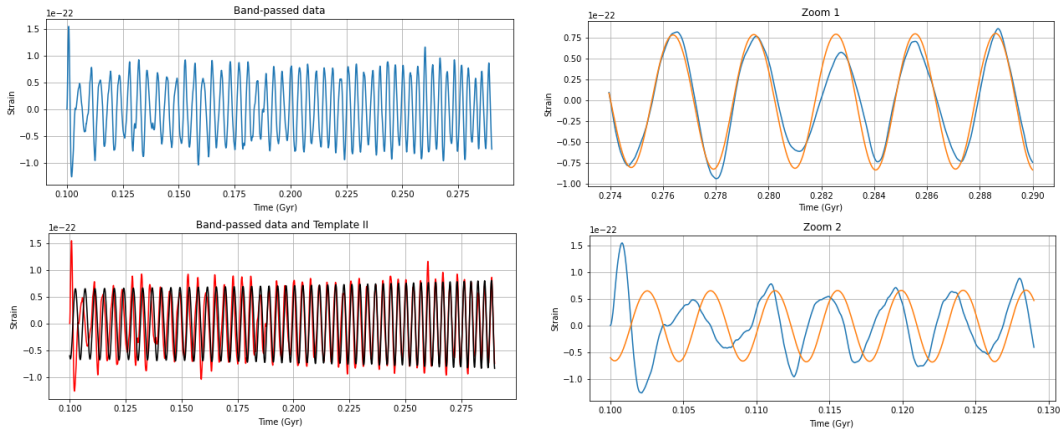

Image source: The author.

Notice how the order of magnitude of the strain went to 10^{-23} m and that the gravitational signal is already completely evident. To make this even clearer, we can compare this result with the template.

In Figure 33 (left bottom panel) we have the comparison between the filtered signal (red) and the template (black). We then see that the result fits very well the expected signal. We can also zoom in on the first (bottom plot) and last (upper plot) data points and with that we will see that the signal is almost perfectly fitted to the template (plots on the right).

To finish this analysis, we need to plot the residual signal and the spectrogram after filtering (Figure 34). At this point it is interesting to note how the gravitational wave signal appears clearly in this new spectrogram and that, in fact, we managed to get most of the noise out. When comparing with the spectrogram of the template (Figure 32 right plot), we see that our result was very similar. This is a good result and is similar to what happens in a real situations. In general, it is not possible to remove

Figure 34 – Residual signal and the signal after filtering.

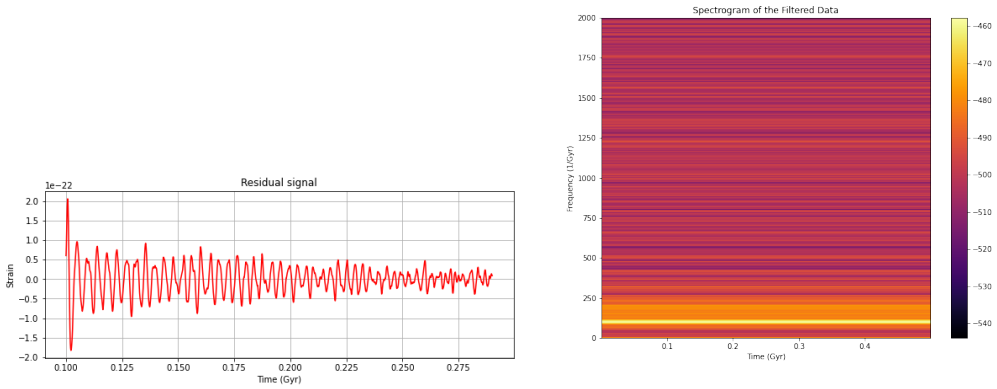

Image source: The author.

all the noise because many of them are mixed in the same frequency bands as the gravitational wave and, therefore, it becomes impossible to filter one without filtering the other. However, by knowing the patterns present in the noise and having a huge bank of templates, it is possible to obtain a very "clean" result.

This analysis was a little less challenging than the previous one and, even with little information, it was possible to extract a lot of the astrophysical signal.

5.4.3 Signal 3: GW190426_152155

To finish our analysis of simulated inspiral signals, we will study the event GW190426152155, which origin is not yet known. Once again we will consider the signal of the inspiral stage of this event

Figure 35 – Data with noise and template fo the event GW190426_152155.

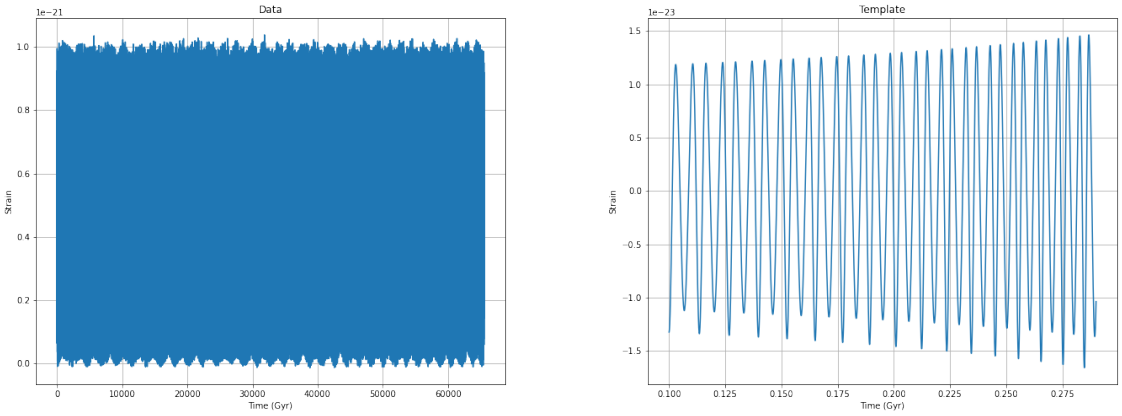

Image source: The author.

being suppressed by random noise and we will follow exactly the same procedures as we did in the previous analyses. Therefore, we start with the plot of the noisy signal and the template.

Figure 35 is again in the time domain (in giga years) and we can see how in this case it is even more difficult to identify any gravitational signal due to the noise. It is also possible to notice how the

behavior of the template is also slightly different from the previous one. These variations in the strain value happen due to limitations in the post-Newtonian approximation. Then we can plot the Fourier transform of the noisy signal and the template.

Figure 36 – FFT of the data and the template.

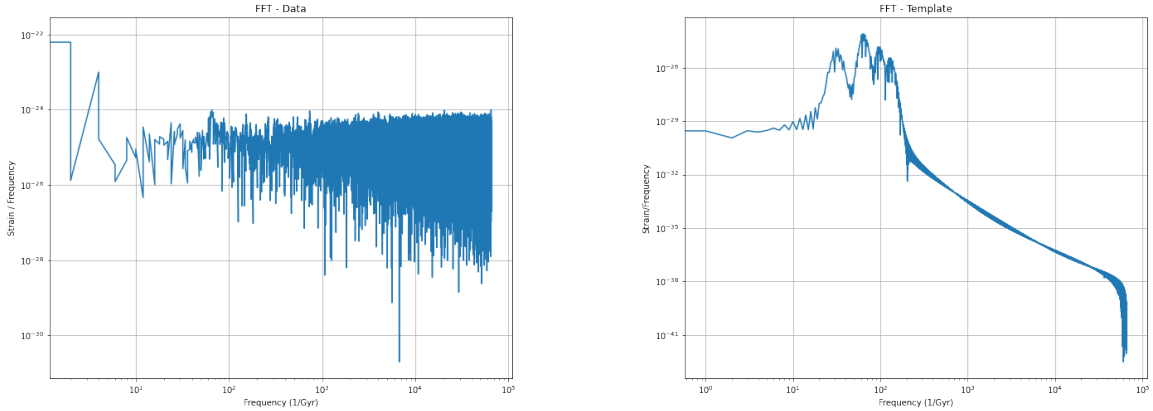

Image source: The author.

Figure 36 illustrates the signal with noise on the left and the template on the right. Here we can notice that, although very similar to the previous case, it is more difficult to identify the interval that contains the gravitational wave, even in the frequency domain. Generally this tells us that the noise and the signal are very close in frequency and possibly there would be too much noise left after filtering. However, in this case we have another important factor to consider which is the irregular behavior of the signal caused by the PN approximation. Because it is a theory limited to a moderate gravitational field regime, the signal ends up suffering distortions that add an additional difficulty to the analysis. In order to try to extract the information we need to make a bandpass filter, we already know that we need to plot the PSD and ASD of both cases (signal with noise and template).

Figure 37 – PSD of the data and the template.

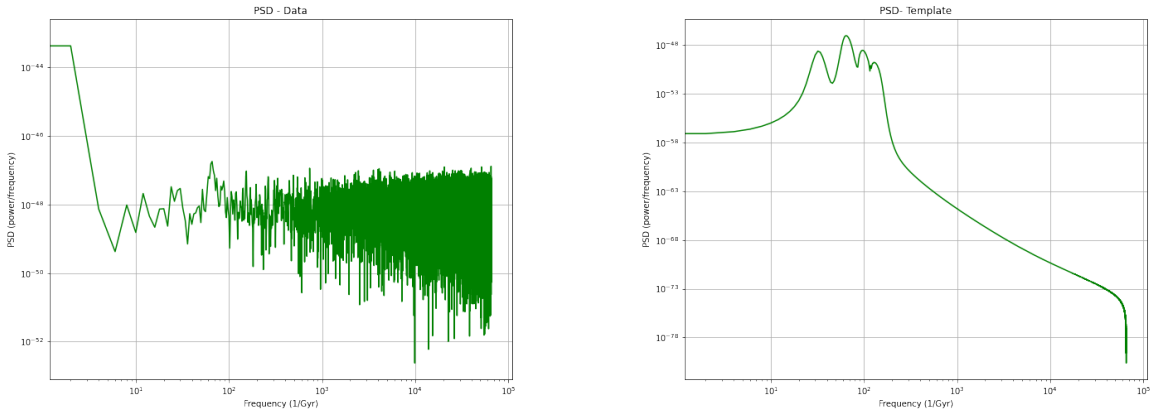

Image source: The author.

In Figure 37 it is possible to notice that a small peak begins to appear around $10^2\ Gyr^{-1}$. Another way to identify a more accurate value for these frequencies is to plot the template outside the logarithmic scale, but this will not be done in this work, since our goal is to test the behavior of the filter in different ranges to gain practice and knowledge about the signal.

Figure 38 – ASD of the data and the template.

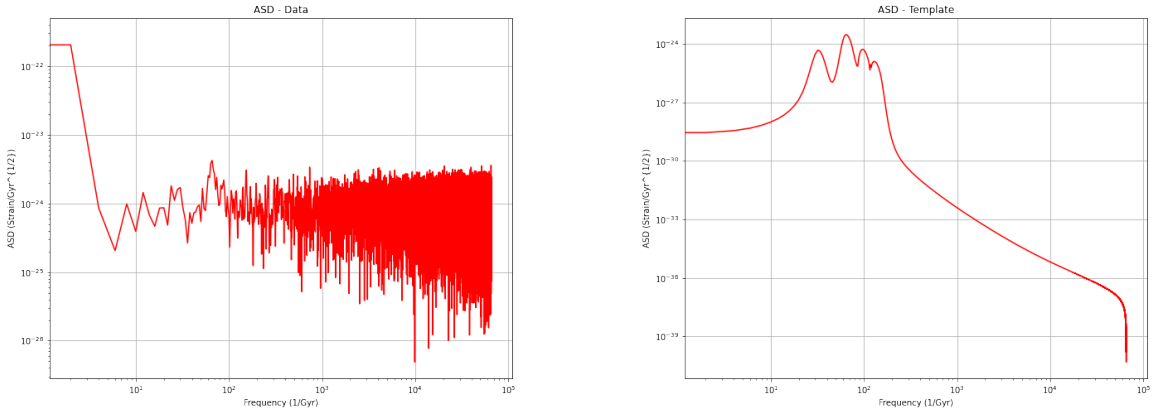

Image source: The author.

The same happens with the ASD plot, where the peak is even more evident than in Figure 36.

Figure 39 – Spectrograms: Data with noise (left) and template (right).

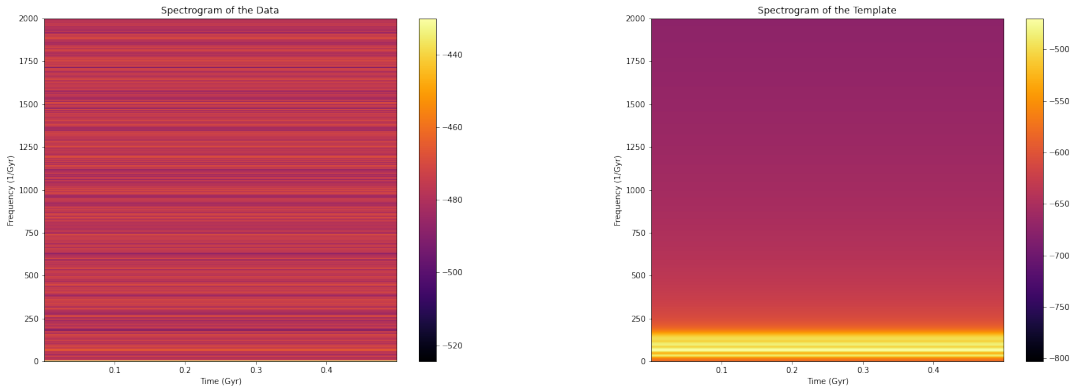

Image source: The author.

Figure 39 illustrates the spectrogram of the template on the right and the noisy signal on the left. Once again we can see that the gravitational wave is not evident from the spectrogram of the noyse data and, from the template, we can sse that the gravitational signal will have a restricted variation in frequency.

To filter this signal, a bandpass filter was used once again, but at this time between the frequencies 42 Gr^{-1} and 90 Gyr^{-1}. The results are in the following figures. In Figure 40 we can see the signal after filtering (right upper panel), the comparison between the filtered signal and the template (right

bottom panel), the zoom of the last 5536 points of the signal (left upper panel) and the zoom of the first 10000 points of the signal (left bottom panel) .

Figure 40 – Signal after filtering.

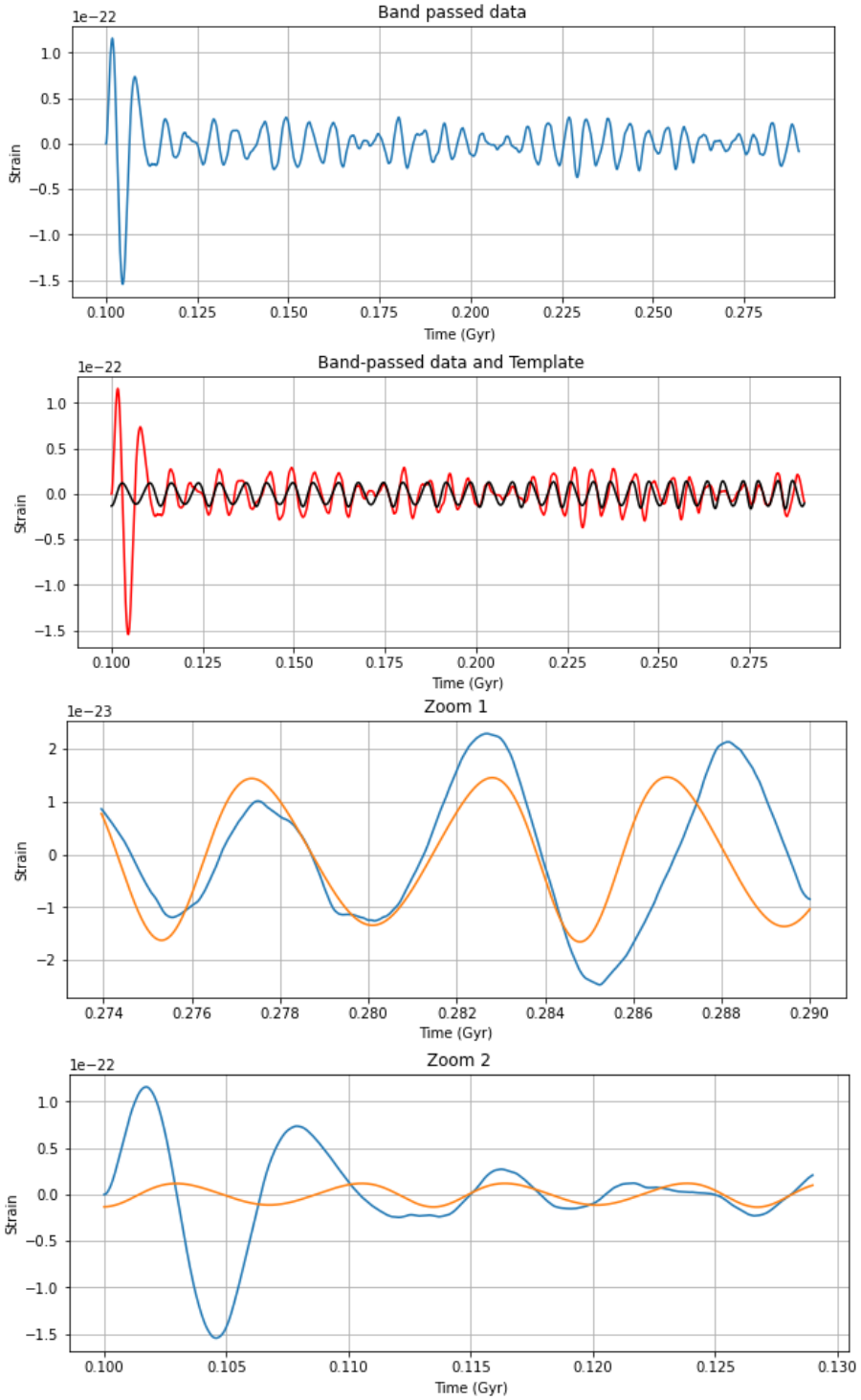

Image source: The author.

Fortunately our initial assumption was close enough. Figure 40 shows that the filtered signal fits the template relatively well but, once again, there is still a lot of noise associated with the beginning of the signal. Unfortunately, using a larger number of point for the FFT, narrower frequency bands in the filter or multiple filters was not enough to solve this problem.

Figure 41 – Residual signal and spectrogram of the filtered signal.

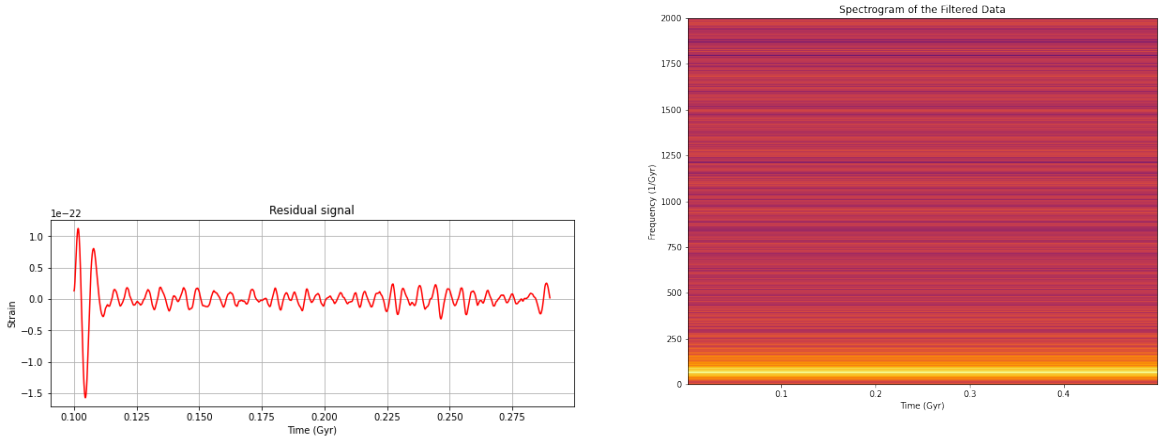

Image source: The author.

Figure 41 shows the residual signal and the spectrogram of the signal after removing the noise. In it is possible to notice the great similarity with the template, showing that the filtering was done correctly.

With this, we can conclude that the search for gravitational waves in stages before the merger is a great challenge. It is necessary to have a prior knowledge of the noise and even the expected signal to be able to carry out a more complete analysis, however, even some simpler filtering methods can help us to extract some relevant information.

6 CONCLUSIONS

The initial proposal of this research was to approach different aspects involved in the study of gravitational waves. We have seen that since the publication of general relativity, this phenomenon has been studied and tested. The first studies were intended to verify if this phenomenon was in fact a prediction of the theory. Then came the studies on the generation and propagation of these waves, revealing their nature, their effects when interacting with matter, which led, years later, to the construction of huge detectors such as LIGO. Finally, the first direct detection of these waves marked the beginning of a new period of exploration in this area and triggered a new approach of study through computation. We have also seen that theories of gravitation have changed over the years and that there are currently several proposals for modifying general relativity, such as massive gravity.

We can therefore conclude that all these aspects were explored in this work and that the objectives of this research were achieved. We can also conclude that there is still much to be studied about this phenomenon. With the development of space detectors such as LISA, it is hoped that we will be able to test theories beyond general relativity. In addition, with greater sensitivity, it will be possible to detect and analyze different types of sources other than the merger of compact binaries.

The simulation of gravitational wave signals proved to be an excellent tool to train and learn more about the data analysis techniques currently used. With this, it was possible to learn about the challenges involved in the search for gravitational wave signals and the importance of certain filtering processes. The results obtained were satisfactory and the discussions very wealthy.

BIBLIOGRAPHY

ABBOTT, B. et al. Observation of gravitational waves from a binary black hole merger. **Physical Review Letters**, American Physical Society (APS), v. 116, n. 6, Feb 2016. ISSN 1079-7114. Disponível em: <http://dx.doi.org/10.1103/PhysRevLett.116.061102>. Acesso em: 09 jul. 2022.

ABBOTT, B. et al. Gw170817: Observation of gravitational waves from a binary neutron star inspiral. **Physical Review Letters**, American Physical Society (APS), v. 119, n. 16, Oct 2017. ISSN 1079-7114. Disponível em: <http://dx.doi.org/10.1103/PhysRevLett.119.161101>. Acesso em: 09 jul. 2022.

ABBOTT, B. et al. Tests of general relativity with the binary black hole signals from the ligo-virgo catalog gwtc-1. **Physical Review D**, American Physical Society (APS), v. 100, n. 10, Nov 2019. ISSN 2470-0029. Disponível em: <http://dx.doi.org/10.1103/PhysRevD.100.104036>. Acesso em: 09 jul. 2022.

ABBOTT, B. P. et al. The basic physics of the binary black hole merger gw150914. **Annalen der Physik**, Wiley, v. 529, n. 1-2, p. 1600209, Oct 2016. ISSN 1521-3889. Disponível em: <http://dx.doi.org/10.1002/andp.201600209>. Acesso em: 09 jul. 2022.

ABBOTT, R. et al. Gw190521: A binary black hole merger with a total mass of 150m. **Physical Review Letters**, American Physical Society (APS), v. 125, n. 10, Sep 2020. ISSN 1079-7114. Disponível em: <http://dx.doi.org/10.1103/PhysRevLett.125.101102>. Acesso em: 09 jul. 2022.

ABBOTT, R. et al. Gwtc-2: Compact binary coalescences observed by ligo and virgo during the first half of the third observing run. **Physical Review X**, American Physical Society (APS), v. 11, n. 2, Jun 2021. ISSN 2160-3308. Disponível em: <http://dx.doi.org/10.1103/PhysRevX.11.021053>. Acesso em: 09 jul. 2022.

ABBOTT, R. et al. Tests of general relativity with binary black holes from the second ligo-virgo gravitational-wave transient catalog. **Physical Review D**, American Physical Society (APS), v. 103, n. 12, Jun 2021. ISSN 2470-0029. Disponível em: <http://dx.doi.org/10.1103/PhysRevD.103.122002>. Acesso em: 09 jul. 2022.

ABBOTT, R. et al. Gw190814: Gravitational waves from the coalescence of a 23 solar mass black hole with a 2.6 solar mass compact object. **The Astrophysical Journal**, American Astronomical Society, v. 896, n. 2, p. L44, Jun 2020. ISSN 2041-8213. Disponível em: <http://dx.doi.org/10.3847/2041-8213/ab960f>. Acesso em: 09 jul. 2022.

ABUTER, R. et al. Detection of the schwarzschild precession in the orbit of the star s2 near the galactic centre massive black hole. **Astronomy Astrophysics**, EDP Sciences, v. 636, p. L5, Apr 2020. ISSN 1432-0746. Disponível em: <http://dx.doi.org/10.1051/0004-6361/202037813>. Acesso em: 09 jul. 2022.

ADMINISTRATOR. **Cosmic Explorer: a next-generation gravitational wave detector**. 2022. Disponível em: <https://cosmicexplorer.org/index.html#overview>. Acesso em: 09 jul. 2022.

ADMINISTRATOR. **Einstein Telescope**. 2022. Disponível em: <http://www.et-gw.eu/>. Acesso em: 09 jul. 2022.

BAKER, J. G. et al. Comparisons of binary black hole merger waveforms. **Classical and Quantum Gravity**, IOP Publishing, v. 24, n. 12, p. S25–S31, May 2007. ISSN 1361-6382. Disponível em: <http://dx.doi.org/10.1088/0264-9381/24/12/S03>. Acesso em: 09 jul. 2022.

BAKER, J. G. et al. Binary black hole merger dynamics and waveforms. **Physical Review D**, American Physical Society (APS), v. 73, n. 10, May 2006. ISSN 1550-2368. Disponível em: <http://dx.doi.org/10.1103/PhysRevD.73.104002>. Acesso em: 09 jul. 2022.

BONDI, H.; PIRANI, F. A. E.; ROBINSON, I. Gravitational waves in general relativity. 3. Exact plane waves. **Proc. Roy. Soc. Lond. A**, v. 251, p. 519–533, 1959.

BOULWARE, D. G.; DESER, S. Can gravitation have a finite range? **Phys. Rev. D**, v. 6, p. 3368–3382, 1972.

BURNS, C.; AL et. **Scipy Lecture Notes**. 2. ed. [S.l.: s.n.], 2020.

CAMPANELLI, M. et al. Accurate evolutions of orbiting black-hole binaries without excision. **Physical Review Letters**, American Physical Society (APS), v. 96, n. 11, Mar 2006. ISSN 1079-7114. Disponível em: <http://dx.doi.org/10.1103/PhysRevLett.96.111101>. Acesso em: 09 jul. 2022.

CARROLL, S. **Spacetime and Geometry: An Introduction to General Relativity**. [S.l.]: Addison Wesley, 2004.

CASTELVECCHI, D. Black hole at the centre of the galaxy imaged for the first time. **Nature**, Nature, v. 605, 2022. ISSN 403-404. Disponível em: <https://www.nature.com/articles/d41586-022-01320-y>. Acesso em: 09 jul. 2022.

CASTRO, G. C. **Gravitational waves and massive gravitons**. Dissertação (Mestrado em Engenharia Física) — Técnico Lisboa, Lisboa, 2018.

CATTANI, M. **Einstein Gravitation Theory: Experimental Tests**. arXiv, 2010. Disponível em: <https://arxiv.org/abs/1007.0140>. Acesso em: 09 jul. 2022.

COLLABORATION, T. L. S. et al. **GWTC-3: Compact Binary Coalescences Observed by LIGO and Virgo During the Second Part of the Third Observing Run**. 2021. Acesso em: 09 jul. 2022.

COLLABORATION, T. L. S. et al. **Tests of General Relativity with GWTC-3**. 2021. Acesso em: 09 jul. 2022.

CREIGHTON, J. D. E.; ANDERSON, W. G. **Gravitational-wave physics and astronomy: An introduction to theory, experiment and data analysis**. [S.l.: s.n.], 2011.

DAM, H. van; VELTMAN, M. J. G. Massive and massless Yang-Mills and gravitational fields. **Nucl. Phys. B**, v. 22, p. 397–411, 1970.

EINSTEIN, N. R. A. On gravitational waves. **Journal of the Franklin Institute**, v. 223, 1937. ISSN 0016-0032. Disponível em: <https://www.sciencedirect.com/science/article/abs/pii/S0016003237905830?via%3Dihub>. Acesso em: 09 jul. 2022.

FIERZ, M.; PAULI, W. On relativistic wave equations for particles of arbitrary spin in an electromagnetic field. **Proc. Roy. Soc. Lond. A**, v. 173, p. 211–232, 1939.

GENZEL, R.; EISENHAUER, F.; GILLESSEN, S. The galactic center massive black hole and nuclear star cluster. **Reviews of Modern Physics**, American Physical Society (APS), v. 82, n. 4, p. 3121–3195, Dec 2010. ISSN 1539-0756. Disponível em: <http://dx.doi.org/10.1103/RevModPhys.82.3121>. Acesso em: 09 jul. 2022.

HANNAM, M. et al. Where post-newtonian and numerical-relativity waveforms meet. **Physical Review D**, American Physical Society (APS), v. 77, n. 4, Feb 2008. ISSN 1550-2368. Disponível em: <http://dx.doi.org/10.1103/PhysRevD.77.044020>. Acesso em: 09 jul. 2022.

HINTERBICHLER, K. Theoretical aspects of massive gravity. **Reviews of Modern Physics**, American Physical Society (APS), v. 84, n. 2, p. 671–710, May 2012. ISSN 1539-0756. Disponível em: <http://dx.doi.org/10.1103/RevModPhys.84.671>. Acesso em: 09 jul. 2022.

HULSE, R. A.; TAYLOR, J. H. Discovery of a pulsar in a binary system. **Astrophys. J. Lett.**, v. 195, p. L51–L53, 1975.

JOHANSSO, R. **Numerical Phyton: Scientific Computing and Data Science Applications with Numpy, SciPy and Matplotlib**. 2. ed. [S.l.]: Apress, 2019.

LEUNG, S.-C.; NOMOTO, K.; BLINNIKOV, S. Pulsational pair-instability supernovae. i. pre-collapse evolution and pulsational mass ejection. **The Astrophysical Journal**, American Astronomical Society, v. 887, n. 1, p. 72, Dec 2019. ISSN 1538-4357. Disponível em: <http://dx.doi.org/10.3847/1538-4357/ab4fe5>. Acesso em: 09 jul. 2022.

LIGO, C. **Gravitational Wave Open Science Center: Tutorials**. 2022. Disponível em: <https://www.gw-openscience.org/tutorials/>. Acesso em: 09 jul. 2022.

LIGO-CALTECH. **LIGO's Interferometer**. 2015. Disponível em: <https://www.ligo.caltech.edu/page/ligos-ifo>. Acesso em: 23 jun 2021.

LIGO-CALTECH. **O3B CATALOG**. 2021. Disponível em: <https://www.ligo.org/detections/O3bcatalog.php>. Acesso em: 21 fev 2022.

LUCCHINI, A. F. M. . L. **gwarticle**. 2021. GitHub repository. Disponível em: <https://github.com/andrelucchini/gw_article>. Acesso em: 09 jul. 2022.

LUCCHINI, A. F. M. . L. **Ondas Gravitacionais em regime pós Newtoniano**. 2022. Trabalho de graduação - Bacharelado em Física. Acesso em: 09 jul. 2022.

MORAES, T. **Uma introdução à teoria de ondas gravitacionais**. 2019. Trabalho de graduação - Licenciatura em Física.

MORAES, T. **SIMULATED SIGNAL ANALYSIS**. 2022. GitHub repository. Disponível em: <https://github.com/M-TATI/SIMULATED_SIGNAL_ANALYSIS-/tree/main>. Acesso em: 09 jul. 2022.

MORAES, T. d. P. Polarization modes of gravitational waves in the context of massive gravity. **Revista Semana da Física**, Editora da UESC, v. 5, 2021. ISSN 2527-1830. Disponível em: <https://revistasemanafisica.wixsite.com/revistasemanafisica/edicoes>. Acesso em: 09 jul. 2022.

NASA. Hubble space telescope: An overview. **NASA facts**, 2017.

NASA, E. **Laser Interferometer Space Antenna (LISA)**. 2022. Disponível em: <https://lisa.nasa.gov/>. Acesso em: 09 jul. 2022.

PENROSE, R. Gravitational collapse and space-time singularities. **Physical Review Letters**, v. 14, n. 3, p. 57–59, 1965.

PIRANI, F. A. E. Invariant formulation of gravitational radiation theory. **Phys. Rev.**, American Physical Society, v. 105, p. 1089–1099, Feb 1957. Disponível em: <https://link.aps.org/doi/10.1103/PhysRev.105.1089>. Acesso em: 09 jul. 2022.

PRETORIUS, F. Evolution of binary black-hole spacetimes. **Physical Review Letters**, American Physical Society (APS), v. 95, n. 12, Sep 2005. ISSN 1079-7114. Disponível em: <http://dx.doi.org/10.1103/PhysRevLett.95.121101>. Acesso em: 09 jul. 2022.

PRETORIUS, F. **Binary Black Hole Coalescence**. 2007.

RHAM, C. de; GABADADZE, G. Generalization of the fierz-pauli action. **Phys. Rev. D**, American Physical Society, v. 82, p. 044020, Aug 2010. Disponível em: <https://link.aps.org/doi/10.1103/PhysRevD.82.044020>. Acesso em: 09 jul. 2022.

RHAM, C. de; GABADADZE, G.; TOLLEY, A. J. Resummation of massive gravity. **Phys. Rev. Lett.**, American Physical Society, v. 106, p. 231101, Jun 2011. Disponível em: <https://link.aps.org/doi/10.1103/PhysRevLett.106.231101>. Acesso em: 09 jul. 2022.

ROBINSON, I.; TRAUTMAN, A. Some spherical gravitational waves in general relativity. **Proc. Roy. Soc. Lond. A**, v. 265, p. 463–473, 1962.

SAKAI, S. et al. The galactic center: An improved astrometric reference frame for stellar orbits around the supermassive black hole. **The Astrophysical Journal**, American Astronomical Society, v. 873, n. 1, p. 65, Mar 2019. ISSN 1538-4357. Disponível em: <http://dx.doi.org/10.3847/1538-4357/ab0361>. Acesso em: 09 jul. 2022.

SORMANI, C. et al. The mathematics of gravitational waves. **Notices of the AMS**, v. 64, 2017. Disponível em: <https://www.ams.org/publications/journals/notices/201707/rnoti-p684.pdf>. Acesso em: 09 jul. 2022.

TACHINAMI, T.; TONOSAKI, S.; SENDOUDA, Y. Gravitational-wave polarizations in generic linear massive gravity and generic higher-curvature gravity. **Physical Review D**, American Physical Society (APS), v. 103, n. 10, May 2021. ISSN 2470-0029. Disponível em: <http://dx.doi.org/10.1103/PhysRevD.103.104037>. Acesso em: 09 jul. 2022.

VILLARD, R. **Hubble Focus: Galaxies through Space and Time**. [S.l.]: (GSFC, 2019.

WIKIPEDIA. **Convolution**. 2021. Disponível em: <https://en.wikipedia.org/wiki/Convolution>. Acesso em: 23 jun 2021.

WIKIPEDIA. **Window function**. 2021. Disponível em: <https://en.wikipedia.org/wiki/Window_function>. Acesso em: 23 jun 2021.

WILL, C. M. **Theory and Experiment in Gravitational Physics**. [S.l.: s.n.], 1993. ISBN 978-0-511-56424-6.

ZAKHAROV, V. I. Linearized gravitation theory and the graviton mass. **JETP Lett.**, v. 12, p. 312, 1970.

APPENDIX A – GENERAL RELATIVITY: GAUGE INVARIANTS

The transformations acting on the decomposition of the field $h_{\mu\nu}$ lead us to the following relations:

$$\widetilde{h}_{00} = 2\phi + 2\partial_0\xi_0 = 2(\phi + \partial_0\xi_0) \equiv 2\widetilde{\phi} \tag{A.1}$$

$$\widetilde{h}_{0i} = B_i + \partial_i S + \partial_0\xi_i + \partial_i\xi_0 \tag{A.2}$$

$$= B_i + \partial_i S + \partial_0\xi_i^D + \partial_0\partial_i\xi^R + \partial_i\xi_0$$

$$= (B_i + \partial_0\xi_i^D) + \partial_i(S + \partial_0\xi^R + \xi_0)$$

$$\equiv \widetilde{B}_i + \partial_i\widetilde{S}.$$

$$\widetilde{h}_{ij} = 2\delta_{ij}\psi + 2\partial_i\partial_j E + \partial_i F_j + \partial_j F_i + h_{ij}^{TT} + \partial_i\xi_j + \partial_i\xi_j \tag{A.3}$$

$$= 2\delta_{ij}\psi + 2\partial_i\partial_j E + \partial_i F_j + \partial_j F_i + h_{ij}^{TT} + \partial_i(\xi_j^D + \partial_j\xi^R) + \partial_j(\xi_i^D + \partial_i\xi^R)$$

$$= 2\delta_{ij}\psi + 2\partial_i\partial_j(E + \xi^R) + \partial_i(F_j + \xi_j^D) + \partial_j(F_i + \xi_i^D) + h_{ij}^{TT}$$

$$\equiv 2\delta_{ij}\widetilde{\psi} + 2\partial_i\partial_j\widetilde{E} + \partial_i\widetilde{F_j} + \partial_j\widetilde{F}_i + \widetilde{h}_{ij}^{TT}.$$

Combining the gauge invariants ϕ, S and E, we have:

$$\tilde{\phi} - \frac{1}{2}\partial_0\tilde{S} = \phi + \frac{1}{2}\partial_0\xi_0 - \frac{1}{2}\partial_0 S - \frac{1}{2}\partial_0\partial_0\xi^R \tag{A.4}$$

$$\partial_0\partial_0\tilde{E} - \frac{1}{2}\partial_0\tilde{S} = \partial_0\partial_0 E + \frac{1}{2}\partial_0\partial_0\xi^R - \frac{1}{2}\partial_0 S - \frac{1}{2}\partial_0\xi_0 \tag{A.5}$$

and then, adding the two equations above, we have

$$D = \phi - \partial_0 S + \partial_0^2 E. \tag{A.6}$$

APPENDIX B – MASSIVE GRAVITY: FINDING THE EQUATIONS OF MOTION

Starting from the action given by

$$S = \int d^4x \mathcal{L}_{m=0} - \frac{1}{2}m^2(h_{\mu\nu}h^{\mu\nu} - h^2) - \frac{1}{2}F_{\mu\nu}F^{\mu\nu} - 2m(h_{\mu\nu}\partial^\mu A^\nu - h\partial_\mu A^\mu) \tag{B.1}$$

$$-2(h_{\mu\nu}\partial^\mu\partial^\nu\Phi - h\Box\Phi) + kh_{\mu\nu}T^{\mu\nu} - \frac{2}{m}kA_\mu\partial_\nu T^{\mu\nu} + \frac{2}{m^2}k\phi\partial\partial T.$$

we will make:

- PART I :

$$\partial_\mu\left(\frac{\partial\mathcal{L}}{\partial(\partial_\mu h_{\varepsilon\rho})}\right) - \frac{\partial\mathcal{L}}{\partial h_{\varepsilon\rho}} = 0 \tag{B.2}$$

- PART II :

$$\partial_\mu\left(\frac{\partial\mathcal{L}}{\partial(\partial_\mu A_\nu)}\right) - \frac{\partial\mathcal{L}}{\partial A_\nu} = 0 \tag{B.3}$$

- PART III :

$$\partial_\mu\left(\frac{\partial\mathcal{L}}{\partial(\partial_\mu\Phi)}\right) - \frac{\partial\mathcal{L}}{\partial\Phi} = 0. \tag{B.4}$$

Knowing that

$$\partial\partial T = \partial_\mu\partial_\nu T^{\mu\nu} \tag{B.5}$$

$$F_{\mu\nu} \equiv \partial_\mu A_\nu - \partial_\nu A_\mu \tag{B.6}$$

and assuming the following notation:

$$\partial_\alpha h_{\mu\nu} = h_{\mu\nu,\alpha} \tag{B.7}$$

$$\eta_{\sigma\lambda}h^{\sigma\lambda} = h \tag{B.8}$$

$$\partial_\mu\partial^\mu \equiv \Box \tag{B.9}$$

B.1 PART I

Initially we have find the equations of motion that comes from (B.1) varing the action with respect to the field $h_{\mu\nu}$. We will do this with each term separately and then joining the results, since the equations are extensive.

- First term:

The first term is:

$$\mathcal{L}_1 = -\frac{1}{2}m^2(h_{\mu\nu}h^{\mu\nu} - h^2) = -\frac{1}{2}(h_{\mu\nu}\eta^{\mu\alpha}\eta^{\beta\nu}h_{\alpha\beta} - (\eta^{\gamma\sigma}h_{\gamma\sigma})^2). \tag{B.10}$$

Using (B.2):

$$-\frac{\partial\mathcal{L}_1}{\partial h_{\varepsilon\rho}} = \frac{1}{2}m^2\left[\eta^{\mu\alpha}\eta^{\beta\nu}\frac{\partial h_{\mu\nu}h_{\alpha\beta}}{\partial h_{\varepsilon\rho}} - \frac{\partial(\eta^{\gamma\sigma}h_{\gamma\sigma})^2}{\partial h_{\varepsilon\rho}}\right] = \tag{B.11}$$

$$= \frac{1}{2}m^2\left[\eta^{\mu\alpha}\eta^{\beta\nu}\left(\frac{\partial h_{\mu\nu}}{\partial h_{\varepsilon\rho}}h_{\alpha\beta} + \frac{\partial h_{\alpha\beta}}{\partial h_{\varepsilon\rho}}h_{\mu\nu}\right) - 2(\eta^{\gamma\sigma}h_{\gamma\sigma})\frac{h_{\gamma\sigma}}{\partial h_{\varepsilon\rho}}\eta^{\gamma\sigma}\right] =$$

$$= \frac{1}{2}m^2\left(\eta^{\mu\alpha}\eta^{\beta\nu}(\delta^{\varepsilon}_{\mu}\delta^{\rho}_{\nu}h_{\alpha\beta} + \delta^{\varepsilon}_{\alpha}\delta^{\rho}_{\beta}h_{\mu\nu}) - 2h\ \eta^{\gamma\sigma}\delta^{\varepsilon}_{\gamma}\delta^{\rho}_{\sigma}\right) =$$

$$= \frac{1}{2}m^2\left(\eta^{\varepsilon\alpha}\eta^{\beta\rho}h_{\alpha\beta} + \eta^{\mu\varepsilon}\eta^{\rho\nu}h_{\mu\nu} - h\ \eta^{\varepsilon\rho}\right) =$$

$$= \frac{1}{2}m^2\left(h^{\varepsilon\rho} + h^{\varepsilon\rho} - 2\eta^{\varepsilon\rho}h\right) =$$

$$= m^2\left(h^{\varepsilon\rho} - \eta^{\varepsilon\rho}h\right)$$

- Second term:

The second term does not depend on $h_{\mu\nu}$.

- Third term:

The third term is:

$$\mathcal{L}_3 = -2m(h_{\mu\nu}\partial^{\mu}A^{\nu} - h\partial_{\mu}A^{\mu}) = -2m(h_{\mu\nu}\partial^{\mu}A^{\nu} - \eta^{\beta\gamma}h_{\beta\gamma}\partial_{\mu}A^{\mu}). \tag{B.12}$$

Using (B.2), we have:

$$-\frac{\partial\mathcal{L}_3}{\partial h_{\varepsilon\rho}} = 2m\left[\partial^{\mu}A^{\nu}\frac{\partial h_{\mu\nu}}{\partial h_{\varepsilon\rho}} - \partial_{\mu}A^{\mu}\eta^{\beta\gamma}\frac{\partial h_{\beta\gamma}}{\partial h_{\varepsilon\rho}}\right] = \tag{B.13}$$

$$= 2m\left[\partial^{\mu}A^{\nu}\delta^{\varepsilon}_{\mu}\delta^{\rho}_{\nu} - \partial_{\mu}A^{\mu}\eta^{\beta\gamma}\delta^{\varepsilon}_{\beta}\delta^{\rho}_{\gamma}\right] =$$

$$= 2m\left(\partial^{\varepsilon}A^{\rho} - \partial_{\mu}A^{\mu}\eta^{\varepsilon\rho}\right).$$

Symmetrizing the previous expression, we get:

$$= 2m\left[\frac{1}{2}\left(\partial^{\varepsilon}A^{\rho} + \partial^{\rho}A^{\varepsilon}\right) - \partial_{\mu}A^{\mu}\eta^{\varepsilon\rho}\right] \tag{B.14}$$

- Fourth term:

The fourth term is:

$$\mathcal{L}_4 = -2(h_{\mu\nu}\partial^\mu\partial^\nu\Phi - h\partial^2\Phi) = -2\left(h_{\mu\nu}\partial^\mu\partial^\nu\Phi - \eta^{\alpha\beta}h_{\alpha\beta}\partial^2\Phi\right). \tag{B.15}$$

Using (B.2), we have:

$$-\frac{\partial\mathcal{L}_4}{\partial h_{\varepsilon\rho}} = 2\left(\partial^\mu\partial^\nu\Phi\frac{\partial h_{\mu\nu}}{\partial h_{\varepsilon\rho}} - \partial^2\Phi\eta^{\alpha\beta}\frac{\partial h_{\alpha\beta}}{\partial h_{\varepsilon\rho}}\right) = \tag{B.16}$$

$$= 2\left(\partial^\mu\partial^\nu\Phi\ \delta^\varepsilon_\mu\delta^\rho_\nu - \partial^2\Phi\eta^{\alpha\beta}\ \delta^\varepsilon_\alpha\delta^\rho_\beta\right) =$$

$$= 2\left(\partial^\varepsilon\partial^\rho\Phi - \partial^2\Phi\eta^{\varepsilon\rho}\right).$$

- Fifth term:

The fifth term is:

$$\mathcal{L}_5 = kh_{\mu\nu}T^{\mu\nu}. \tag{B.17}$$

Then using (B.2), we have:

$$-\frac{\partial\mathcal{L}_5}{\partial h_{\varepsilon\rho}} = -kT^{\mu\nu}\delta^\varepsilon_\mu\delta^\rho_\nu = -kT^{\varepsilon\rho}. \tag{B.18}$$

- The sixth and seventh terms do not depend on $h_{\mu\nu}$.

Combining the results and considering the energy-momentum tensor equal to zero, we get

$$\text{General Relativity} + m^2\left(h^{\varepsilon\rho} - \eta^{\varepsilon\rho}h\right) + 2m\left[\frac{1}{2}\left(\partial^\varepsilon A^\rho + \partial^\rho A^\varepsilon\right) - \partial_\mu A^\mu\eta^{\varepsilon\rho}\right] + \tag{B.19}$$

$$+2\left(\partial^\varepsilon\partial^\rho\Phi - \eta^{\varepsilon\rho}\Box\Phi\right) = 0.$$

Using Mathematica software, the equation found for the massive part was:

$$m^2\left(-h_{\varepsilon\rho} + \eta_{\varepsilon\rho}h\right) + 2m\left[-\frac{1}{2}\left(\partial_\varepsilon A_\rho + \partial_\rho A_\varepsilon\right) + \partial_\mu A^\mu\eta_{\varepsilon\rho}\right] - \tag{B.20}$$

$$-2\left(\partial_\varepsilon\partial_\rho\Phi + \eta_{\varepsilon\rho}\Box\Phi\right) = 0.$$

B.2 PART II

Now, following the same procedure as before, we want to find the equations of motion for the field A. With that we have:

The first term does not depend on A.

- Second term:

The second term is

$$\mathcal{L}_{2A} = -\frac{1}{2}F_{\mu\nu}F^{\mu\nu} = -\frac{1}{2}F_{\mu\nu}\eta^{\mu\alpha}\eta^{\beta\nu}F_{\alpha\beta} = \tag{B.21}$$

$$= -\frac{1}{2}\Big\{ \left(\partial_\mu A_\nu - \partial_\nu A_\mu\right)\left(\eta^{\mu\alpha}\eta^{\beta\nu}\left(\partial_\alpha A_\beta - \partial_\beta A_\alpha\right)\right) \Big\}$$

$$= -\frac{1}{2}\Big\{ \left(\partial_\mu A_\nu - \partial_\nu A_\mu\right)\left(\eta^{\mu\alpha}\eta^{\beta\nu}\partial_\alpha A_\beta - \eta^{\mu\alpha}\eta^{\beta\nu}\partial_\beta A_\alpha\right) \Big\}$$

$$= -\frac{1}{2}\eta^{\mu\alpha}\eta^{\beta\nu}\Big\{\partial_\alpha A_\beta\partial_\mu A_\nu - \partial_\beta A_\alpha\partial_\mu A_\nu - \partial_\nu A_\mu\partial_\alpha A_\beta + \partial_\nu A_\mu\partial_\beta A_\alpha\Big\}$$

Using (B.3), we have:

$$\partial_\varepsilon\left(\frac{\partial\mathcal{L}_{2A}}{\partial(\partial_\varepsilon A_\rho)}\right) = -\frac{1}{2}\eta^{\mu\alpha}\eta^{\beta\nu}\ \partial_\varepsilon\Big\{\partial_\alpha A_\beta\frac{\partial A_{\nu,\mu}}{\partial A_{\rho,\varepsilon}} + \partial_\mu A_\nu\frac{\partial A_{\beta,\alpha}}{\partial A_{\rho,\varepsilon}} - \partial_\beta A_\alpha\frac{\partial A_{\nu,\mu}}{\partial A_{\rho,\varepsilon}} - \tag{B.22}$$

$$-\partial_\mu A_\nu\frac{\partial A_{\alpha,\beta}}{\partial A_{\rho,\varepsilon}} - \partial_\nu A_\mu\frac{\partial A_{\beta,\alpha}}{\partial A_{\rho,\varepsilon}} - \partial_\alpha A_\beta\frac{\partial A_{\mu,\nu}}{\partial A_{\rho,\varepsilon}} + \partial_\nu A_\mu\frac{\partial A_{\alpha,\beta}}{\partial A_{\rho,\varepsilon}} + \partial_\beta A_\alpha\frac{\partial A_{\mu,\nu}}{\partial A_{\rho,\varepsilon}}\Big\}$$

$$= -\frac{1}{2}\eta^{\mu\alpha}\eta^{\beta\nu}\ \partial_\varepsilon\Big\{\partial_\alpha A_\beta\ \delta^\rho_\nu\delta^\varepsilon_\mu + \partial_\mu A_\nu\ \delta^\rho_\beta\delta^\varepsilon_\alpha - \partial_\beta A_\alpha\ \delta^\rho_\nu\delta^\varepsilon_\mu - \partial_\mu A_\nu\ \delta^\rho_\alpha\delta^\varepsilon_\beta - \partial_\nu A_\mu\ \delta^\rho_\beta\delta^\varepsilon_\alpha -$$

$$-\partial_\alpha A_\beta\ \delta^\rho_\mu\delta^\varepsilon_\nu + \partial_\nu A_\mu\ \delta^\rho_\alpha\delta^\varepsilon_\beta + \partial_\beta A_\alpha\ \delta^\rho_\mu\delta^\varepsilon_\nu\Big\}$$

$$= -\frac{1}{2}\partial_\varepsilon\Big\{\partial_\alpha A_\beta\eta^{\varepsilon\alpha}\eta^{\beta\rho} + \partial_\mu A_\nu\eta^{\mu\varepsilon}\eta^{\rho\nu} - \partial_\beta A_\alpha\eta^{\varepsilon\alpha}\eta^{\beta\rho} - \partial_\mu A_\nu\eta^{\mu\rho}\eta^{\varepsilon\nu} -$$

$$-\partial_\nu A_\mu\eta^{\mu\varepsilon}\eta^{\rho\nu} - \partial_\alpha A_\beta\eta^{\rho\alpha}\eta^{\beta\varepsilon} + \partial_\nu A_\mu\eta^{\mu\rho}\eta^{\varepsilon\nu} + \partial_\beta A_\alpha\eta^{\rho\alpha}\eta^{\beta\varepsilon}\Big\}$$

$$= -\frac{1}{2}\left(4\Box A^\rho - 4\partial_\varepsilon\partial^\rho A^\varepsilon\right)$$

$$= -2\Box A^\rho + 2\ \partial_\varepsilon\partial^\rho A^\varepsilon. \tag{B.23}$$

- Third term:

The third term is

$$\mathcal{L}_{3A} = -2(h_{\mu\nu}\partial^\mu A^\nu - h\partial_\mu A^\mu) = -2m\left(h_{\mu\nu}\eta^{\alpha\mu}\partial_\alpha\eta^{\gamma\nu}A_\gamma - h\partial_\mu\eta^{\sigma\mu}A_\sigma\right) \tag{B.24}$$

Using (B.3), we have:

$$\partial_\varepsilon\left(\frac{\partial\mathcal{L}_{3A}}{\partial(A_{\rho,\varepsilon})}\right)=\partial_\varepsilon\left[-2m\left(h_{\mu\nu}\eta^{\alpha\mu}\eta^{\gamma\nu}\frac{\partial(A_{\gamma,\alpha})}{\partial A_{\rho,\varepsilon}}-h\eta^{\sigma\mu}\frac{\partial(A_{\sigma,\mu})}{\partial A_{\rho,\varepsilon}}\right)\right] \tag{B.25}$$

$$=\partial_\varepsilon\left[-2m\left(h_{\mu\nu}\eta^{\alpha\mu}\eta^{\gamma\nu}\delta^\rho_\gamma\delta^\varepsilon_\alpha-h\eta^{\sigma\mu}\delta^\rho_\sigma\delta^\varepsilon_\mu\right)\right]$$

$$=\partial_\varepsilon\left[-2m\left(h_{\mu\nu}\eta^{\varepsilon\mu}\eta^{\rho\nu}-h\eta^{\rho\varepsilon}\right)\right]$$

$$=-2m\left(\partial_\varepsilon h^{\varepsilon\rho}-\partial^\rho h\ \right).$$

- The fourth and fifth terms do not depend on A.

- Sixth term:

The sixth term is

$$\mathcal{L}_{6A}=-\frac{2}{m}kA_\mu\partial_\nu T^{\mu\nu} \tag{B.26}$$

Using (B.3), we have:

$$-\frac{\partial\mathcal{L}_{6A}}{\partial A_\rho}=-\left(-\frac{2}{m}k\partial_\nu T^{\mu\nu}\frac{\partial A_\mu}{\partial A_\rho}\right) \tag{B.27}$$

$$=\frac{2}{m}k\partial_\nu T^{\mu\nu}\delta^\rho_\mu \tag{B.28}$$

$$=\frac{2}{m}k\partial_\nu T^{\rho\nu}. \tag{B.29}$$

- The seventh term does not depend on A.

Once again, combining the results and considering the energy-momentum tensor equal to zero, we have

$$\Box A^\rho-\ \partial_\varepsilon\partial^\rho A^\varepsilon+m\left(\partial_\varepsilon h^{\varepsilon\rho}-\partial^\rho h\ \right)=0. \tag{B.30}$$

B.3 PART III

Now we want to find the equations of motion for the field Φ following the same steps as before. With that we have:

- The terms 1,2,3,5 and 6 do not depend on Φ.

- Fourth term:

The fourth term is

$$\mathcal{L}_{4\Phi} = -2(h_{\mu\nu}\partial^{\mu}\partial^{\nu}\Phi - h\partial^{2}\Phi) = -2(h_{\mu\nu}\eta^{\alpha\mu}\partial_{\alpha}\eta^{\beta\nu}\partial_{\beta}\Phi - h\partial^{2}\Phi) \tag{B.31}$$

Using (B.4), we have:

$$\begin{aligned}\partial_{\varepsilon}\left(\frac{\partial\mathcal{L}_{4\Phi}}{\partial(\partial_{\varepsilon}\Phi)}\right) = \partial_{\varepsilon}\Bigg\{ -2\Bigg(h_{\mu\nu}\eta^{\alpha\mu}\eta^{\beta\nu}\left(\frac{\partial\Phi_{,\alpha}}{\partial\Phi_{,\varepsilon}}\partial_{\beta} + \frac{\partial\Phi_{,\beta}}{\partial\Phi_{,\varepsilon}}\partial_{\alpha}\right) \\ -h\eta^{\rho\sigma}\left(\frac{\partial\Phi_{,\sigma}}{\partial\Phi_{,\varepsilon}}\partial_{\rho} + \frac{\partial\Phi_{,\rho}}{\partial\Phi_{,\varepsilon}}\partial_{\sigma}\right)\Bigg)\Bigg\}\end{aligned} \tag{B.32}$$

$$= \partial_{\varepsilon}\Big\{ -2\left[h_{\mu\nu}\eta^{\alpha\mu}\eta^{\beta\nu}\left(\delta^{\varepsilon}_{\alpha}\partial_{\beta} + \delta^{\varepsilon}_{\beta}\partial_{\alpha}\right) - h\eta^{\rho\sigma}\left(\delta^{\varepsilon}_{\rho}\partial_{\sigma} + \delta^{\varepsilon}_{\sigma}\partial_{\rho}\right)\right]\Big\}$$

$$= \partial_{\varepsilon}\left[-2\left(h_{\mu\nu}\eta^{\varepsilon\mu}\partial^{\nu} + h_{\mu\nu}\eta^{\varepsilon\nu}\partial^{\mu} - h\eta^{\varepsilon\sigma}\partial_{\sigma} - h\eta^{\rho\sigma}\partial_{\rho}\right)\right]$$

$$= -2\left(h_{\mu\nu}\partial_{\varepsilon}\partial^{\nu}\eta^{\varepsilon\mu} + h_{\mu\nu}\partial_{\varepsilon}\partial^{\mu}\eta^{\varepsilon\nu} - 2\partial_{\varepsilon}\partial^{\varepsilon}h\right)$$

$$= -4\left(h_{\mu\nu}\partial^{\mu}\partial^{\nu} - \Box h\right)$$

$$= \Box h - \partial^{\mu}\partial^{\nu}h_{\mu\nu}.$$

- Seventh term:

The seventh term is:

$$\mathcal{L}_{7\Phi} = \frac{2}{m}k\Phi\partial\partial T = \frac{2}{m}k\Phi\partial_{\mu}\partial_{\nu}T^{\mu\nu} \tag{B.33}$$

Using (B.4), we have:

$$\frac{\partial\mathcal{L}_{7\Phi}}{\partial\Phi} = -\frac{2}{m}k\partial_{\mu}\partial_{\nu}T^{\mu\nu}\frac{\partial\Phi}{\partial\Phi} = -\frac{2}{m}k\partial\partial T \tag{B.34}$$

Combining the two results and considering the energy-momentum tensor equal to zero, we get

$$\Box h - \partial^{\mu}\partial^{\nu}h_{\mu\nu} = 0. \tag{B.35}$$

APPENDIX C – MASSIVE GRAVITY: FIELD DECOMPOSITIONS AND GAUGE INVARIANTS

C.1 FIELD DECOMPOSITIONS

Decomposition of the field A

$$\tilde{A}_i = J_i + \partial_i M - \xi_i \tag{C.1}$$

$$= J_i + \partial_i M - \xi_i^D - \partial_i \xi^R$$

$$= (J_i - \xi_i^D) + \partial_i (M - \xi^R)$$

$$= \tilde{J}_i + \partial_i \tilde{M}.$$

and

$$\tilde{\tilde{A}}_i = J_i + \partial_i M + \partial_i \Lambda \tag{C.2}$$

$$= J_i + \partial_i (M + \Lambda)$$

$$= \tilde{\tilde{J}} + \partial_i \tilde{\tilde{M}}.$$

C.2 GAUGE INVARIANTS

- Combination between gauge invariants:

Combining $\tilde{\tilde{M}}$ and $\tilde{\tilde{\omega}}$, we have

$$\tilde{f}_1 = \frac{1}{2}\partial_0 \tilde{\tilde{M}} - \tilde{\tilde{\omega}} = \frac{1}{2}\partial_0 M + \frac{1}{2}\cancel{\partial_0 \Lambda} - \omega - \frac{1}{2}\cancel{\partial_0 \Lambda} \tag{C.3}$$

$$= \frac{1}{2}\partial_0 M - \omega = f_1.$$

Combining $\tilde{\phi}$, $\tilde{S}$ e $\tilde{M}$, we have

$$\tilde{f}_2 = \tilde{\phi} - \partial_0 \tilde{S} - \partial_0^2 \tilde{M} \tag{C.4}$$

$$= \phi + \cancel{\partial_0 \xi_0} - \partial_0 S - \cancel{\partial_0^2 \xi^R} - \cancel{\partial_0 \xi_0} - \partial_0^2 M - \cancel{\partial_0^2 \xi^R}$$

$$= \phi - \partial_0 S - \partial_0^2 M = f_2.$$

It is also possible to combine $\tilde{\omega}$, $\tilde{S}$ and $\tilde{E}$:

$$\tilde{f}_3 = \tilde{\omega} + \frac{1}{2}\tilde{S} - \frac{1}{2}\partial_0 \tilde{E} \tag{C.5}$$

$$= \omega - \frac{1}{\cancel{2}}\cancel{\xi_0} + \frac{1}{2}S + \frac{1}{\cancel{2}}\cancel{\partial_0 \xi^R} + \frac{1}{\cancel{2}}\cancel{\xi_0} - \frac{1}{2}\partial_0 E - \frac{1}{\cancel{2}}\cancel{\partial_0 \xi^R}$$

$$= \omega + \frac{1}{2}S - \frac{1}{2}\partial_0 E = f_3$$

or even $\tilde{\omega}$, $\tilde{S}$ and $\tilde{M}$, so we have

$$\tilde{f}_4 = 2\tilde{\omega} + \tilde{S} + \partial_0 \tilde{M} \tag{C.6}$$

$$= 2\omega - \cancel{\xi_0} + S + \cancel{\partial_0 \xi^R} + \cancel{\xi_0} + \partial_0 M - \cancel{\partial_0 \xi^R}$$

$$= 2\omega + \partial_0 M + S = f_4.$$

Finally, we can combine $\tilde{F}$, $\tilde{J}$ and $\tilde{B}$:

$$\tilde{f}_5 = 2\partial_0 \tilde{J}_i + \partial_0 \tilde{F}_i + \tilde{B}_i \tag{C.7}$$

$$= 2\partial_0 J_i - 2\cancel{\partial_0 \xi_i^{\not D}} + \partial_0 F_i + \cancel{\partial_0 \xi_i^{\not D}} + B_i + \cancel{\partial_0 \xi_i^{\not D}}$$

$$= 2\partial_0 J_i + \partial_0 F_i + B_i = f_5.$$

- Writing the third equation of motion as a function of gauge invariants:

$$\Box h - \partial^\epsilon \partial^\rho h_{\epsilon\rho} = 0 \tag{C.8}$$

Performing the decomposition of the field $h_{\mu\nu}$, we are left with

$$\Box h - \partial^0 \partial^0 h_{00} - 2\partial^0 \partial^i h_{0i} - \partial^i \partial^j h_{ij} = 0 \tag{C.9}$$

$$\Box \left(-2\,\phi + 6\psi + 2\nabla^2 E\right) - 2\,\partial^0 \partial^0 \phi - \cancel{2\,\partial^0 \partial^i B_i}^{\,0} - 2\,\partial^0 \partial^i \partial_i S - \tag{C.10}$$

$$-2\,\partial^i \partial^j \delta_{ij} \Psi - 2\,\partial^i \partial^j \partial_i \partial_j E - \cancel{\partial^i \partial^j \partial_i F_j}^{\,0} - \cancel{\partial^i \partial^j \partial_j F_i}^{\,0} + \cancel{\partial^i \partial^j h_{ij}^{TT}}^{\,0} = 0.$$

and knowing that we can write

$$\Box(\nabla^2 E) = \partial_0\partial^0(\nabla^2 E) + \nabla^2(\nabla^2 E), \tag{C.11}$$

we have

$$-2\Box\phi + 6\Box\Psi + 2\ \partial_0\partial^0(\nabla^2 E) + \cancel{2\ \nabla^2(\nabla^2 E)} - 2\partial^0\ \nabla^2 S - \tag{C.12}$$

$$-2\ \partial^0\partial^0\phi - 2\partial^i\partial^i\Psi - \cancel{2\nabla^2(\nabla^2 E)} = 0.$$

$$\cancel{-2\partial_0\partial^0\phi} - 2\nabla^2\phi - 6\partial_0^2\Psi + 6\nabla^2\Psi - 2\ \partial_0^2(\nabla^2 E) - \tag{C.13}$$

$$+2\partial_0\ \nabla^2 S + \cancel{2\partial_0\partial^0\phi} - 2\nabla^2\Psi = 0.$$

$$\nabla^2\left(-2\phi + 6\Psi - 2\partial_0^2 E + 2\partial_0 S - 2\Psi\right) - 6\ \partial_0^2\Psi = 0. \tag{C.14}$$

Dividing everything by (-2), we get

$$\nabla^2\left(\phi - 2\Psi + \partial_0^2 E - \partial_0 S\right) + 3\ \partial_0^2\Psi = 0. \tag{C.15}$$

and finally we are left with

$$\nabla^2\left(D - 2\Psi\right) + 3\ \partial_0^2\Psi = 0. \tag{C.16}$$

C.3 COORDINATE CHANGE

In chapter 4 we have used the following coordinate change in our equations of motion

$$h_{\mu\nu} = h'_{\mu\nu} + \pi\eta_{\mu\nu}. \tag{C.17}$$

With that we had,

- For the equation (4.37):

$$\Box h^{\mu\nu} - \partial_\alpha\partial^\mu h^{\nu\alpha} - \partial_\alpha\partial^\nu h^{\mu\alpha} + \partial^\mu\partial^\nu h - \eta^{\mu\nu}\left(\Box h - \partial\alpha\partial_\beta h^{\alpha\beta}\right) + \tag{C.18}$$

$$+2\left(\partial^\mu\partial^\nu\Phi - \eta^{\mu\nu}\Box\Phi\right) = 0.$$

$$\Box\left(h'^{\mu\nu} + \pi\eta^{\mu\nu}\right) - \partial_\alpha\partial^\mu\left(h'^{\nu\alpha} + \pi\eta^{\nu\alpha}\right) - \partial_\alpha\partial^\nu\left(h'^{\mu\alpha} + \pi\eta^{\mu\alpha}\right) + \tag{C.19}$$

$$+\partial^\mu\partial^\nu\left(h'+4\pi\right)-\eta^{\mu\nu}\left[\Box\left(h'+4\pi\right)-\partial_\alpha\partial_\beta\left(h'^{\alpha\beta}+\pi\eta^{\alpha\beta}\right)\right]+2\left(\partial^\mu\partial^\nu\Phi-\eta^{\mu\nu}\Box\Phi\right).$$

$$\Box h'^{\mu\nu}-\partial_\alpha\partial^\mu h'^{\nu\alpha}-\partial_\alpha\partial^\nu h'^{\mu\alpha}+\partial^\mu\partial^\nu h'-\eta^{\mu\nu}\Box h'+\eta^{\mu\nu}\partial_\alpha\partial_\beta h'^{\alpha\beta}+\Box\pi\eta^{\mu\nu}- \tag{C.20}$$

$$-\partial_\alpha\partial^\mu\pi\eta^{\nu\alpha}-\partial_\alpha\partial^\nu\pi\eta^{\mu\alpha}+\partial_\mu\partial^\nu 4\pi-\eta^{\mu\nu}\Box 4\pi+\eta^{\mu\nu}\partial_\alpha\partial_\beta\pi\eta^{\alpha\beta}+2\left(\partial^\mu\partial^\nu\Phi-\eta^{\mu\nu}\Box\Phi\right)=0.$$

Taking

$$\Box h'^{\mu\nu}-\partial_\alpha\partial^\mu h'^{\nu\alpha}-\partial_\alpha\partial^\nu h'^{\mu\alpha}+\partial^\mu\partial^\nu h'-\eta^{\mu\nu}\Box h'+\eta^{\mu\nu}\partial_\alpha\partial_\beta h'^{\alpha\beta}=(GR)'^{\mu\nu}, \tag{C.21}$$

we have,

$$(GR)'^{\mu\nu}-2\eta^{\mu\nu}\Box\pi+2\partial^\mu\partial^\nu\pi+2\left(\partial^\mu\partial^\nu\Phi-\eta^{\mu\nu}\Box\Phi\right)=0 \tag{C.22}$$

Taking $\pi=-\Phi$, we have

$$(GR)'^{\mu\nu}+2\eta^{\mu\nu}\Box\Phi-2\partial^\mu\partial^\nu\Phi+2\partial^\mu\partial^\nu\Phi-2\eta^{\mu\nu}\Box\Phi=0 \tag{C.23}$$

$$(GR)'^{\mu\nu}=0. \tag{C.24}$$

- For the equation (4.39):

$$\Box h-\partial^\mu\partial^\nu h_{\mu\nu}=0 \tag{C.25}$$

$$\Box(h'+4\pi)-\partial^\mu\partial^\nu(h'_{\mu\nu}+\pi\eta_{\mu\nu})=0. \tag{C.26}$$

$$\Box h'-\partial^\mu\partial^\nu h'_{\mu\nu}+4\Box\pi-\partial^\mu\partial^\nu\eta_{\mu\nu}\pi=0 \tag{C.27}$$

With $\pi=-\Phi$, we have

$$\Box h'-\partial^\mu\partial^\nu h'_{\mu\nu}-4\Box\Phi+\Box\Phi=0 \tag{C.28}$$

If we now take the trace of (C.24), we have

$$\Box h'-\partial_\alpha\partial_\nu h'^{\nu\alpha}-\partial_\alpha\partial_\mu h'^{\mu\alpha}+\Box h'-4\Box h'+4\partial_\alpha\partial_\beta h'^{\alpha\beta}=0 \tag{C.29}$$

$$\Box h' - \partial_\alpha \partial_\beta h'^{\alpha\beta} = 0 \tag{C.30}$$

Substituting this result in (C.23) we get

$$\partial_\mu \partial_\nu h'_{\mu\nu} - \partial_\mu \partial_\nu h'_{\mu\nu} - 3\Box\Phi = 0. \tag{C.31}$$

then

$$\Box\Phi = 0. \tag{C.32}$$

APPENDIX D – MASSIVE GRAVITY: ANOTHER APPROACH FOR THE VDVZ DISCONTINUITY

Starting from the action with $m = 0$ given by

$$S = \int d^4x \Big\{ \mathcal{L}_{m=0} - \frac{1}{2} F_{\mu\nu} F_{\mu\nu} - 2\left(h_{\mu\nu}\partial^\mu\partial^\nu\Phi - h\Box\Phi\right) + \kappa h_{\mu\nu} T^{\mu\nu} \Big\} \tag{D.1}$$

and taking the following transformation

$$h_{\mu\nu} = h'_{\mu\nu} + \Phi\eta_{\mu\nu} \tag{D.2}$$

we will see that the transformed action will be:

$$S = \int d^4x \left\{ \mathcal{L}_{m=0}(h') - \frac{1}{2} F_{\mu\nu} F^{\mu\nu} - 3\partial_\mu\Phi\partial^\mu\Phi + \kappa h'_{\mu\nu} T^{\mu\nu} + \kappa\Phi T \right\} \tag{D.3}$$

where the non-massive Lagrangian, when transformed, becomes:

$$\mathcal{L}_{m=0} = -\frac{1}{2}\partial_\lambda(h'_{\mu\nu} + \Phi\eta_{\mu\nu})\partial^\lambda(h'^{\mu\nu} + \Phi\eta^{\mu\nu}) + \partial_\mu(h'_{\nu\lambda} + \Phi\eta_{\nu\lambda})\partial^\nu(h'^{\mu\lambda} + \Phi\eta^{\mu\lambda}) - \tag{D.4}$$

$$-\partial_\mu(h'^{\mu\nu} + \Phi\eta^{\mu\nu})\partial_\nu(h' + 4\Phi) + \frac{1}{2}\partial_\lambda(h' + 4\Phi)\partial^\lambda(h' + 4\Phi) =$$

$$= -\frac{1}{2}\Big\{ \left(\partial_\lambda h'_{\mu\nu} + \partial_\lambda\Phi\eta_{\mu\nu}\right)\left(\partial^\lambda h'^{\mu\nu} + \partial^\lambda\Phi\eta^{\mu\nu}\right) \Big\} + \Big\{ \left(\partial_\mu h'_{\nu\lambda} + \partial_\mu\Phi\eta_{\nu\lambda}\right)\left(\partial^\nu h'^{\mu\lambda} + \partial^\nu\Phi\eta^{\mu\lambda}\right) \Big\} - \tag{D.5}$$

$$-\Big\{ \left(\partial_\mu h'^{\mu\nu} + \partial_\mu\Phi\eta^{\mu\nu}\right)\left(\partial_\nu h' + \partial_\nu 4\Phi\right) \Big\} + \frac{1}{2}\Big\{ \left(\partial_\lambda h' + \partial_\lambda 4\Phi\right)\left(\partial^\lambda h' + \partial^\lambda 4\Phi\right) \Big\} =$$

$$-\frac{1}{2}\Big\{ \partial_\lambda h'_{\mu\nu}\partial^\lambda h'^{\mu\nu} + \partial_\lambda h'_{\mu\nu}\partial^\lambda\Phi\eta^{\mu\nu} + \partial_\lambda\Phi\eta_{\mu\nu}\partial^\lambda h'^{\mu\nu} + \partial_\lambda\Phi\eta_{\mu\nu}\partial^\lambda\Phi\eta^{\mu\nu} \Big\} + \tag{D.6}$$

$$+\partial_\mu h'_{\nu\lambda}\partial^\nu h'^{\mu\lambda} + \partial_\mu h'_{\nu\lambda}\partial^\nu\Phi\eta^{\mu\lambda} + \partial_\mu\Phi\eta_{\nu\lambda}\partial^\nu h'^{\mu\lambda} + \partial_\mu\Phi\eta_{\nu\lambda}\partial^\nu\Phi\eta^{\mu\lambda} -$$

$$-\Big\{ \partial_\mu h'^{\mu\nu}\partial_\nu h' + \partial_\mu h'^{\mu\nu}\partial_\nu 4\Phi + \partial_\mu\Phi\eta^{\mu\nu}\partial_\nu h' + \partial_\mu\Phi\eta^{\mu\nu}\partial_\nu 4\Phi \Big\} +$$

$$+\frac{1}{2}\Big\{ \partial_\lambda h'\partial^\lambda h' + \partial_\lambda h'\partial^\lambda 4\Phi + \partial_\lambda 4\Phi\partial^\lambda h' + \partial_\lambda 4\Phi\partial^\lambda 4\Phi \Big\} =$$

$$= \mathcal{L}_{m=0}(h') + 3\partial_\mu\Phi\partial^\mu\Phi + 2\partial_\mu\Phi\partial^\mu h' - 2\partial_\mu\Phi\partial_\nu h'^{\mu\nu}. \tag{D.7}$$

Combining (D.1) with (D.7), we get the complete transformed action from which we will extract the equations of motion.

$$S = \int d^4x \Big\{ -\frac{1}{2}\partial_\lambda h'_{\mu\nu}\partial^\lambda h'^{\mu\nu} + \partial_\mu h'_{\nu\lambda}\partial^\nu h'^{\mu\lambda} - \partial_\mu h'^{\mu\nu}\partial_\nu h' + \frac{1}{2}\partial_\lambda h'\partial^\lambda h' - \tag{D.8}$$

$$-\frac{1}{2}F_{\mu\nu}F^{\mu\nu} - 3\partial_\mu\Phi\partial^\mu\Phi + \kappa h'_{\mu\nu}T^{\mu\nu} + \kappa\Phi T\Big\}.$$